INCOHERENT TARGET DECOMPOSITION OF POLSAR DATA FOR LAND APPLICATIONS

Ph.D. THESIS

by

HIMANSHU MAURYA

DEPARTMENT OF ELECTRONICS AND COMMUNICATION ENGINEERING
INDIAN INSTITUTE OF TECHNOLOGY ROORKEE
ROORKEE - 247 667 (INDIA)

FEBRUARY, 2019

INCOHERENT TARGET DECOMPOSITION OF POLSAR DATA FOR LAND APPLICATIONS

A THESIS

Submitted in partial fulfilment of the
requirements for the award of the degree

of

DOCTOR OF PHILOSOPHY

in

ELECTRONICS AND COMMUNICATION ENGINEERING

by

HIMANSHU MAURYA

DEPARTMENT OF ELECTRONICS AND COMMUNICATION ENGINEERING
INDIAN INSTITUTE OF TECHNOLOGY ROORKEE
ROORKEE - 247 667 (INDIA)

FEBRUARY, 2019

INDIAN INSTITUTE OF TECHNOLOGY ROORKEE
ROORKEE

CANDIDATE'S DECLARATION

I hereby certify that the work which is being presented in the thesis entitled **"INCOHERENT TARGET DECOMPOSITION OF POLSAR DATA FOR LAND APPLICATIONS"** in partial fulfilment of the requirements for the award of the Degree of Doctor of Philosophy and submitted in the Department of **Electronics and Communication Engineering** of Indian Institute of Technology Roorkee, Roorkee is an authentic record of my own work carried out during a period from **January, 2014** to **February, 2019** under the supervision of **Dr. R. K. Panigrahi**, Associate Professor, Department of Electronics and Communication Engineering of Indian Institute of Technology Roorkee, Roorkee, India.

The matter presented in this thesis has not been submitted by me for the award of any other degree of this or any other Institute.

(HIMANSHU MAURYA)

This is to certify that the above statement made by the candidate is correct to the best of my knowledge.

Date: 28 February 2019.

(R. K. Panigrahi)
Supervisor

ABSTRACT

The rapid growth of population with limited natural resources demands a study of anthropogenic modification of Earth surface and its environmental impact. Earth surface classification, popularly known as land-cover classification, is the first step to achieve this goal. Land-cover alteration is strongly associated with atmosphere, ecosystem process and human behavior, thereby can be related to worldwide climate change. The manual collection of Earth surface parameters is a herculean task. Also, the dynamic changing environment of Earth demands frequent observations of its surface. The most adequate alternative which provides the feasible solution to the challenge of timely observations of Earth surface in all weather conditions is polarimetric synthetic aperture radar (PolSAR) system. Since the backscattered polarization information depends on the sensitivity of the transmitted polarization to the dielectric and geometrical characteristics of scatterers, it is easier to extract the geophysical and biophysical parameters of Earth's surface with the fully polarimetric data. The PolSAR observed values are transformed into the parameters associated with the physical significance of the scatterer by so-called target decomposition theorems. Target decomposition theorems exploit the PolSAR information to interpret the scattering mechanisms. Since different types of land-covers involve different types of scattering, correct interpretation of the underlying scattering mechanism is the foundation of land-cover classification. A straightforward way to accomplish this is through the decomposition of PolSAR data into linear sum of physical scattering mechanisms. This principle is popularly referred to as model-based decomposition.

Although model-based decomposition technique for PolSAR data has been investigated for the last two decades, efficient and robust methods are still very few in number. The reason behind this is the inherited flaws of model-based decomposition technique. The efficacy of a model-based decomposition technique is mainly based on the appropriate modeling of physical scattering mechanisms. However, the scatterings from terrain targets highly depend on their relative orientation with respect to the radar illumination. Thereby, different type of scatterers with different orientations may generate similar scattering and vice versa, which give rise to scattering mechanism ambiguity. If the physical scattering mechanisms are not properly modeled, scattering mechanism ambiguity may lead to misclassification of land-covers. Another consequence of scattering mechanism ambiguity is the overestimation of some of the scattering powers. This overestimation may result in negative scattering contributions for other scattering mechanisms. The occurrence of negative scattering powers indicates that the backscattered polarimetric information is not properly modeled. The third issue related to the model-based methods is the under-determined equation system. Due to fewer number equations than unknowns, the branching conditions have to be applied in model-based decomposi-

tion methods. Branching conditions are the assumptions or constraints taken to solve the under-determined equation system of model-based decomposition methods. Because of this, the performances of model-based decomposition methods depend on the efficiency of branching conditions. These limitations restrict the applications of model-based decomposition methods. In order to resolve these issues, some feasible solutions are presented in this thesis.

The research work of this thesis can be divided into two main parts. In the first part, straightforward solutions to the challenges regarding scattering mechanism ambiguity and negative power problem of model-based decomposition methods are presented. The first part can be further broken into three sub-research works. In the first research work, a new urban scattering model is presented to deal with scattering mechanism ambiguity between vegetation and oriented urban areas. In the second work, unitary matrix rotations are applied to decouple the energy between co- and cross-polarization scattering mechanisms. This decoupling optimizes the PolSAR coherency matrix to be used for model-based decomposition methods. In the third research work, hybrid scattering models are utilized to address the negative power problem of model-based decomposition methods. The second part of the thesis investigates the significance of branching conditions in model-based decomposition methods. The first section of this second part presents computationally efficient alternate model-based decomposition schemes. These alternate decomposition schemes demonstrate a methodology to linearly solve the under-determined equation system of model-based decomposition methods without incorporation of branching conditions. In the second section, an efficient branching condition is presented to enhance the decomposition results of current model-based decomposition methods. In summary, this thesis contributes towards the development of new efficient model-based decomposition methods for land-cover classification. Simple approaches are also explored to optimize the PolSAR coherency matrix and to enhance the performance of existing model-based decomposition methods.

ACKNOWLEDGEMENTS

I owe my sincere thanks and gratitude to all those people who made this thesis possible and an unforgettable experience for me. Without their support, this achievement would have not been possible.

Words are inadequate in offering my deep sense of gratitude to my PhD supervisor **Dr. Rajib Kumar Panigrahi** for his continuous support and strong belief on me during every stage of this course. His guidance, motivation, and support helped me in all the time of research and writing of this Thesis. I always enjoyed his friendly accessibility and openness towards the discussions related to my research work. Apart from all these things, his positive attitude towards life will always inspire me to believe in destiny.

I am also indebted to **Prof. Amit Kumar Mishra** for his optimistic view towards every problem. His constant encouragement, open-mindedness, and vision teaches me to focus on many research areas parallelly. I am very much thankful to **Prof. M. V. Kartikeyan** for treating me like his own PhD student.

I would like to earnestly thank the rest of my doctoral committee: **Prof. D. Singh** and **Prof. R. D. Garg**, for their thoughtful suggestions and comments which widen my research perspectives.

I also express my heartfelt thanks to **Dr. A. Patnaik** and **Prof. D. Ghosh**, for their lectures during my course work. I am thankful to all the professors in the department of Electronics and Communication Engineering for their support and encouragement. I humbly extend my word of gratitude to our staffs and administration of the department for providing me valuable support.

I would like to express adequately my feeling of gratitude to **Ms. Ankita Deo** for having my back. Time that I spent with her is memorable and I will always cherish those moments. I would like to specially mention and thanks my friends **Mr. Gourav Modanwal**, **Mr. Manish Varyani**, **Mr. Gaurav Soni** and **Mr. Ajay Kumar Singh** for all the cherish moments and emotional support.

I have great pleasure in expressing my heartfelt thanks to my lab seniors and close friends **Dr. Jagannath Malik**, **Dr. Gaurav Singh Baghel** and **Dr. Sukwinder Singh**. Because of their constant support and encouragement, I never felt that I was the first student of my supervisor. I owe my thanks to **Mr. Yuvaraj** for supporting me during hard times of my life. I would like to thank my departmental seniors and friends **Dr. Ranjay Hazra**, **Dr. Satish Maheshwaram**, **Dr. Santosh Kumar Reddy**, **Dr. Prateek Dolas**, **Dr. Arvind Sharma**, **Dr. Dinesh Sharma**, **Mr. Om Prakash**, **Mr. Rakesh Sharma**, **Mr. Kumar Goodwill**, **Mr. Kamlesh Verma** and **Dr. Zahir Ahmed Ansari** for making my PhD duration special.

I would also like to thanks all other friends and fellow students particularly my Millimeter and THz wave labmates **Narendra**, **Sandeep**, **Upendra sir**, **Sambaiah sir**, **Amit**, **Surbhi Adya**, **Debasish**, **Aditya**, **Ayush** and **Vinit** for spending a great time throughout my PhD duration and providing me great memories from simulations, discussions, and the sleepless nights we were working together before the deadlines. They have always encouraged and supported me throughout this thesis work. Furthermore, I would also like to thank all others who directly or indirectly helped me during my stay at IIT Roorkee.

I wish to express my heartfelt love and gratitude to my parents **Mr. S. R. Maurya** and **Mrs. Kanchan Lata Maurya** for their unconditional love, care, support and strong belief on me in all ups and downs during this course and my life. I convey my deep gratitude to my loving sisters **Shikha** and **Adya** for never letting me feel lonely in life.

Himanshu Maurya

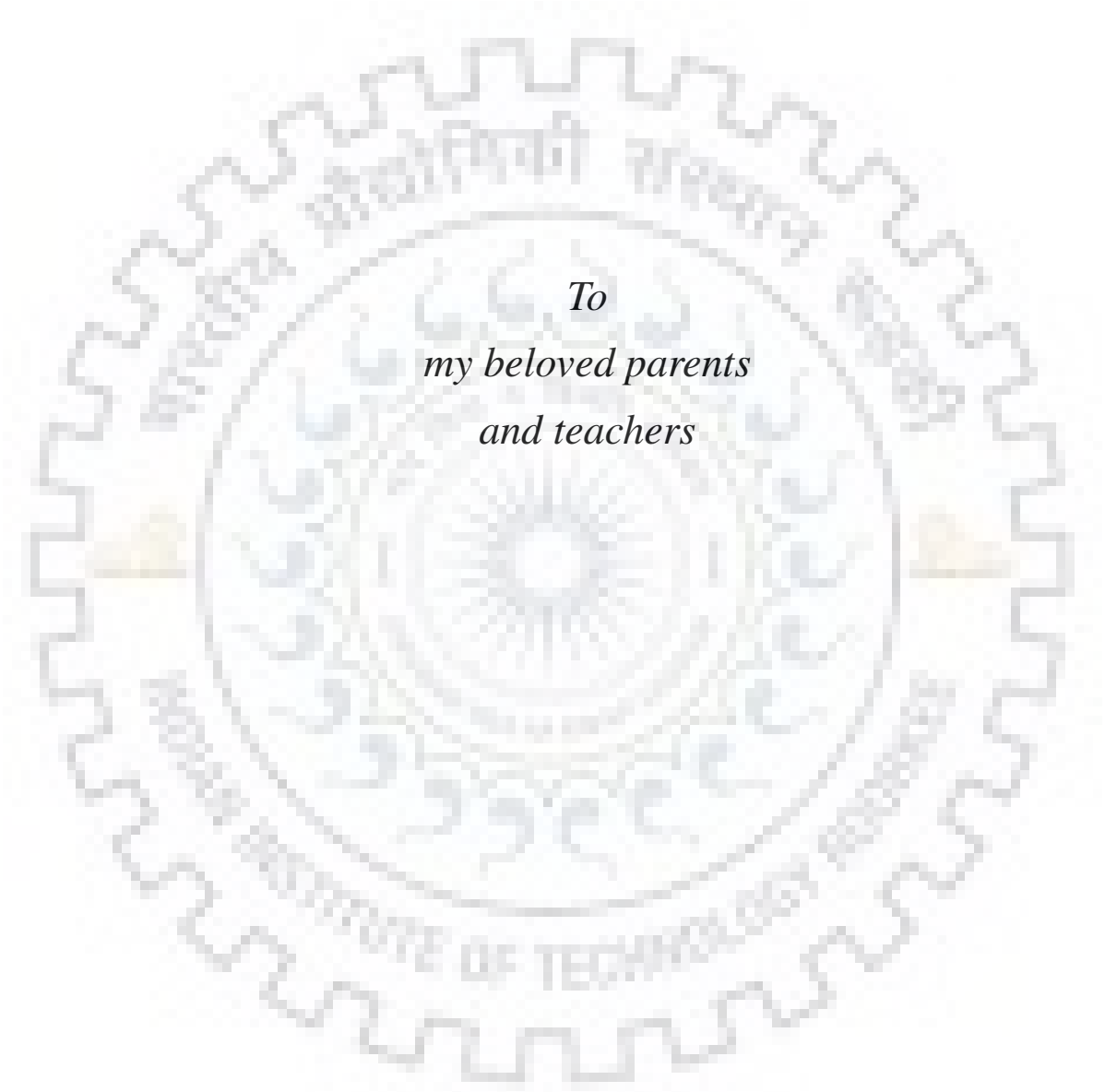

To

my beloved parents

and teachers

Contents

Abstract i
Acknowledgements iii
Table of Contents vii
List of Figures xi
List of Tables xiii

1 Introduction **1**
1.1 Polarimetric SAR Data Representation 2
1.1.1 Coherency and Covariance Matrices 2
1.2 Information Extraction from PolSAR Data 5
1.2.1 Coherent Decomposition Methods 5
1.2.2 Incoherent Decomposition Methods 6
1.3 PolSAR Environmental Applications 14
1.3.1 Forestry 15
1.3.2 Agriculture 15
1.3.3 Cryosphere 15
1.3.4 Ocean 16
1.3.5 Urban 16
1.3.6 Land-cover Classification 16
1.4 Research Objectives and Problem Statement 17
1.5 Organization of Thesis 19

2 Advancements in Model-Based Decomposition Category **21**
2.1 New Scattering Models 23
2.1.1 Surface Scattering Model 23
2.1.2 Dihedral Scattering Model 25
2.1.3 Volume Scattering Model 27
2.2 Unitary Rotations of Coherency Matrix 31
2.3 Elimination of Negative Power Problem 34
2.3.1 Scattering Similarity 36

3 Extended Four-Component Decomposition by Using Modified Cross-Scattering Matrix **39**
3.1 Introduction . . . 39
3.2 Generation of the Modified Cross-Scattering Matrix . . . 40
3.3 Decomposition Methodology . . . 41
3.4 Experimental Results and Discussion . . . 44
3.4.1 AIRSAR San Francisco Bay Data . . . 44
3.4.2 Radarsat-2 Mumbai Data . . . 48
3.5 Conclusion . . . 50

4 Optimization of Coherency Matrix Through Selective Unitary Rotations **53**
4.1 Introduction . . . 53
4.2 Special unitary SU(3) group . . . 54
4.2.1 T_{13} Element Removal in Dominant Surface Scattering Areas . . . 55
4.3 Freeman-Durdens' Decomposition (FDD) After Selective Unitary Rotations (SUR) . . . 57
4.4 Experimental Results and Discussion . . . 59
4.4.1 Radarsat-2 Quebec City Data . . . 60
4.4.2 AIRSAR Death Valley Data . . . 61
4.5 Conclusions . . . 63

5 Non-negative Scattering Power Decomposition **65**
5.1 Introduction . . . 65
5.1.1 Hybrid Three-Component Decomposition . . . 66
5.2 Hybrid Four-Component Decomposition (HFCD) . . . 67
5.3 Results and Discussion . . . 71
5.3.1 Radarsat-2 San Francisco Bay Data . . . 71
5.3.2 UAVSAR Hayward Data . . . 73
5.4 Conclusions . . . 76

6 Investigation of Branching Condition in Model-Based Decomposition Methods **77**
6.1 Introduction . . . 77
6.2 A Fast Alternative to Model-Based Decomposition Techniques . . . 77
6.2.1 First Unitary Transformation to Remove $\Re(T_{12})$ . . . 78
6.2.2 Second Unitary Transformation to Remove $\Im(T_{12})$ . . . 79
6.3 Alternate Decomposition Methodology . . . 80
6.4 Results and Discussion . . . 81

6.4.1 Computational Efficiency 82
6.5 Branching Conditions in Model-based Decomposition Methods 83
6.5.1 Branching Condition 1: $T_{11} - T_{22}$ 83
6.5.2 Branching Condition 2: $2T_{11} - TP + P_c$ 84
6.6 Branching Condition Based on Alpha ($\overline{\alpha}$) Angle 84
6.6.1 Deciding the boundary of $\overline{\alpha}$ angle 85
6.7 Results and Discussions 85
6.7.1 Radarsat-2 San Francisco Bay Data 88
6.7.2 UAVSAR Hayward Data 89
6.7.3 PiSAR Niigata Data 91
6.8 Conclusions 93

7 Conclusion and Future Scope **95**
7.1 Contribution of the Thesis 95
7.2 Future Scope 97

Bibliography **101**

List of Figures

1.1 $H/\overline{\alpha}$ plane. 9

2.1 Flowchart of the advancements in model-based decomposition category. . 21

3.1 Flowchart of E4D. 43
3.2 Color coded decomposed images of AIRSAR San Francisco data. (a) Pauli RGB. (b) Y4O. (c) Y4R. (d) E4D. 44
3.3 Orientation angle distribution. (a) Patch 1. (b) Patch 2. (c) Patch 3. 45
3.4 Classified images of urban Patch 1. (a) Y4O. (b) Y4R. (c) E4D. 46
3.5 Urban scattering powers along Transect 1. 46
3.6 Classified images of urban Patch 2. (a) Y4O. (b) Y4R. (c) E4D. 46
3.7 Urban scattering powers along Transect 2. 47
3.8 Classified images of urban Patch 3. (a) Y4O. (b) Y4R. (c) E4D. 47
3.9 Urban scattering powers along Transect 3. 48
3.10 Radarsat-2 Mumbai images. (a) Pauli RGB. (b) Optical Image. 49
3.11 Color coded decomposed images of Radarsat-2 Mumbai data. (a) Y4O (b) Y4R (c) E4D. 49

4.1 Flowchart of FDD after SUR. 59
4.2 Color coded decomposed images of Radarsat-2 Quebec City (blue: surface scattering (P_s), red: double-bounce scattering (P_d), green: volume scattering (P_v)). (a) FDD. (b) FDD after OAC. (c) FDD after SUR. 60
4.3 Color coded decomposed images of AIRSAR Death Valley (blue: surface scattering (P_s), red: double-bounce scattering (P_d), green: volume scattering (P_v)). (a) FDD. (b) FDD with OAC. (c) FDD after SUR. 62

5.1 Flowchart of HFCD Method. 70
5.2 C-band Radarsat-2 San Francisco image. (a) Pauli RGB image of Radarsat-2 San Francisco area with selected land-cover patches used for analysis. (b) Optical view of selected land-cover patches. 71

5.3 Color coded decomposed images of C-band Radarsat-2 San Francisco area. (a) Y4O. (b) Y4R. (c) HFCD. 72
5.4 L-band UAVSAR Hayward image. (a) Pauli RGB image of UAVSAR Hayward area with selected urban patches used for analysis. (b) Optical view of selected urban patches. 74
5.5 Color coded decomposed images of L-band UAVSAR Hayward area. (a) Y4O. (b) Y4R. (c) HFCD. 74
5.6 Volume scattering power (m_v) for UAVSAR Hayward image. (a) Y4O. (b) Y4R. (c) HFCD. 75

6.1 Color coded decomposed images of Radarsat-2 San Francisco area. (a) Alternate FDD. (b) Alternate Y4O. 81
6.2 Pauli RGB images. (a) Radarsat-2 San Francisco area. (b) UAVSAR Hayward area. (c) PiSAR Niigata area. 86
6.3 Urban pixels satisfying the different branching conditions for dominant dihedral scattering (Red color: Urban Pixels satisfying the dominant dihedral scattering condition, Blue color: Urban pixels violating the dominant dihedral scattering condition). 86
6.4 Color coded decomposed images of Radarsat-2 San Francisco area. (a)-(c) Y4O, Y4R, G4U, respectively with original branching conditions. (d)-(f) Y4O, Y4R, G4U, respectively with branching condition C_3. 88
6.5 Color coded decomposed images of UAVSAR Hayward area. (a)-(c) Y4O, Y4R, G4U, respectively with original branching conditions. (d)-(f) Y4O, Y4R, G4U, respectively with branching condition C_3. 90
6.6 Color coded decomposed images of PiSAR Niigata area. (a)-(c) Y4O, Y4R, G4U, respectively with original branching conditions. (d)-(f) Y4O, Y4R, G4U, respectively with branching condition C_3. 91

List of Tables

2.1 Surface scattering models 24
2.2 Dihedral scattering models 28
2.3 Volume scattering models 31
2.4 Unitary rotations of coherency matrix 34
2.5 Analysis of negative power problem 36
2.6 Similarity parameter analysis 38

3.1 Classification accuracies of selected land-covers in percentage (%) 45
3.2 Classification accuracies of selected land-covers in percentage (%) 50

4.1 Normalized scattering powers mean (in %) over the selected urban patches of Radarsat-2 Quebec City image 60
4.2 Percentage (%) of negative power pixels for Radarsat-2 Quebec City image 61
4.3 Normalized scattering powers mean (in %) over the selected desert patches of AIRSAR Death Valley image 62
4.4 Percentage (%) of negative power pixels for AIRSAR Death Valley image 63

5.1 Normalized scattering powers mean (in %) over selected land-cover patches of Radarsat-2 San Francisco image (For all the three decomposition methods, An *et al.* [88] volume scattering matrix is used) 72
5.2 Percentage (%) of negative power pixels by different methods with An *et al.* [88] volume scattering model for Radarsat-2 San Francisco image . . . 73
5.3 Normalized scattering powers mean (in %) over selected urban patches of UAVSAR Hayward image 75
5.4 Percentage(%) of negative power pixels by different methods with An *et al.* [88] volume scattering model for UAVSAR Hayward image 76

6.1 Normalized scattering powers mean (in %) over selected land-cover patches of Radarsat-2 San Francisco image 82

6.2 Percentage (%) of pixels satisfying different dominant dihedral branching conditions for selected urban patches 87
6.3 Means of normalized P_d (in %) over selected urban patches of Radarsat-2 San Francisco image 89
6.4 Means of normalized P_d (in %) over selected urban patches of UAVSAR Hayward image 90
6.5 Means of normalized P_d (in %) over selected urban patches of PiSAR Niigata image 92
6.6 Percentage (%) of pixels satisfying different dominant surface scattering branching conditions for selected ocean patches 92
6.7 Means of normalized P_s (in %) over selected ocean patches of San Francisco and Hayward images 93

Chapter 1

Introduction

Nowadays imaging radars are playing a crucial role in the investigation of Earth and other celestial bodies. This can be done through the analysis of data that is acquired from an overhead perspective through the transmission and reception of electromagnetic waves of microwave spectrum [1]- [5]. In this purpose, over the past three decades, polarimetric synthetic aperture radar (PolSAR) has been in the service to the mankind [6]- [14]. PolSAR is recognized as the most powerful tool to acquire high resolution microwave images of Earth surface through integrating the concept of synthetic aperture radar (SAR) with the vector nature of polarized electromagnetic wave and the underlying target. In SAR, a fine resolution in azimuth direction is achieved by 'synthesizing' a larger virtual aperture of the antenna. The radar antenna which acts like a single array element of the antenna is mounted on a moving platform. The platform motion is utilized to move this single element through successive element position on a known trajectory to form the complete array. At each element position along the path, a pulse is transmitted and the scattered wave from the target received. When this single element has traveled across the length of the complete array, the received backscattered signal from each element position is coherently combined to create the effect of a large phased array antenna. The SAR system thus synthesizes a virtual aperture equal to the length of phased array antenna that is much larger than the physical length of the actual antenna [3]- [4]. On the other hand, to obtain a enhanced resolution in range direction, pulse compression technique is utilized [15]. PolSAR upgrades the capacities of SAR by introducing polarimetry to it. Polarimetry is the method of accessing, processing and investigating the state of polarization of an electromagnetic field. In fundamental terms, SAR framework can transmit and receive a single polarization of the electromagnetic wave. However, to express the polarization state of a electromagnetic wave, two orthogonal polarization basis vectors are required [3]. A fully polarimetric SAR system transmits two orthogonal polarizations and coherently receives by dual orthogonal polarized channels. Since the polarization information present in the

backscattered wave is sensitive to the geometrical structure, orientation and shape of a given target, a PolSAR system greatly helps in extracting the significant information of the target or scatterer.

1.1 Polarimetric SAR Data Representation

The scattering process occurring at the target can be described by relating the complex amplitudes of incident ($\underline{E}_S$) and backscattered ($\underline{E}_I$) fields as [1], [3]

$$\underline{E}_S = [S]\,\underline{E}_I. \tag{1.1}$$

Here matrix $[S]$ is called the scattering matrix. Taking the most common choice of two orthogonal basis vectors of linear polarization, the fully polarimetric scattering matrix can be expressed as

$$[S] = \begin{bmatrix} S_{HH} & S_{HV} \\ S_{VH} & S_{VV} \end{bmatrix}, \tag{1.2}$$

where S_{ij} are the complex scattering coefficients, and 'H' and 'V' stand for horizontal and vertical polarizations, respectively. The diagonal elements of scattering matrix are 'co-polar' terms since they have the same polarization for scattered and incident waves, while the off-diagonal elements relate the orthogonal polarizations and hence called 'cross-polar' terms.

1.1.1 Coherency and Covariance Matrices

The scattering matrix is generally used to express a pure or single target as it produces a coherent averaging of reflected waves at each instant without any external disturbance phenomena [1]. However, pure target case is an ideal scenario, since even the time fluctuation of the target exposure affects the backscattering. Flow of wind and stresses generated by the temperature and pressure gradients can vary natural targets. Therefore, in real or practical scenario, the concept of distributed targets is more relevant. The concept of distributed targets arises from the fact that radar targets are situated in a dynamically changing environment. When these targets are illuminated by the monochromatic plane wave of a fixed frequency and polarization, the backscattered returns will be no longer coherent in nature. These returns are analogous to partially polarized wave, and can be analyzed as the time averaged samples of scattering from a set of different single targets. This set of single targets is called the distributed target. The scattering from distributed target can be better analyzed when the target is described by the second order moments

of the fluctuations which leads us towards the polarimetric coherency and covariance matrices.

Coherency Matrix ($[T]$)

The fully polarimetric coherency matrix $[T]$ is generated by the outer product of the Pauli target vector '$\underline{k}$' with its conjugate transpose '$\underline{k}^{*\mathrm{T}}$'. Pauli target vector can be constructed with the linear combination of trace of complex Pauli spin matrices [1] as

$$\underline{k} = \frac{1}{2}\mathrm{Tr}\left([S]\,\psi_{\mathrm{P}}\right), \tag{1.3}$$

where Tr denotes the trace of a matrix and ψ_{P} is a set of 2×2 complex Pauli spin matrix basis set [1], given by

$$\psi_{\mathrm{P}} = \left\{ \sqrt{2}\begin{bmatrix}1 & 0\\ 0 & 1\end{bmatrix} \sqrt{2}\begin{bmatrix}1 & 0\\ 0 & -1\end{bmatrix} \sqrt{2}\begin{bmatrix}0 & 1\\ 1 & 0\end{bmatrix} \sqrt{2}\begin{bmatrix}0 & j\\ -j & 0\end{bmatrix} \right\}. \tag{1.4}$$

Pauli target vector ($\underline{k}$) can be computed from (1.3) and (1.4) as

$$\underline{k} = \frac{1}{\sqrt{2}}\begin{bmatrix} S_{\mathrm{HH}}+S_{\mathrm{VV}} & S_{\mathrm{HH}}-S_{\mathrm{VV}} & S_{\mathrm{HV}}+S_{\mathrm{VH}} & j\left(S_{\mathrm{HV}}-S_{\mathrm{VH}}\right)\end{bmatrix}^{\mathrm{T}}. \tag{1.5}$$

The aforementioned equation (1.5) describes the Pauli feature vector for bistatic scattering case. However, at present, most of the airborne and spaceborne PolSAR systems use a single antenna to transmit and receive electromagnetic waves which represents a monostatic scattering case [15]. For monostatic configuration, the scattering matrix becomes symmetrical, i.e., $S_{\mathrm{HV}} = S_{\mathrm{VH}}$. Thus, the 4-dimensional Pauli feature vector is reduced to 3-dimensional as given by

$$\underline{k} = \frac{1}{\sqrt{2}}\begin{bmatrix} S_{\mathrm{HH}}+S_{\mathrm{VV}} & S_{\mathrm{HH}}-S_{\mathrm{VV}} & 2S_{\mathrm{HV}}\end{bmatrix}^{\mathrm{T}}. \tag{1.6}$$

From (1.6), the 3×3 coherency matrix can be generated as

$$\begin{aligned}[T] = \underline{k}\cdot\underline{k}^{*\mathrm{T}} &= \begin{bmatrix} T_{11} & T_{12} & T_{13}\\ T_{12}^{*} & T_{22} & T_{23}\\ T_{13}^{*} & T_{23}^{*} & T_{33}\end{bmatrix}\\ &= \begin{bmatrix} \frac{1}{2}\left|S_{\mathrm{HH}}+S_{\mathrm{VV}}\right|^{2} & \frac{1}{2}\left(S_{\mathrm{HH}}+S_{\mathrm{VV}}\right)\left(S_{\mathrm{HH}}-S_{\mathrm{VV}}\right)^{*} & \left(S_{\mathrm{HH}}+S_{\mathrm{VV}}\right)S_{\mathrm{HV}}^{*}\\ \frac{1}{2}\left(S_{\mathrm{HH}}-S_{\mathrm{VV}}\right)\left(S_{\mathrm{HH}}+S_{\mathrm{VV}}\right)^{*} & \frac{1}{2}\left|S_{\mathrm{HH}}-S_{\mathrm{VV}}\right|^{2} & \left(S_{\mathrm{HH}}-S_{\mathrm{VV}}\right)S_{\mathrm{HV}}^{*}\\ S_{\mathrm{HV}}\left(S_{\mathrm{HH}}+S_{\mathrm{VV}}\right)^{*} & S_{\mathrm{HV}}\left(S_{\mathrm{HH}}-S_{\mathrm{VV}}\right)^{*} & 2\left|S_{\mathrm{HV}}\right|^{2}\end{bmatrix}.\end{aligned} \tag{1.7}$$

The diagonal terms of coherency matrix represent the correlation of Pauli target vector

components with themselves. Hence, the diagonal terms are real quantity in nature and constitute the total power or *span*. The remaining off-diagonal terms of coherency matrix represent all possible combination of correlation between different Pauli target vector components [1].

Covariance Matrix ($[C]$)

The fully polarimetric covariance matrix can be obtained with the help of Lexicographic target vector. Lexicographic target vector can be constructed by the linear combination of trace of Lexicographic basis matrix set ψ_{L} [1] as

$$\underline{\Omega} = \frac{1}{2}\mathrm{Tr}\left([S]\,\psi_{\mathrm{L}}\right). \tag{1.8}$$

The Lexicographic basis matrix set ψ_{L} is given by

$$\{\psi_{\mathrm{L}}\} = \left\{ 2\begin{bmatrix}1 & 0\\ 0 & 0\end{bmatrix}\ 2\begin{bmatrix}0 & 1\\ 0 & 0\end{bmatrix}\ 2\begin{bmatrix}0 & 0\\ 1 & 0\end{bmatrix}\ 2\begin{bmatrix}0 & 0\\ 0 & 1\end{bmatrix} \right\}, \tag{1.9}$$

and the corresponding Lexicographic target vector $\underline{\Omega}$ can be obtained as

$$\underline{\Omega} = \begin{bmatrix} S_{\mathrm{HH}} & S_{\mathrm{HV}} & S_{\mathrm{VH}} & S_{\mathrm{VV}} \end{bmatrix}^{\mathrm{T}}. \tag{1.10}$$

For monostatic radar configuration, the 3-dimensional Lexicographic feature vector is given by

$$\underline{\Omega} = \begin{bmatrix} S_{\mathrm{HH}} & \sqrt{2}S_{\mathrm{HV}} & S_{\mathrm{VV}} \end{bmatrix}^{\mathrm{T}}. \tag{1.11}$$

The fully polarimetric covariance matrix $[C]$ can be generated by the outer product of Lexicographic target vector '$\underline{\Omega}$' with its conjugate transpose '$\underline{\Omega}^{*\mathrm{T}}$' as

$$[C] = \underline{\Omega}\cdot\underline{\Omega}^{*\mathrm{T}} = \begin{bmatrix} C_{11} & C_{12} & C_{13}\\ C_{12}^{*} & C_{22} & C_{23}\\ C_{13}^{*} & C_{23}^{*} & C_{33}\end{bmatrix} = \begin{bmatrix} |S_{\mathrm{HH}}|^2 & \sqrt{2}\left(S_{\mathrm{HH}}S_{\mathrm{HV}}^{*}\right) & \left(S_{\mathrm{HH}}S_{\mathrm{VV}}^{*}\right)\\ \sqrt{2}\left(S_{\mathrm{HV}}S_{\mathrm{HH}}^{*}\right) & 2|S_{\mathrm{HV}}|^2 & \sqrt{2}\left(S_{\mathrm{HV}}S_{\mathrm{VV}}^{*}\right)\\ \left(S_{\mathrm{VV}}S_{\mathrm{HH}}^{*}\right) & \sqrt{2}\left(S_{\mathrm{VV}}S_{\mathrm{HV}}^{*}\right) & |S_{\mathrm{VV}}|^2\end{bmatrix}. \tag{1.12}$$

Like coherency matrix, the diagonal terms of covariance matrix are also real quantity and constitute the total power or *span*. However, the remaining off-diagonal terms represent all possible combination of correlation between different Lexicographic target vector components. The polarimetric coherency and covariance matrices are interchangeable through the following unitary transformation [1].

$$[T] = [U]_{\mathrm{L}\to\mathrm{P}}\,[C]\,[U]^{-1}_{\mathrm{L}\to\mathrm{P}}, \tag{1.13}$$

where $[U]_{\mathrm{L}\to\mathrm{P}}$ is the unitary matrix for Lexicographic covariance matrix to Pauli coherency matrix conversion, given by

$$[U]_{\mathrm{L}\to\mathrm{P}} = \frac{1}{\sqrt{2}}\begin{bmatrix} 1 & 0 & 1 \\ 1 & 0 & -1 \\ 0 & \sqrt{2} & 0 \end{bmatrix}. \tag{1.14}$$

The total power or *span* for both coherency and covariance matrices can be computed as

$$\begin{aligned} Span &= |S_{\mathrm{HH}}|^2 + 2\,|S_{\mathrm{HV}}|^2 + |S_{\mathrm{VV}}|^2 \\ &= T_{11} + T_{22} + T_{33} \\ &= C_{11} + C_{22} + C_{33}. \end{aligned} \tag{1.15}$$

Both coherency and covariance matrices are positive semidefinite Hermitian in nature. A matrix $[A]$ is said to be Hermitian if it follows $[A]^{*\mathrm{T}} = [A]$. The eigenvalues of a positive semidefinite Hermitian matrix are always real and non-negative, and remain same under unitary transformations. That is why, coherency and covariance matrices possess same eigenvalues, since they are related through a unitary transformation. The only difference between these two matrices is in the way of representing polarimetric information. The covariance matrix elements are directly related to the observed data, whereas coherency matrix elements can be interpreted in terms of physical scattering mechanisms. The ease of interpretation of the scattering phenomena via formulation of a decomposition scheme through coherency matrix is the main reason for its extensive use in literature over the covariance matrix.

1.2 Information Extraction from PolSAR Data

The bridge between PolSAR measurements and the physical parameters of the scatterer under study can be established by the so-called target decomposition theorems. Target decomposition theorems have their roots in the work of Chandrasekhar [16] on light scattering by small anisotropic particles and first formalized by the Huynen [17]. Target decomposition theorems can be broadly classified into coherent and incoherent decomposition methods.

1.2.1 Coherent Decomposition Methods

Coherent decomposition methods express the measured scattering matrix into combination of canonical scattering mechanisms. In this category, the main contributions are reported by Pauli [1], Krogager [18], Krogager and Boerner [19], Cameron [20], Corr

and Rodrigues [21], and Touzi and Charbonneau [22]. Among coherent decomposition techniques, Pauli decomposition is the most frequently used method by the polarimetric radar community. Pauli decomposition method expresses the scattering matrix into sum of Pauli spin matrices [1]. Each Pauli spin matrix is associated with an elementary scattering mechanism. The Pauli decomposition method can be expressed as

$$\begin{bmatrix} S_{\mathrm{HH}} & S_{\mathrm{HV}} \\ S_{\mathrm{HV}} & S_{\mathrm{VV}} \end{bmatrix} = \frac{a}{\sqrt{2}} \begin{bmatrix} 1 & 0 \\ 0 & 1 \end{bmatrix} + \frac{b}{\sqrt{2}} \begin{bmatrix} 1 & 0 \\ 0 & -1 \end{bmatrix} + \frac{c}{\sqrt{2}} \begin{bmatrix} 0 & 1 \\ 1 & 0 \end{bmatrix}, \tag{1.16}$$

where a, b, and c are the complex quantities, given by

$$a = \frac{S_{\mathrm{HH}} + S_{\mathrm{VV}}}{\sqrt{2}},\ b = \frac{S_{\mathrm{HH}} - S_{\mathrm{VV}}}{\sqrt{2}}, \text{and } c = \sqrt{2} S_{\mathrm{HV}}. \tag{1.17}$$

The three matrices on the right hand side of (1.16) denote three scattering mechanisms. The first matrix corresponds to single- or odd-bounce scattering from a plane surface, whereas the second and third matrix corresponds to double- or even-bounce scattering from a dihedral plane with a relative orientation of 0° and 45°, respectively [1]. The Pauli decomposed RGB (Red Green Blue) images are generally used in literature for reference purpose. The general color coding used for Pauli decomposed images are as red: $|b|^2$, green: $|c|^2$, blue: $|a|^2$.

1.2.2 Incoherent Decomposition Methods

Coherent decomposition methods are mainly suitable for pure targets since they based on the decomposition of measured scattering matrix. However, most of the targets in real scenario are distributed in nature, that is why, incoherent decomposition methods become more appropriate to be used for decomposition [23]. Incoherent decomposition techniques utilize the information contained in the coherency or covariance matrix. Incoherent decomposition techniques can be further divided into two main groups, eigenvector-based decomposition and model-based decomposition [1]. Eigenvector decomposition methods are based on the quantitative analysis of eigenvalues and eigenvectors of the coherency or covariance matrix, while model-based methods decompose the coherency or covariance matrix into the summation of physical scattering models.

1.2.2.1 Eigenvector-based decomposition

Eigenvectors and eigenvalues can be parameterized through decomposing the measured coherency matrix $[T]$ as [24]- [31]

$$[T] = [U][\Sigma][U]^{*\mathrm{T}}, \tag{1.18}$$

where $[\Sigma]$ is the 3×3 diagonal eigenvalues matrix of $[T]$, given by

$$[\Sigma] = \begin{bmatrix} \lambda_1 & 0 & 0 \\ 0 & \lambda_2 & 0 \\ 0 & 0 & \lambda_3 \end{bmatrix}_{\lambda_1 \geq \lambda_2 \geq \lambda_3} \tag{1.19}$$

and $[U]$ is the 3×3 eigenvectors matrix of $[T]$, which can be presented as

$$[U] = \begin{bmatrix} \underline{u_1} & \underline{u_2} & \underline{u_3} \end{bmatrix} = \begin{bmatrix} \cos\alpha_1 & \cos\alpha_2 & \cos\alpha_3 \\ \sin\alpha_1 \cos\beta_1 e^{\delta_1} & \sin\alpha_2 \cos\beta_2 e^{\delta_2} & \sin\alpha_3 \cos\beta_3 e^{\delta_3} \\ \sin\alpha_1 \sin\beta_1 e^{\gamma_1} & \sin\alpha_2 \sin\beta_2 e^{\gamma_2} & \sin\alpha_3 \sin\beta_3 e^{\gamma_3} \end{bmatrix}. \tag{1.20}$$

In (1.20), $\underline{u_1}$, $\underline{u_2}$, and $\underline{u_3}$ are the three unit orthogonal eigenvectors. The parameters α_i, β_i, γ_i, and δ_i, $i = \{1,2,3\}$, are the real angles derived from the eigenvectors of $[T]$. With this representation, the coherency matrix $[T]$ can be expanded into sum of three independent targets as

$$[T] = \sum_{i=1}^{3} \lambda_i \underline{u_i} \cdot \underline{u_i}^{*T} = \lambda_1 \underline{u_1} \cdot \underline{u_1}^{*T} + \lambda_2 \underline{u_2} \cdot \underline{u_2}^{*T} + \lambda_3 \underline{u_3} \cdot \underline{u_3}^{*T} = T_1 + T_2 + T_3. \tag{1.21}$$

The unitary eigenvector $\underline{u_i}$ gives the information about the type of scattering mechanism, while the relative magnitude of that scattering mechanism is specified by the corresponding eigenvalue λ_i. A single non-zero eigenvalue corresponds to a pure target, while if all the three eigenvalues are equal, then it describes a random target. Between these two cases, partial targets exists where the eigenvalues are nonzero and non-equal.

(a) Entropy/Alpha $(H/\overline{\alpha})$ Decomposition

As discussed in Section 1.2.2.1, the eigenvectors and eigenvalues can be used to decompose the coherency matrix into a diagonal form. The 3×3 eigenvalues matrix $[\Sigma]$ can be expressed as given in (1.19), whereas the 3×3 eigenvectors matrix is described in (1.20). With the parameterization of $[U]$ in column vectors, Cloude and Pottier [27] presented a statistical model to find out the dominant 'average' scattering mechanism in a single resolution cell. The eigenvalues and eigenvectors are used as parameters to describe this dominant 'average' scattering mechanism.

Alpha (α) angle

Within eigenvectors parameters, α_i is the main parameter to identify the scattering mechanism. However, the parameters α_1, α_2, and α_3 are not independent. Therefore, it is better to describe the average scattering mechanism by mean alpha angle $(\overline{\alpha})$, given by

$$\overline{\alpha} = \sum_{i=1}^{3} P_i \alpha_i = P_1 \alpha_1 + P_2 \alpha_2 + P_3 \alpha_3, \tag{1.22}$$

where P_i are the pseudo probabilities or normalized eigenvalues, given by

$$P_i = \frac{\lambda_i}{\sum_{i=1}^{3} \lambda_i} = \frac{\lambda_i}{\lambda_1 + \lambda_2 + \lambda_3}. \tag{1.23}$$

The parameter $\overline{\alpha} = 0^\circ$ corresponds to surface scattering from geometrical optics, while $\overline{\alpha} = 90^\circ$ corresponds to the dihedral scattering from metallic surfaces. The median of these values, $(\overline{\alpha} = 45^\circ)$ can be found in the area of dipole scattering or single scattering by the cloud of anisotropic particles. The continuous range between these two extremities $(0^\circ \leq \overline{\alpha} \leq 90^\circ)$ is occupied by the Bragg surface scattering $\rightarrow$ dipole scattering $\rightarrow$ double-bounce scattering from two dielectric surfaces [27].

Entropy (H)

The polarimetric entropy (H) defines the degree of statistical disorder for distributed or partially polarized scatterers. H can be described as

$$H = -\sum_{i=1}^{3} P_i \, log_3 \, (P_i) = -P_1 \, log_3 \, P_1 - P_2 \, log_3 \, P_2 - P_3 \, log_3 \, P_3. \tag{1.24}$$

The first limiting value of polarimetric entropy, i.e. $H = 0$, describes the single or point scattering case where only one eigenvalue is present. The second limiting value, $H = 1$, describes the completely depolarized random scattering phenomenon. The low entropy values $(H < 0.3)$ are considered as weakly depolarized [27]. For these cases, the dominant scattering mechanism can be easily found out. However, if the entropy is high, then the target is depolarizing and the mixture of scattering mechanisms must be considered from the complete eigenvalue spectrum. As the entropy value reaches to its maximum, it is more difficult to identify distinguishable classes from polarimetric observations.

$H/\overline{\alpha}$ decomposition

Based on the values of H and $\overline{\alpha}$, Cloude and Pottier [27] construct a 2-dimensional H/α plane as shown in Figure 1.1. The 2-D $H/\overline{\alpha}$ plane is subdivided into nine zones. These

zones represent different types of nine classes based on the characteristics of different scattering behavior. General properties of scattering mechanisms (related with the values of H and $\overline{\alpha}$) are used to set the boundaries of $H/\overline{\alpha}$ plane.

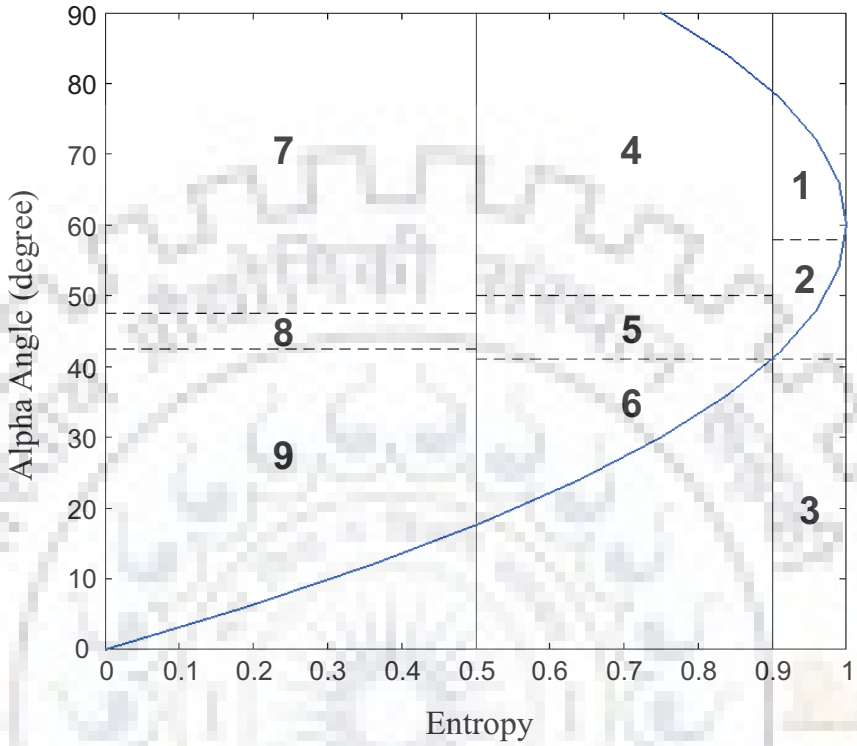

Figure 1.1: $H/\overline{\alpha}$ plane.

Zone 9: Low entropy surface scattering

This zone accommodates the low entropy scattering processes with $\overline{\alpha} < 42.5°$. Surface scattering from geometrical and physical optics, specular scattering and Bragg surface scattering which do not involve 180° phase sift between S_{HH} and S_{VV} are included in this zone.

Zone 8: Low entropy dipole scattering

The boundaries for this zone are kept at $H < 0.5$ and $42.5° < \overline{\alpha} < 47.5°$. This zone includes scattering from strongly correlated mechanisms those have large amplitude imbalance between S_{HH} and S_{VV}. Scattering from anisotropic scattering elements with strongly correlated orientation like in the case of vegetation would come under this category.

Zone 7: Low entropy multiple scattering

This zone is characterized with low entropy with high $\overline{\alpha}$ values ($\overline{\alpha} > 42.5°$). Low entropy even bounce scatterings with isolated dielectric and metallic dihedral scatterers are the example of the event occurring in this zone.

Zone 6: Medium entropy surface scattering

Changes in surface roughness and canopy propagation effects increases the entropy H through secondary wave propagation and scattering mechanisms. This zone includes the scatterings from surfaces with slope and large scale roughness.

Zone 5: Medium entropy vegetation scattering

This zone accounts for the scattering from vegetation with moderate correlation of anisotropic scatterers' orientations.

Zone 4: Medium entropy multiple scattering

This zone includes the dihedral scattering in moderate entropy environment. This type of scattering can be seen in the forest areas where double-bounce scattering is obtained after penetration through a canopy. Another scenario where this type scattering can be seen is the urban area with random orientation of double-bounce structures.

Zone 3: High entropy surface scattering

This is a non-feasible zone. Surface scattering in high entropy region ($H > 0.9$) is not distinguishable.

Zone 2: High entropy vegetation scattering

Multiple scattering from a cloud of low loss symmetric particles or single scattering from a cloud of anisotropic needle like particles come under high entropy volume scattering case.

Zone 1: High entropy multiple scattering

This zone includes the scattering from vegetation with well developed branch and crown structure. Though the entropy value is high ($H > 0.9$), the dihedral scattering mechanism is still possible to distinguish in this region.

1.2.2.2 Model-Based Decomposition

The model-based decomposition of PolSAR data was first introduced by Freeman and Durden in their three-component scattering model, popularly known as Freeman-Durdens' decomposition method [32]- [33]. The basic idea was to decompose the measured covariance or coherency matrix into a linear sum of three scattering mechanisms, viz. single or odd bounce scattering from a moderately rough surface, double or even bounce scattering from two orthogonal dielectric surfaces, and volume scattering from a cloud of oriented dipoles. Brief descriptions of these three scattering models are given below.

Single-Bounce Scattering

Odd- or single-bounce or surface scattering mechanism is based on Bragg scattering from a moderately rough surface [33]. Bragg scattering describes the effects of the reflection of electromagnetic waves from the periodic structures whose distances are in the range of wavelength. This type of scattering can be found in the areas of bare soil and sea surface. The scattering matrix for a Bragg surface has the form

$$[S]_{\mathrm{s}} = \begin{bmatrix} R_{\mathrm{H}} & 0 \\ 0 & R_{\mathrm{V}} \end{bmatrix}, \tag{1.25}$$

where R_{H} and R_{V} are the reflection coefficients for horizontally and vertically polarized waves. The Reflection coefficients R_{H} and R_{V} can be defined as

$$R_{\mathrm{H}} = \frac{\cos\phi - \sqrt{\varepsilon_{\mathrm{r}} - \sin^2\phi}}{\cos\phi + \sqrt{\varepsilon_{\mathrm{r}} - \sin^2\phi}}, \text{ and } R_{\mathrm{V}} = \frac{(\varepsilon_{\mathrm{r}} - 1)\left\{\sin^2\phi - \varepsilon_{\mathrm{r}}\left(1 + \sin^2\phi\right)\right\}}{\left(\varepsilon_{\mathrm{r}}\cos\phi + \sqrt{\varepsilon_{\mathrm{r}} - \sin^2\phi}\right)^2}. \tag{1.26}$$

Here ϕ and ε_{r} are the local incidence angle and relative dielectric constant of the surface, respectively. The coherency matrix corresponds to single-bounce scattering mechanism [33] can be written as

$$[T]_{\mathrm{s}} = \begin{bmatrix} 1 & \beta^* & 0 \\ \beta & |\beta|^2 & 0 \\ 0 & 0 & 0 \end{bmatrix}, \text{ where } \beta = \frac{R_{\mathrm{H}} - R_{\mathrm{V}}}{R_{\mathrm{H}} + R_{\mathrm{V}}}. \tag{1.27}$$

Double-Bounce Scattering

Even- or double-bounce or dihedral scattering mechanism is usually modeled by scattering from a pair of orthogonal surfaces having different dielectric constants [33]. Such type of scattering can be found through the ground-tree trunk interaction or ground-wall interaction. Double-bounce scattering matrix has the form

$$[S]_{\mathrm{d}} = \begin{bmatrix} e^{2j\gamma_{\mathrm{H}}} R_{\mathrm{TH}} R_{\mathrm{GH}} & 0 \\ 0 & e^{2j\gamma_{\mathrm{V}}} R_{\mathrm{TV}} R_{\mathrm{GV}} \end{bmatrix}, \tag{1.28}$$

where $e^{2j\gamma_{\mathrm{H}}}$ and $e^{2j\gamma_{\mathrm{V}}}$ are the propagation factors. γ_{H} and γ_{V} are the complex coefficients that represent propagation attenuation and phase change effects, respectively. R_{TH} and R_{TV} are the reflection coefficients of the vertical structure for horizontal and vertical polarized wave, whereas R_{GH} and R_{GV} are the reflection coefficients of the horizontal

structure for horizontal and vertical polarized wave, respectively, given by

$$R_{\mathrm{iH}} = \frac{\cos\phi_{\mathrm{i}} - \sqrt{\varepsilon_{\mathrm{i}} - \sin^2\phi_{\mathrm{i}}}}{\cos\phi_{\mathrm{i}} + \sqrt{\varepsilon_{\mathrm{i}} - \sin^2\phi_{\mathrm{i}}}}, \text{ and } R_{\mathrm{iV}} = \frac{\varepsilon_{\mathrm{i}}\cos\phi_{\mathrm{i}} - \sqrt{\varepsilon_{\mathrm{i}} - \sin^2\phi_{\mathrm{i}}}}{\varepsilon_{\mathrm{i}}\cos\phi_{\mathrm{i}} + \sqrt{\varepsilon_{\mathrm{i}} - \sin^2\phi_{\mathrm{i}}}}. \tag{1.29}$$

Here $\mathrm{i} \in \{\mathrm{G}, \mathrm{T}\}$, ε_{G} and ε_{T} are the dielectric constants for horizontal and vertical structure, and ϕ_{G} and ϕ_{V} are the corresponding incidence angles, respectively. The coherency matrix for the double-bounce scattering mechanism is given by

$$[T]_{\mathrm{d}} = \begin{bmatrix} |\alpha|^2 & \alpha & 0 \\ \alpha^* & 1 & 0 \\ 0 & 0 & 0 \end{bmatrix}, \tag{1.30}$$

where

$$\alpha = \frac{R_{\mathrm{TH}}R_{\mathrm{GH}} + e^{2j(\gamma_{\mathrm{V}} - \gamma_{\mathrm{H}})}R_{\mathrm{TV}}R_{\mathrm{GV}}}{R_{\mathrm{TH}}R_{\mathrm{GH}} - e^{2j(\gamma_{\mathrm{V}} - \gamma_{\mathrm{H}})}R_{\mathrm{TV}}R_{\mathrm{GV}}}. \tag{1.31}$$

Volume Scattering

Volume scattering is modeled by a cloud of randomly oriented very thin dipoles [33]. The scattering matrix for horizontal and vertical dipoles can be given as

$$[S]_{\mathrm{dipole(H)}} = \begin{bmatrix} 1 & 0 \\ 0 & 0 \end{bmatrix}, \text{ and } [S]_{\mathrm{dipole(V)}} = \begin{bmatrix} 0 & 0 \\ 0 & 1 \end{bmatrix}. \tag{1.32}$$

The scattering matrix of an oriented dipole by an angle θ around the radar line of sight can be derived as

$$[S(\theta)] = \begin{bmatrix} \cos\theta & \sin\theta \\ -\sin\theta & \cos\theta \end{bmatrix} [S]_{\mathrm{dipole}} \begin{bmatrix} \cos\theta & -\sin\theta \\ \sin\theta & \cos\theta \end{bmatrix}. \tag{1.33}$$

The coherency matrix for volume scattering mechanism can be obtained by mathematical averaging of $[T(\theta)]$ with respect to the probability density function as

$$[T]_{\mathrm{v}} = \int_0^{2\pi} [T(\theta)]\, p(\theta)\, d\theta. \tag{1.34}$$

Here $[T(\theta)]$ is the coherency matrix corresponding to the scattering matrix given in (1.33), and $p(\theta)$ is the probability density function of the orientation angle of randomly oriented dipoles. For uniform probability density function ($p(\theta) = 1/2\pi$), the averaged volume scattering coherency matrix can be computed as [33]

$$[T]_{\mathrm{v}} = \frac{1}{4}\begin{bmatrix} 2 & 0 & 0 \\ 0 & 1 & 0 \\ 0 & 0 & 1 \end{bmatrix}. \tag{1.35}$$

Freeman-Durdens' Decomposition (FDD) Method

Freeman-Durdens' decomposition (FDD) method [33] can be mathematically described on the coherency matrix as

$$[T] = f_{\mathrm{s}}[T]_{\mathrm{s}} + f_{\mathrm{d}}[T]_{\mathrm{d}} + f_{\mathrm{v}}[T]_{\mathrm{v}}, \tag{1.36}$$

where $[T]_{\mathrm{s}}$, $[T]_{\mathrm{d}}$ and $[T]_{\mathrm{v}}$ are the coherency matrices for single-bounce, double-bounce and volume scattering mechanisms as described in (1.27), (1.30) and (1.35), and f_{s}, f_{d}, and f_{v} are the corresponding unknown scattering model coefficients, respectively. On comparing unknown model coefficients with the coherency matrix elements, following equations are obtained.

$$T_{11} = f_{\mathrm{s}} + f_{\mathrm{d}}|\alpha|^2 + \frac{f_{\mathrm{v}}}{2},\ T_{22} = f_{\mathrm{s}}|\beta|^2 + f_{\mathrm{d}} + \frac{f_{\mathrm{v}}}{4},$$
$$T_{33} = \frac{f_{\mathrm{v}}}{4},\ \text{and}\ T_{12} = f_{\mathrm{s}}\beta_{\mathrm{s}}^* + f_{\mathrm{d}}\alpha_{\mathrm{d}}. \tag{1.37}$$

As one can see, the aforementioned four equations have five unknowns. These unknowns can be solved using the criterion based on the sign of real part of $\left(S_{\mathrm{HH}}S_{\mathrm{VV}}^*\right)$, i.e. $\Re\left(S_{\mathrm{HH}}S_{\mathrm{VV}}^*\right)$. Sign of $\Re\left(S_{\mathrm{HH}}S_{\mathrm{VV}}^*\right)$ depends on the phase angle of $\left(S_{\mathrm{HH}}S_{\mathrm{VV}}^*\right)$. It has been shown that for odd number of scattering events, the elements S_{HH} and S_{VV} are in phase [34]. The positive phase angle results in positive sign for $\Re\left(S_{\mathrm{HH}}S_{\mathrm{VV}}^*\right)$ provided

$$\left|\Re\left(S_{\mathrm{HH}}S_{\mathrm{VV}}^*\right)\right| > \left|S_{\mathrm{HV}}\right|^2. \tag{1.38}$$

On the other hand, the even number of reflections result in nearly 180° phase shift between S_{HH} and S_{VV}. This out of phase condition results in negative values of $\Re\left(S_{\mathrm{HH}}S_{\mathrm{VV}}^*\right)$ [34]. However, the condition (1.38) will still be satisfied. For coherency matrix case, this criterion can be realized by checking the sign of $T_{11} - T_{22}$, since $T_{11} - T_{22} = 4\Re\left(S_{\mathrm{HH}}S_{\mathrm{VV}}^*\right)$ [35]. The positive values of $T_{11} - T_{22}$ indicate the dominant odd- or single-bounce scattering, while the negative values of $T_{11} - T_{22}$ indicate the dominant even- or double-bounce scattering.

For dominant single-bounce scattering case ($T_{11} - T_{22} > 0$), parameter α is assumed to be zero and the solution for the remaining unknown coefficients can be given as

$$f_v = 4T_{33},\ f_s = T_{11} - \frac{f_v}{2},\ \beta^* = \frac{T_{12}}{f_s},$$
$$\text{and } f_d = T_{22} - f_s|\beta|^2 - \frac{f_v}{4}. \tag{1.39}$$

For dominant double-bounce scattering case ($T_{11} - T_{22} \leq 0$), parameter β is assumed to be zero and the solution for the remaining unknown coefficients can be given as

$$f_v = 4T_{33},\ f_d = T_{22} - \frac{f_v}{4},\ \alpha = \frac{T_{12}}{f_d},$$
$$\text{and } f_s = T_{11} - f_d|\alpha|^2 - \frac{f_v}{2}. \tag{1.40}$$

The scattering powers for single-bounce (P_s), double-bounce (P_d), and volume (P_v) scattering mechanisms can be computed as

$$P_s = f_s\left(1+|\beta|^2\right),\ P_d = f_d\left(1+|\alpha|^2\right),\ \text{and } P_v = f_v. \tag{1.41}$$

As per the previous discussions, it can be seen that the eigenvector-based decomposition class has clear mathematical background since it is based on the statistical analysis of eigenvalues and eigenvectors of PolSAR coherency/covariance matrix. Constant expressions of eigenvalues and eigenvectors lead to a single decomposition solution. In contrast, the model-based decomposition method can obtain a variety of solutions by varying the physical scattering models. The conventional scattering models presented in FDD method [33] do not fit the actual PolSAR observations. Therefore, many deficiencies are inherited to the model-based decomposition method. These deficiencies received a great attention which stimulated the research in the development of effective model-based decomposition technique, and thereby many excellent works have been reported which are thoroughly discussed in the next chapter.

1.3 PolSAR Environmental Applications

The major application domain of PolSAR is in the remote sensing of environment. In this respect, SAR polarimetry is a broadly utilized strategy for capturing the critical information about the shape, orientation, and dielectric properties of the scatterer. The environmental applications of PolSAR used for mankind purpose can be broadly categorized into following domains.

1.3.1 Forestry

Forest plays an important role in the global carbon cycle as carbon sinks of the terrestrial ecosystem. The carbon sequestered or stored on the forest trees are mostly referred to as the biomass of the tree or forest. The primary function of biomass is described as its carbon sink capability, but it is also described as a carbon reservoir and carbon emitter, which mainly draws the attention of ecologists. The microwave interaction is sensitive to the roughness and physical geometry of forests. This, when combined with the polarization, results in a sensitivity of PolSAR backscatter to key biophysical variables such as crown size, leaf area index, tree height, and tree density. With the help of these biophysical parameters, major reservoir of world's carbon can be mapped and monitored quantitatively through forest mapping, biomass estimation, and forest change detection [36]- [40].

1.3.2 Agriculture

Agriculture is the pivotal sector of the world to fulfill the need of food. Timely availability of information regarding agriculture can play a vital role for taking crucial decisions on food security issues. Nowadays many countries in the world use PolSAR data to generate regular basis updates on crop production statistics. These statistics are used to achieve sustainable agriculture which is necessary to meet the world's increasing demand of food. Not only that, the agriculture is the backbone of many developing countries' economy like India. To maintain the stable flow of economy of these countries, PolSAR data has been used for crop health monitoring, crop discrimination, crop production forecasts, phenology determination, soil moisture estimation, and drought assessment [41]- [55].

1.3.3 Cryosphere

The cryosphere is the frozen water portion of the Earth's system, e.g. sea ice, river ice, glaciers, snow cover, and permafrost. The cryosphere is an intrinsic part of global climate system. Change in cryosphere distribution influences the water flow in world's major rivers which has a direct impact on human livelihood [56]. However, the research in this domain is often obstructed by the inaccessibility of data. In that case, PolSAR greatly helps in cryology and its relation to global climate change. With PolSAR data, many studies related to snow water equivalent, sea ice surface characterization, ice thickness estimation, land ice extinction, and snow volume estimation have been carried out [57]- [62]. By these studies, the global glacier recessions can be monitored which are the crucial indicators of the world's climate change.

1.3.4 Ocean

Applications of PolSAR data in this domain mainly include oil spill monitoring at ocean/sea surfaces, detection of metallic targets like ship, measurement of ocean surface slopes and directional wave spectra, determination of surface wind parameters, and tropical cyclone tracking [63]- [68]. The polarimetric parameters are affected by dielectric coefficient which helps in observing oil slick on the water surface. Whereas, by analyzing the change in scattering mechanism, ship like targets can be identified. The polarimetric parameters are sensitive to range and azimuth slopes of the scatterer. Using this sensitivity, the direction of ocean waves can be tracked which will serve as early waring system for the people living in nearby areas.

1.3.5 Urban

In recent years, urbanization is one of the most studied topics of research. The industrial revolution, growth of private sector, economic opportunities, and infrastructure facilities causes a rapid growth in urbanization. To accommodate this urbanization, land suitability should be properly observed. It has been estimated that more than 30% of urban population lives in slums and squatters. This has greatly caused many problems in crowding cities like lack of electricity, water lines, proper roads. Therefore, a proper management is required to provide adequate shelter and basic supplements that will improve the living standards of the inhabitants of urban areas. The proper tracking of urban areas is also required to monitor the environmental impacts of urban growth. On this matter, the PolSAR data has been utilized in many aspects such as urban planning, urban mapping, urban classification, urban growth monitoring, urban change detection, and population estimation.

1.3.6 Land-cover Classification

Land-cover classification or land-cover mapping is a process that quantifies the Earth surface into a series of thematic categories, like forest, water, urban, and paved surfaces etc. It is a key driver to understand the land-cover alteration process and its consequences. Understanding current land-covers and the way people use the land is an important global issue. Current land-cover condition and how they are changing can be easily measured through land-cover classification or mapping. With the advancement of technology and the availability of fully polarimetric spaceborne and airborne sensors [13], land-cover classification using PolSAR data has received a great attention [69]- [70]. In all above application areas, land-cover classification used as the first step to separate the region of interest from the rest of area. Moreover, the average scattering parameters used for

land-cover classification can be directly utilized for different PolSAR environmental applications.

1.4 Research Objectives and Problem Statement

Nowadays tracking the anthropogenic modifications of Earth surface and its effects on the global environmental change is an area of interest of international radar communities. To better understand the effects of land-cover and land-use change on the global Earth system, it is required to monitor the changes that occur, where and when they occur, and the rate at which they occur. On this issue, PolSAR data has many significant implications that can be used for land-cover classification or land-cover mapping in regional and global scales. Land-cover classification is one of the relevant environmental application that can be directly used for land-change detection, urban extraction, deforestation monitoring, damage assessment, and so on. That is why, it has been chosen as the main application area of the thesis.

Land-cover classification using PolSAR data has been researched over the past few decades, and many target decomposition categories have been developed. Among these categories, incoherent decomposition theorems always lead with better decomposition results, since most of the natural and man-made areas are time varying which corresponds to a distributed target or scatterer. Furthermore, between two main incoherent decomposition methods, model-based decomposition technique has been the most explored category since its inception [71]. Model-based decomposition technique is based on the simple mathematical approach and has a clear physical understanding. However, despite of its straightforward approach, model-based decomposition category still lacks of efficient decomposition methods for land-cover classification. This is because the model-based decomposition methods suffer from some inherited flaws. These flaws are briefly described next by relating their provenance to pioneer FDD method.

The primitive FDD method was based on the reflection symmetry assumption. Reflection symmetry [72]- [73] implies that the correlation between co- and cross-polarization component is zero, which restricts the full utilization of all the information contained in the coherency matrix. The elements representing the correlation between co- and cross-polarization accommodate the backscattering from incoherently scatting areas. Neglecting this information limits the applicability of FDD model in these areas [74]- [75]. Therefore, the cross-correlation terms should be properly modeled in the decomposition scheme to address the scattering from non-reflection symmetric or incoherently scattering areas.

The incoherently scattering areas depolarize the incident wave which results in cross-

polarization power. In FDD model, entire cross-polarization power is assigned to the volume scattering category which represents the scattering from the vegetation only. However, cross-polarization also gets generated from sloped terrains, azimuth tilts of the surfaces, and oriented man-made structures. Basically, cross-polarization refers to any process that causes coupling of energy between orthogonal states of polarization [2]. In FDD model, cross-polarization scatterings from all of the aforementioned regions are wrongly classified under volume scattering category, which makes FDD method to overestimate the volume scattering power. This overestimation of volume scattering power must be addressed for the correct interpretation of the scattering mechanisms.

The overestimation of volume scattering power results in negative scattering power contributions for other scattering mechanisms. The word negative power in the radar context arises from the fact that the radar cross-section which is proportional to the power received by the radar system for the given transmit and receive polarization can never be negative [76]. The sum of the contributions of all the scattering components is equal to the total power or *span* of the coherency matrix. Therefore, overestimation of one of the scattering mechanisms' power at any pixel may result in negative scattering powers for other scattering mechanisms at that pixel so that *span* remains constant. Presence of negative scattering powers indicate that the scattering mechanisms are not properly modeled. Simple and straightforward solution should be explored to mitigate the negative power problem of model-based decomposition methods.

Apart from the aforementioned deficiencies, another fact which draws attention is that FDD model results in an under-determined system. An under-determined system has fewer number of equations than the number of unknowns. Therefore, to solve for the extra unknowns, some assumptions and constraints have to be applied. These constraints are known as branching conditions, which decide the dominance of a scattering mechanism and accordingly some unknowns are fixed. For example, in case of FDD method, the branching condition is based on the sign of $T_{11} - T_{22}$. In model-based decomposition method, branching condition is used as the initial discriminator after which appropriate assumptions are applied. Inefficient branching condition propagates wrong assumption which can lead to misclassification. Therefore, efficiency of existing branching conditions used in current model-based decomposition methods needs to be investigated and new branching conditions should be explored to enhance the performance of model-based decomposition methods.

The aforementioned flaws restrict the performance of model-based decomposition category. The probable solutions to these problems are needed in order to utilize the model-based decomposition technique for land-cover applications. To achieve this objective, following tasks are attempted and accomplished successfully.

- Modeling of cross-polarization power generated from oriented urban areas.
- Utilizing unitary matrix rotations to optimize the use of coherency matrix elements.
- Removal of negative scattering powers.
- Investigation of branching conditions in model-based decomposition methods.

1.5 Organization of Thesis

This thesis aims at the development of some effective decomposition techniques to deal with major challenges of model-based decomposition methods. The complete thesis is organized in seven chapters. The first two chapters of the thesis describe the introduction and literature part. The next four working chapters start with a brief introduction to the concerned problem and motivation behind the study. Subsequently, the solution to the concerned problem is presented in each chapter. The experimental results are summarized and discussed at the end of the each chapter. Finally, the last chapter concluded the thesis. A brief discussion of each chapter is presented below:

Chapter 1 starts with a brief introduction of polarimetric SAR. The formulation of fully polarimetric scattering matrix is described followed by the generation of second order coherency and covariance matrices. Incoherent target decomposition techniques for information extraction are discussed further. Finally, research objectives with problem statement culminate the chapter.

A unique property of model-based decomposition category is its ability to easily accommodate the advancement. This advancement can be of many types, for example, development of new scattering models to fit the actual PolSAR observations, transformation of the conventional scattering models to deal with scattering mechanism ambiguity, finding uncomplicated solution to mitigate the negative power problem etc. In Chapter 2, a complete literature survey of the advancements in model-based decomposition category is provided. These advancements are grouped and discussed in a lucid manner.

The conventional model-based methods fail to efficiently discriminate between the vegetation and oriented urban areas. The reason behind this is the significant generation of cross-polarization power from oriented dihedral structures. A solution to this scattering mechanism ambiguity is provided in Chapter 3 where the cross-polarization power of oriented urban areas is modeled through rotated dihedral scattering mechanism.

In Chapter 4, special unitary SU(3) matrix group is exploited for coherency matrix transformations to decouple the energy between orthogonal states of polarization. This decoupling results in the minimization of the cross-polarization power along with the removal of some off-diagonal terms of coherency matrix. The unitary transformations

are utilized on the basis of underlying co-polar dominant scattering mechanism, so that the removed cross-polarization power is always concentrated on the underlying dominant co-polar scattering mechanism.

In Chapter 5, hybrid surface and dihedral scattering models are used along with selective unitary rotations to deal with negative power problem of model-based decomposition methods.

Under-determined equation system of model-based decomposition methods is discussed in Chapter 6. In the first part, new coherency matrix transformations are presented to transform the conventional model-based decomposition methods into a state of equal number of unknowns and equations. Whereas, in the second part of this chapter, along with the investigation of current branching conditions, a new efficient branching condition based on $\overline{\alpha}$ angle is proposed.

Finally, the contribution of this thesis is summarized in Chapter 7. The remaining challenges are further discussed in future scope section.

Chapter 2

Advancements in Model-Based Decomposition Category

In this chapter, significant advancements in the model-based decomposition technique are thoroughly explored. The four major problems of Freeman-Durdens' decomposition (FDD) [33] as discussed in Chapter 1 are not completely uncorrelated. That is why, a potential solution to one of the problem can also be an improvement factor for other problems. The flowchart of the advancements in model-based decomposition category is shown in Figure 2.1.

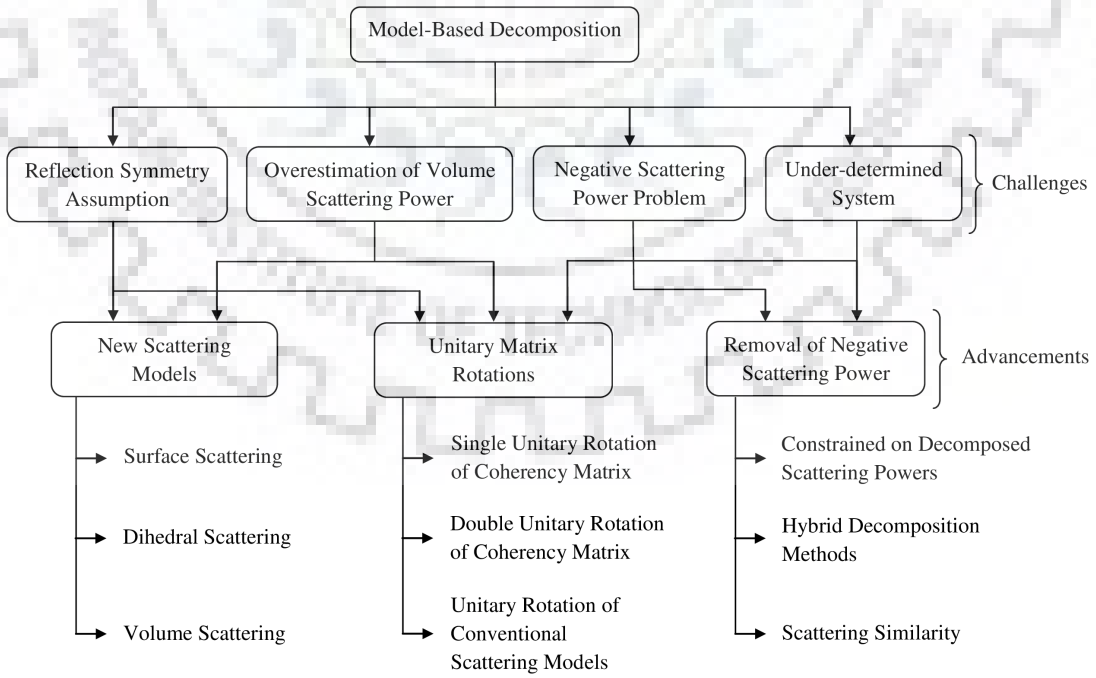

Figure 2.1: Flowchart of the advancements in model-based decomposition category.

As can be seen from Figure 2.1, the reported advancements can be broadly grouped in three main categories. Each category can be further broken into subcategories. These subcategories describe the approach adopted to deal with drawbacks of FDD method. Since the problems of FDD are interrelated, a single approach could be used to resolve more than one problems of FDD simultaneously. On the contrary, two or more approaches can be combined to tackle a single problem. The detailed description of the advancement categories is given below.

New Scattering Models

The first category of advancements can be grouped under the class where new scattering models are deployed to overcome the deficiencies of pioneer FDD method. This category can be further broken into the following subcategories.

1. **Surface Scattering Model**- The conventional surface scattering model was coherent in nature, therefore, does not account for the cross-polarization power. However, terrain slope and large surface roughness lead to cross-polarization generation [2]. This cross-polarization is a result of the depolarization of the incident wave. The advancements in this category mainly include the depolarization effect on surface scattering for various applications.

2. **Dihedral Scattering Models**- Like surface scattering model, conventional dihedral scattering model was also coherent in nature. However, in urban areas, the cross-polarization generation is more often. The man-made structures oriented away from the optimal radar illumination generate significant amount of cross-polarization [77]- [80]. In addition, thin wire targets like eaves, edges and window frames present in urban areas, and the randomness in distribution of various scatterers contribute to the cross-polarization scattering. These cross-polarization responses from various scatterers contribute to the overestimation of volume scattering power. This subsection includes all the major literature on new dihedral scattering model to account for the cross-polarization power generated from the urban areas.

3. **Volume Scattering Models**- The literature in this subcategory presented the improvements over pioneer FDD method through incorporation of new volume scattering models. Overestimation of volume scattering power is one of the major drawbacks of FDD method. The new volume scattering models intended to reduce this overestimation by better characterization of the vegetated areas. Apart from this, some literature incorporated adaptability in volume scattering model through uti-

lizing different polarimetric parameters like co-polarized power ratio, entropy, etc. to enhance the decomposition results.

Unitary Rotations of Coherency Matrix

Unitary rotation of coherency matrix was first proposed to compensate the effects of slope and orientation of the scatterer [77]- [80]. It involves the rotation of coherency matrix through special unitary matrices. Terrain azimuth slope and randomly distributed scatterers shift the polarization orientation angle (POA) from zero. This shift results in cross-polarization generation, which leads to scattering mechanism ambiguity. Unitary rotation enhances the performance of model-based decomposition methods by transforming the coherency matrix into a minimum cross-polarization state.

Elimination of Negative Power Problem

Negative scattering power is the undesirable outcome of model-based decomposition methods. The word negative power in the radar context arises from the fact that the radar cross section, which is proportional to the power received by the radar system can never be negative [76]. So that, for any circumstances, the scattering power cannot be negative. The negative scattering powers signify that the scattering models do not fit the actual PolSAR observations.

2.1 New Scattering Models

2.1.1 Surface Scattering Model

The conventional surface scattering model is based on the Bragg scattering from a moderately rough surface as described in Section 1.2.2.2. However, large scale roughness affects the surface scattering mechanism by reducing coherent scattering at the expense of incoherent scattering. To accommodate this incoherent scattering from depolarizing targets, conventional Bragg scattering model was first extended by Hajnsek *et al.* [81]. Hajnsek *et al.* [81] introduced depolarization effects in Bragg surface model by rotating surface scattering coherency matrix about an angle χ in the plane perpendicular to the scattering plane as

$$[T(\chi)]_{\mathrm{s}} = [U(\chi)]\,[T]_{\mathrm{s}}\,[U(\chi)]^{*T}, \tag{2.1}$$

where $[T(\chi)]_{\mathrm{s}}$ is the extended or X-Bragg surface scattering model, $[T]_{\mathrm{s}}$ is the conventional surface scattering coherency matrix as described in (1.27), χ is the rotation angle,

and $[U(\chi)]$ is the unitary rotation matrix given by

$$[U(\chi)] = \begin{bmatrix} 1 & 0 & 0 \\ 0 & \cos 2\chi & \sin 2\chi \\ 0 & -\sin 2\chi & \cos 2\chi \end{bmatrix}. \tag{2.2}$$

Integrating over probability distribution $p(\chi)$, the X-Bragg surface scattering model can be computed from (2.1) as

$$[T(\chi)]_s = \begin{bmatrix} 1 & \beta^* X_{12} & 0 \\ \beta X_{12} & |\beta|^2 X_{22} & 0 \\ 0 & 0 & X_{33} \end{bmatrix}, \tag{2.3}$$

where X_{12}, X_{22}, X_{33} are defined as

$$X_{12} = \int \cos 2\chi \; p(\chi) \, d\chi \tag{2.4}$$

$$X_{22} = \int \cos^2 2\chi \; p(\chi) \, d\chi \tag{2.5}$$

$$X_{33} = \int \sin^2 2\chi \; p(\chi) \, d\chi. \tag{2.6}$$

Later on, Lee *et al.* [35] used the X-Bragg surface scattering model to propose a generalized model-based decomposition method. The applications of X-Bragg or incoherent surface scattering model is not limited to land-cover classification only. In 2015, Yin *et al.* [82] utilized this model for ship and oil-spill observations, whereas Ponnurangam and Rao [83] incorporated X-Bragg model for soil moisture estimation.

Table 2.1: Surface scattering models

Paper	**Salient Points**	**Year**
Hajnsek *et al.* [81]	Proposed X-Bragg surface scattering model by introducing depolarization effects in Bragg surface model to accommodate incoherent scattering.	2003
Lee *et al.* [35]	Utilized X-Bragg surface scattering model to propose a generalized model-based decomposition scheme.	2014
Yin *et al.* [82]	Utilized X-Bragg model for ship and oil-spill observations.	2015
Ponnurangam and Rao [83]	Incorporated X-Bragg model with different orientation angle distributions for soil moisture estimation.	2017

2.1.2 Dihedral Scattering Model

After Freeman and Durdens' pioneer FDD method [33], the first effective contribution in model-based decomposition category was reported in 2005 by Yamaguchi *et al.* [74]. Yamaguchi *et al.* [74] introduced the helix scattering as the fourth component and extended FDD to four-component decomposition method, popularly known as Y4O. Helix scattering was first introduced by Krogager *et al.* in [84] where authors proposed the coherent decomposition of scattering matrix. Helix scattering accounts for the complex targets those transform the incoming linear polarization to circular polarization. Helix scattering can also be produced by two diplanes oriented at 45° with the relative displacement of $\lambda/8$ along line of sight. It also accumulates the backscattering from artificial targets for which two or more double-bounce scattering take place in a single resolution cell [84]. On the basis of backscattered circular polarization, helix scattering can be of two types, either left-handed or right-handed, according to the target helicity. The left- and right-handed helix scattering matrices are given by

$$[S]_{\text{left-helix}} = \begin{bmatrix} 1 & -j \\ -j & -1 \end{bmatrix}, \text{ and } [S]_{\text{right-helix}} = \begin{bmatrix} 1 & j \\ j & -1 \end{bmatrix}, \tag{2.7}$$

and the corresponding coherency matrices are given by

$$[T]_{\text{left-helix}} = \frac{1}{2}\begin{bmatrix} 0 & 0 & 0 \\ 0 & 1 & -j \\ 0 & j & 1 \end{bmatrix}, \text{ and } [T]_{\text{right-helix}} = \frac{1}{2}\begin{bmatrix} 0 & 0 & 0 \\ 0 & 1 & j \\ 0 & -j & 1 \end{bmatrix}. \tag{2.8}$$

In Y4O, helix scattering was used to address two issues of FDD, first the overestimation of volume scattering power, and second, the reflection symmetry assumption. In FDD, entire cross-polarization power contributes to volume scattering class only. By introducing helix scattering model, overestimation of volume scattering power is reduced somewhat, as a part of cross-polarization power is taken by the helix scattering mechanism. Whereas, the second issue, i.e. reflection symmetry assumption is partially relaxed through modeling of imaginary term of T_{23} element. By adding helix scattering in the decomposition scheme, Y4O showed some improvement over FDD. However, this improvement was not good enough as the helix scattering power is much weaker than the other scattering mechanisms' power.

The next effective contribution in this subcategory was reported by Sato *et al.* [85]. Sato *et al.* [85] investigated that the model-based decomposition methods still not able to efficiently discriminate between vegetation and oriented dihedral structures. This problem is due to wrongly assigning the urban cross-polarization power to vegetation category. To overcome this problem, authors in [85] proposed a new scattering matrix known as

extended volume scattering model. This model accounts for the cross-scattering power (HV) induced by the oriented dihedral structures. The coherency matrix of the extended volume scattering model can be generated with the help of rotated dihedral scattering matrix through cosine distributed averaging with its peak at zero degree. The extended volume scattering model can be represented as

$$[T]_{\mathrm{vd}} = \frac{1}{15}\begin{bmatrix} 0 & 0 & 0 \\ 0 & 7 & 0 \\ 0 & 0 & 8 \end{bmatrix}. \tag{2.9}$$

The extended volume scattering model is used in conjunction with volume scattering model on the basis of the sign of a branching condition given by

$$\mathrm{C} : T_{11} - T_{22} + \frac{1}{2}P_{\mathrm{c}}. \tag{2.10}$$

This branching condition is used to decide the dominant scattering mechanism according to which the volume scattering (HV component) is assigned either to vegetation or to oriented dihedral structures as

$\mathrm{C} > 0$: Dominant surface scattering $\rightarrow$ Volume scattering by vegetation.

$\mathrm{C} \leq 0$: Dominant double-bounce scattering $\rightarrow$ Volume scattering by oriented dihedral.

Sato *et al.* [85] model-based decomposition method showed a great improvement over conventional as well as other parallel advancements. However, the method seems to be partially inappropriate according to the concept of distributed targets. The radar backscatter is the time averaged samples of scattering from a set of different single targets. This set of single targets is called the distributed radar target. Model-based decomposition methods always search for dominant average scattering mechanism in the case of distributed targets. However, for each pixel, Sato *et al.* forcefully made one of the scattering powers (between P_{v} and P_{vd}) zero based on the sign of branching condition 'C'. It could be possible that a single pixel may contain cross-polarization scattering from both oriented dihedral and vegetation which completely depends on the resolution and the scattering area type. In that case, making one component's power zero is inadvisable. Therefore, a provision should be there to find out each scattering mechanisms power used in the decomposition scheme for every pixel.

In 2014, another rotated dihedral cross-scattering model was proposed by Hong and Wdowinski [86]. The idea for generating this dihedral cross-scattering model was same as of [85]. However, for averaging purpose, uniform distribution function is utilized. Hong and Wdowinskis' [86] cross-scattering model can be described as

$$[T]_{\mathrm{rd}} = \frac{1}{2}\begin{bmatrix} 0 & 0 & 0 \\ 0 & 1 & 0 \\ 0 & 0 & 1 \end{bmatrix}. \tag{2.11}$$

In contrary to Sato *et al.* [85] decomposition method, Hong and Wdowinski used their rotated dihedral scattering model along with volume scattering matrix. However, this increased the number of unknowns in the decomposition scheme. Hence, to solve the unknowns, first cross-scattering contribution f_{rd} is calculated by assuming surface scattering zero, i.e. $f_{\mathrm{s}} = 0$. The positive values of f_{rd} are considered to be consistent with the assumption, whereas, for negative values, f_{rd} is assumed to be zero and the remaining unknowns are solved as of Y4O [74]. Like Sato *et al.* [85] model-based method, one can only compute either surface (P_{s}) or rotated dihedral (P_{rd}) scattering power for Hong and Wdowinskis' decomposition method.

The latest major contribution in dihedral scattering category is reported by Lee *et al.* [35]. In [35], incoherent dihedral scattering model was generated by rotating the conventional dihedral scattering coherency matrix about an angle χ in the plane perpendicular to the scattering plane as

$$[T(\chi)]_{\mathrm{d}} = [U(\chi)]\,[T]_{\mathrm{d}}\,[U(\chi)]^{*T}, \tag{2.12}$$

where $[T]_{\mathrm{d}}$ is the conventional dihedral scattering matrix as described in (1.30), and the unitary rotation matrix $[U(\chi)]$ is same as given in (2.2). The incoherent dihedral scattering model can be computed as

$$[T(\chi)]_{\mathrm{d}} = \begin{bmatrix} |\alpha|^2 & \alpha X_{12} & 0 \\ \alpha^* X_{12} & X_{22} & 0 \\ 0 & 0 & X_{33} \end{bmatrix}, \tag{2.13}$$

where parameters X_{12}, X_{22}, and X_{33} have the same expressions as defined in (2.4), (2.5), and (2.6), respectively. In [35], the incoherent dihedral scattering matrix is used along with X-Bragg surface scattering model to introduce a generalized model-based decomposition scheme.

2.1.3 Volume Scattering Model

There are various volume scattering models that have been reported in literature to tackle the overestimation problem. Likewise dihedral scattering category, Yamaguchi *et al.* [74]

Table 2.2: Dihedral scattering models

Paper	Salient Points	Year
Yamaguchi *et al.* [74]	Proposed Y4O by introducing helix scattering in FDD as the fourth component.	2005
Sato *et al.* [85]	Proposed extended volume scattering model to account cross-polarization power from urban areas. Rotated dihedral scattering matrix was used with cosine distribution function.	2012
Hong *et al.* [86]	Rotated dihedral scattering matrix was used with uniform distribution function to propose a cross-scattering model.	2014
Lee *et al.* [35]	Proposed incoherent double-bounce scattering model by rotating conventional dihedral scattering coherency matrix about an angle χ.	2014

first modified the Freeman and Durdens' volume scattering model [33] in their Y4O. FDD's volume scattering model was based on the uniform probability distribution assumption. However, considering vertical and horizontal structures of trees, Yamaguchi *et al.* [74] incorporated sine and cosine distribution functions, to compute average volume scattering matrix. Taking vertical dipole scattering matrix with $p(\theta) = \frac{1}{2}\sin\theta$, the average volume scattering matrix can be derived from (1.34) as

$$[T]_{\mathrm{v}}^{\sin} = \frac{1}{30}\begin{bmatrix} 15 & 5 & 0 \\ 5 & 7 & 0 \\ 0 & 0 & 8 \end{bmatrix}. \tag{2.14}$$

For cosine distribution $\left(p(\theta) = \frac{1}{2}\cos\theta\right)$, the average volume scattering matrix can be computed as

$$[T]_{\mathrm{v}}^{\cos} = \frac{1}{30}\begin{bmatrix} 15 & -5 & 0 \\ -5 & 7 & 0 \\ 0 & 0 & 8 \end{bmatrix}. \tag{2.15}$$

The aforementioned volume scattering models are applied in Y4O decomposition scheme according to co-polar scattering powers ratio as

$$r = 10\log\frac{|S_{\mathrm{VV}}|^2}{|S_{\mathrm{HH}}|^2} = \begin{cases} [T]_{\mathrm{v}} = [T]_{\mathrm{v}}^{\sin} & r < -2 \text{ db} \\ [T]_{\mathrm{v}} = [T]_{\mathrm{v}}^{\text{uniform}} & -2 \text{ db} \leq r \leq 2 \text{ db} \\ [T]_{\mathrm{v}} = [T]_{\mathrm{v}}^{\cos} & r > 2 \text{ db} \end{cases} \tag{2.16}$$

The next significant contribution in volume scattering category was reported by Freeman in two-component scattering model. [87]. In this, two simple scattering mechanisms

of forest are fitted to the polarimetric SAR observations [87]. These mechanisms are canopy scatter from a reciprocal medium with azimuth symmetry and a ground scatter that can be viewed as the double-bounce scattering or Bragg scatter from a moderately rough surface. This decomposition scheme was mainly developed for observation of forests. The Freeman's new volume scattering model can be given as

$$[T]_{\mathrm{v}}^{\mathrm{Freeman}} = \frac{1}{3-\rho}\begin{bmatrix} 1+\rho & 0 & 0 \\ 0 & 1-\rho & 0 \\ 0 & 0 & 1-\rho \end{bmatrix}, \tag{2.17}$$

where ρ is the shape parameter which provides more flexibility in volume scattering model.

In 2010, An *et al.* [88] adopted a different approach to model the volume scattering phenomenon. The idea was to consider only the total randomness which is a prime factor of volume scattering mechanism. It is assumed that the volume scattering is generated by the infinite number of randomly oriented dipoles. This random arrangement of dipoles shows high randomness. Therefore, any matrix representing volume scattering mechanism should have maximum entropy, i.e. one. Considering these facts, An *et al.* [88] used identity matrix to represent the volume scattering phenomenon. Identity matrix has maximum entropy ($H = 1$) which describes the completely random phenomenon where the power generated is independent of incoming polarization [26], therefore fulfils the requirement to represent volume scattering mechanism. An *et al.* [88] volume scattering matrix is given by

$$[T]_{\mathrm{v}}^{\mathrm{An}} = \frac{1}{3}\begin{bmatrix} 1 & 0 & 0 \\ 0 & 1 & 0 \\ 0 & 0 & 1 \end{bmatrix}. \tag{2.18}$$

Following the advancements, an adaptive volume scattering model was proposed by Antropov *et al.* [89]. Their volume scattering model, commonly known as generalized volume scattering model (GVSM), is given by

$$[T]_{\mathrm{v}}^{\mathrm{Antropov}} = \frac{1}{\frac{3(1+\gamma)}{2}-\rho\sqrt{\gamma}}\begin{bmatrix} \frac{1+\gamma}{2}+\rho\sqrt{\gamma} & \frac{\gamma-1}{2} & 0 \\ \frac{\gamma-1}{2} & \frac{1+\gamma}{2}-\rho\sqrt{\gamma} & 0 \\ 0 & 0 & \frac{1+\gamma}{2}-\rho\sqrt{\gamma} \end{bmatrix}, \tag{2.19}$$

where γ and ρ are defined by

$$\gamma = \frac{|S_{HH}|^2}{|S_{VV}|^2}, \text{ and } \rho = \frac{\left(S_{HH}S_{VV}^*\right)}{\sqrt{\left(S_{HH}S_{HH}^*\right)\left(S_{VV}S_{VV}^*\right)}}. \tag{2.20}$$

These two ratios γ and ρ provide adaptability to GVSM and make it suitable for the study of forests as well as several other types of anisotropic media. By varying the values of γ and ρ, GVSM can be transformed into any of the aforementioned discussed volume scattering models.

In another article, an adaptability is provide to Freeman and Durdens' uniformly distributed volume scattering model by Chen *et al.* [90]. Chen *et al.* [90] volume scattering model utilized entropy (H) information to determine volume scattering contribution of each pixel. This model can be presented as

$$[T]_v^{Chen} = \frac{1}{4-H}\begin{bmatrix} 2-H & 0 & 0 \\ 0 & 1 & 0 \\ 0 & 0 & 1 \end{bmatrix}. \tag{2.21}$$

For maximum entropy ($H = 1$), this model becomes An *et al.* [88] volume scattering model. While for $H = 0$, the model replicates Freeman and Durdens' [33] uniformly distributed volume scattering model. Another distribution function is utilized by Wang *et al.* [91] to present a new volume scattering model using dipoles with two dominant orientations. For that, the probability distribution function was taken as

$$p(\theta) = \begin{cases} \sin 2\theta, & [0, \frac{\pi}{2}) \\ 0, & [\frac{\pi}{2}, 2\pi) \end{cases} \tag{2.22}$$

By placing this probability distribution function in 1.34, the averaged volume scattering model can be computed as

$$[T]_v^{Wang} = \frac{1}{6}\begin{bmatrix} 3 & 0 & 0 \\ 0 & 1 & 0 \\ 0 & 0 & 2 \end{bmatrix}. \tag{2.23}$$

Wang *et al.* [91] showed a small improvement over $[T]_v^{An}$ [88] by decreasing negative power pixel count.

Apart from aforementioned literature, some notable volume scattering models were presented in [92]- [94]. However, the main concern of these volume scattering models was the characterization of vegetation, such as forest structure, canopy layer characteristics etc. Moreover, these volume scattering models [92]- [93] are more complex as compared to previously discussed volume scattering models [74], [87]- [91].

Table 2.3: Volume scattering models

Paper	Salient Points	Year
Yamaguchi *et al.* [74]	Oriented dipole scattering matrix was utilized with sine and cosine distribution functions.	2005
Freeman [87]	Provided more flexibility in original FDD's volume scattering model by introducing shape parameter.	2007
An *et al.* [88]	Identity matrix was used to represent volume scattering phenomenon.	2010
Antropov *et al.* [89]	Introduced a generalized volume scattering model. Flexibility was provided by the ratio of co-polarized power.	2011
Chen *et al.* [90]	Entropy (H) information is used to determine the volume scattering contribution of a pixel.	2014
Wang *et al.* [91]	Dipoles with two dominant orientations are utilized to generate volume scattering model.	2018

2.2 Unitary Rotations of Coherency Matrix

It is a well known fact that the backscattering coefficient is highly dependent on target structure and its relative orientation with respect to the radar illumination. The process of reducing the orientation dependency is known as deorientation [17], [79], [95]- [101]. The concept of deorientation was first introduced by Huynen [17]. Further, this theory has been emphasized by Lee *et al.* [78] with a new nomenclature known as orientation angle compensation (OAC). OAC involves the rotation of coherency matrix through a unitary rotation matrix as

$$[T(\vartheta_1)] = [U(\vartheta_1)][T][U(\vartheta_1)]^{*\mathrm{T}}, \tag{2.24}$$

where $[T(\vartheta_1)]$ is the rotated coherency matrix, $[T]$ is the measured coherency matrix, and $[U(\vartheta_1)]$ is the unitary rotation matrix given by

$$[U(\vartheta_1)] = \begin{bmatrix} 1 & 0 & 0 \\ 0 & \cos 2\vartheta_1 & \sin 2\vartheta_1 \\ 0 & -\sin 2\vartheta_1 & \cos 2\vartheta_1 \end{bmatrix}. \tag{2.25}$$

Here ϑ_1 is known as orientation angle. Orientation angle was first derived from the circular polarization based covariance matrix [78]. Later, it was seen that the angle obtained by the minimization of the cross-polarization term of rotated coherency matrix $[T(\vartheta_1)]$ was same as that of orientation angle [102]- [106], which can be given as

$$\vartheta_1 = \frac{1}{4}\tan^{-1}\left(\frac{2\Re(T_{23})}{T_{22}-T_{33}}\right). \tag{2.26}$$

The improvement in the performance of the model-based decomposition method with orientation angle compensation was first observed by An *et al.* [88] in 2010. After that, the effect of orientation angle compensation on coherency matrix elements was further analyzed by Lee *et al.* [102]. In [102], authors demonstrated that after OAC, T_{22} element of coherency matrix which represents the double-bounce scattering channel always increases, while the cross-polarization power T_{33} always decreases by the same amount. The most affected term is $\mathrm{Re}(T_{23})$ which becomes zero after OAC. $\mathrm{Re}(T_{23})$ represents the correlation between double-bounce and volume scattering mechanisms. This term is sensitive to slope and orientation of the scatterer. Terrain slope and orientation of the scatterer induce large values to this term. However, the $\mathrm{Im}(T_{23})$ term is invariant to slope and orientation. Meanwhile to Lee *et al.* [102] investigations, Yamaguchi *et al.* [106] proposed four-component decomposition with rotation of coherency matrix (Y4R). This method was the implementation of Y4O on orientation angle compensated coherency matrix. Parallely, the similar work was presented in [107].

Uniform matrix rotation theory was further explored by Singh *et al.* [108] in general four-component decomposition (G4U) method. In [108], double-unitary rotation of coherency matrix was proposed. The first rotation of coherency matrix was achieved through OAC, while for the second rotation, a complex rotation matrix given in (2.27) from special unitary SU(3) group [1]- [2] was utilized.

$$[U(\vartheta_2)] = \begin{bmatrix} 1 & 0 & 0 \\ 0 & \cos 2\vartheta_2 & j\sin 2\vartheta_2 \\ 0 & j\sin 2\vartheta_2 & \cos 2\vartheta_2 \end{bmatrix}. \tag{2.27}$$

Coherency matrix transformation through the aforementioned rotation matrix is achieved after OAC as

$$[T(\vartheta_2)] = [U(\vartheta_2)][T(\vartheta_1)][U(\vartheta_2)]^{*\mathrm{T}}. \tag{2.28}$$

The rotation angle ϑ_2 can be derived by minimizing the cross-polarization term of $[T(\vartheta_2)]$, as

$$\vartheta_2 = \frac{1}{4}\tan^{-1}\left(\frac{2\Im\left(T_{23}(\vartheta_1)\right)}{T_{22}(\vartheta_1) - T_{33}(\vartheta_1)}\right). \tag{2.29}$$

This second rotation accounts for the imaginary part of T_{23}, i.e. $\Im(T_{23})$, after which the T_{23} element completely becomes zero, and the coherency matrix is left with 7 independent parameters. To utilize these remaining seven parameters of coherency matrix, Singh *et al.* [108] proposed generalized scattering models. Generalized scattering models are generated by transforming the conventional scattering models through the aforementioned complex rotation matrix.

The applicability of G4U was further enhanced by Bhattacharya *et al.* [109] in adaptive general four-component decomposition (AG4U). In AG4U [109], one of the two complex rotation matrices from SU(3) group was used to rotate the OA compensated coherency matrix. The first complex rotation matrix was same as given in (2.27), however, the second complex rotation matrix is given by

$$[U(\varphi_2)] = \begin{bmatrix} \cos2\varphi_2 & 0 & j\sin2\varphi_2 \\ 0 & 1 & 0 \\ j\sin2\varphi_2 & 0 & \cos2\varphi_2 \end{bmatrix}. \tag{2.30}$$

The rotation of the OA compensated coherency matrix through $[U(\varphi_2)]$ can be accomplished as

$$[T(\varphi_2)] = [U(\varphi_2)][T(\vartheta_1)][U(\varphi_2)]^{*\mathrm{T}}. \tag{2.31}$$

The rotation angle φ_2 for this transformation can be given as

$$\varphi_2 = \frac{1}{4}\tan^{-1}\left(\frac{2\Im\left(T_{13}(\vartheta_1)\right)}{T_{11}(\vartheta_1) - T_{33}(\vartheta_1)}\right). \tag{2.32}$$

The selection between complex rotation matrices (2.27) and (2.30) for second unitary rotation of coherency matrix was based on the effective degree of polarization.

Another application of unitary rotation was reported by Chen *et al.* [110]. Chen *et al.* [110] proposed a general model-based decomposition method with generalized single- and double-bounce scattering models. These generalized scattering models are generated by transforming the conventional single- and double-bounce scattering models through the following two unitary rotation matrices, given as

$$[U(\vartheta_{\mathrm{odd}})] = \begin{bmatrix} 1 & 0 & 0 \\ 0 & \cos2\vartheta_{\mathrm{odd}} & \sin2\vartheta_{\mathrm{odd}} \\ 0 & -\sin2\vartheta_{\mathrm{odd}} & \cos2\vartheta_{\mathrm{odd}} \end{bmatrix}, \tag{2.33}$$

$$[U(\vartheta_{\mathrm{dbl}})] = \begin{bmatrix} 1 & 0 & 0 \\ 0 & \cos2\vartheta_{\mathrm{dbl}} & \sin2\vartheta_{\mathrm{dbl}} \\ 0 & -\sin2\vartheta_{\mathrm{dbl}} & \cos2\vartheta_{\mathrm{dbl}} \end{bmatrix}. \tag{2.34}$$

The matrix given in (2.33) was used to generate generalized single-bounce scattering model while matrix given in (2.34) was utilized to generate the generalized double-bounce scattering model. However, like incoherent scattering models in [35], Chen *et al.* [110] did not average their generalized scattering models through any distribution function. The second difference is Chen *et al.* [110] generalized scattering models do not follow the reflection symmetry assumption. In [110], (2.33) and (2.34) are treated as unknowns along

with other model-coefficients whose values are determined by the residual minimization criterion.

Table 2.4: Unitary rotations of coherency matrix

Paper	Salient Points	Year
An *et al.* [88]	Deorientation was first introduced in model-based decomposition technique.	2010
	Implemented Y4O with deorientation.	2011
Lee and Ainsworth [102]	Analyzed OAC effect on coherency matrix elements.	2007
Yamaguchi *et al.* [106]	Proposed Y4R by introducing OAC in original Y4O.	2011
Singh *et al.* [108]	Proposed double unitary rotation of coherency matrix. Transformed conventional scattering models with phase rotated unitary matrix.	2013
Chen [110]	Unitary rotation matrix with different rotation angles are used to transform conventional surface and dihedral scattering models.	2014
Bhattacharya *et al.* [109]	Proposed adaptive unitary rotation of coherency matrix based on effective degree of polarization.	2015

2.3 Elimination of Negative Power Problem

As mentioned in Section 1.4, overestimation of volume scattering power is the main reason for getting negative power pixels in model-base decomposition methods. The negative power problem was first confronted by Yajima *et al.* [111] in their modified four-component scattering power decomposition. The method deals with the negative power problem by inspection of the decomposed powers at every pixel. The decomposed scattering powers having negative values are made zero.

The next advancement in this category was reported by Cloude in 2010 [2]. Cloude proposed a hybrid three-component decomposition method [2]. In this hybrid method, the volume scattering power was first derived from the Freeman and Durdens' volume scattering model, while the eigenvalue and eigenvectors' information are utilized to compute the surface and dihedral scattering powers. Cloude's hybrid approach provides a solution for negative power problem by keeping only the non-negative eigenvalue spectrum of $[T]_{\text{sd}}$. Later on, Singh *et al.* [112] incorporated OAC in Cloude's hybrid decomposition method to compensate the effects of polarization orientation angle shifts. In addition to OAC, Singh *et al.* [112] also introduced extended volume scattering model [85] to improve the performance of Cloude's hybrid method. Subsequently, Cloude's hybrid scattering mod-

els were employed by Zhang *et al.* [113] to present a modified hybrid Freeman/eigenvalue decomposition. In modified hybrid Freeman decomposition, eigenvalues based parameters, anisotropy [1] and entropy [27] are used to decide whether the cross-polarization is induced from urban areas or vegetation.

The negative power problem of model-based decomposition methods was further discussed by Van Zyl *et al.* [76]. To avoid the negative scattering powers and eigenvalues, authors in [76] put a constrained on the contributions of different scattering components of FDD method. They added a remainder term in the FDD that contains the values of measured coherency matrix which are not consistent with the scattering models. Van Zyl *et al.* [76] non-negative eigenvalue decomposition (NNED) technique can be expressed as

$$[T] = a\,[T]_{\text{model}} + [T]_{\text{remainder}}\,. \tag{2.35}$$

where $[T]_{\text{model}}$ comprised of physical scattering models. The largest value of the parameter 'a' can be determined by ensuring that all the eigenvalues of remainder matrix $[T]_{\text{remainder}}$ must be non-negative. With this approach, volume scattering contribution is determined first. Remaining single- and double-bounce contributions are determined by keeping the remainder matrix positive semidefinite. The NNED approach was further extended by Liu *et al.* [114] for non-negative eigenvalues of four-component scattering power decomposition. The non-negative eigenvalues are the results of overestimation of some of the scattering powers. Taking this observation into account, Liu *et al.* [114] used a shrinkage coefficient to suppress all the possible overestimation of scattering powers, and the case that provides minimum remainder power was selected to resolve the issue of non-negative eigenvalue constraint problem.

The most recent noteworthy advancement to prevent negative scattering powers in model-based decomposition scheme was reported by Cui *et al.* in [115]. Cui *et al.* [115] presented a complete three-component model-based decomposition method (C3MD). The method was proposed to resolve two issues of model-based methods, i.e. the complete utilization of fully polarimetric coherency matrix and negative power problem. To utilize all the elements of coherency matrix, incoherent eigenvector-based scattering models were employed. In Cui *et al.* [115] decomposition method, the volume scattering power was first determined as the smallest eigenvalue of the coherency matrix. Further, to solve the remaining contributions of surface and dihedral scattering components, two approaches, eigen-decomposition and model fitting were used. Later on, improvements over C3MD were presented in [116]- [117]. Deorientation was applied in [116] to analyze the co-polarized scattering mechanisms after finding the volume scattering power in C3MD. While in [117], different unitary transformations are applied to eigenvectors of the remaining coherency matrix. With this, the remaining coherency matrix is made more

consistent with the conventional surface and dihedral scattering models.

Table 2.5: Analysis of negative power problem

Paper	Salient Points	Year
Yajima *et al.* [111]	By inspecting each pixel, the decomposed scattering powers having negative values are made zero.	2008
Cloude [2]	Proposed hybrid scattering models to deal with negative power problem.	2010
Van Zyl [76]	Proposed non-negative eigenvalue decomposition (NNED) by putting constrained on the contributions of different scattering components of FDD method.	2011
Singh *et al.* [112]	Incorporated OAC in Cloude's hybrid decomposition method to compensate the effects of orientation shifts.	2013
Zhang *et al.* [113]	Anisotropy and entropy informations are incorporated in Cloude's hybrid decomposition method to differenetiate between cross-polarization powers from vegetation and man-made structures.	2015
Liu *et al.* [114]	Extended NNED to four-component deccomposition.	2014
Cui *et al.* [115]	Volume scattering power was first determined as the smallest eigenvalue of the coherency matrix. To solve the remaining contributions of surface and dihedral scattering components, two approaches, eigen-decomposition and model fitting were used.	2014

2.3.1 Scattering Similarity

Another domain that deals with negative scattering power problem is based on the scattering similarity. The similarity parameter identifies the closest matrix to a given matrix from a set of different matrices. Scattering similarity in PolSAR context was first used by Yang *et al.* [118] in 2001. In [118], authors proposed a similarity parameter to obtain the degree of similarity between the scattering matrix of a scatterer and the canonical scattering mechanisms. The scattering mechanism with highest degree of similarity was assigned as the class of that scatterer. The similarity approach was extended to next level in [119]-[120] where similarity parameter between coherency matrix of a scatterer and canonical scattering mechanisms were measured. The similarity parameter can be computed as

$$\text{Similarity Parameter} = \frac{\text{Tr}\left([T]\,[T]_{\text{c}}^{\text{H}}\right)}{\text{Tr}\left([T]\right)\text{Tr}\left([T]_{\text{c}}\right)}, \tag{2.36}$$

where Tr denotes the trace of a matrix, $[T]$ is the measured coherency matrix, $[T]_{\text{c}}$ represents the coherency matrix of canonical scattering mechanism, and symbol 'H' stands for

Hermitian transpose. The canonical coherency matrices of surface, and dihedral scattering mechanisms are given by

$$[T]_{\text{surface}} = \begin{bmatrix} 1 & 0 & 0 \\ 0 & 0 & 0 \\ 0 & 0 & 0 \end{bmatrix}, \text{ and } [T]_{\text{dihedral}} = \begin{bmatrix} 0 & 0 & 0 \\ 0 & 1 & 0 \\ 0 & 0 & 0 \end{bmatrix}. \tag{2.37}$$

The scattering similarity approach was further extended to $H/\overline{\alpha}$ decomposition along with incorporation of different volume scattering models in [121]- [123]. The scattering similarity based target decomposition has two major advantages over model-based decomposition methods, which are

1. Similarity parameter is independent of the target orientation.

2. As can be seen from (2.36), the similarity parameter always results in positive value, therefore, always guarantees positive decomposition result.

Since scattering similarity parameter is derived independently for each of the scattering mechanisms, the decomposition schemes based on it do not require any branching condition. However, this circumstance could lead to a problem in discriminating areas of different target classes with same scattering behavior. For example, let a complex urban area whose streets are not aligned with the radar illumination. This situation will lead to high cross-polarization power generation. If PolSAR data of this area is decomposed by FDD, then all the cross-polarization power is assigned to volume scattering class. However, in case of Y4O, the volume scattering contribution decreases since it is obtained after subtracting the helix scattering contribution from cross-polarization (T_{33}) term. On the other hand, the similarity parameter based techniques [118]- [123] compute the volume scattering similarity same for both aforementioned cases as it will be derived independently. Therefore, classification based on scattering similarity will always classify that area under vegetation by reason of high volume scattering similarity irrespective of the number of scattering classes used. This problem of scattering similarity based techniques was somewhat resolved by Ratha *et al.* [124] through normalizing and then assigning weights to similarity parameter of each scattering mechanisms. Ratha *et al.* [124] proposed the scattering similarity measure based on Geodesic distance (GD). Instead of using coherency matrices of canonical scattering mechanisms, Ratha *et al.* [124] exploited Kennaugh matrix to compute the *GD* between target and elementary scattering mechanisms. The *GD* between two Kennaugh matrices can be obtained as [125]

$$GD\left([K]_1,[K]_2\right)=\frac{2}{\pi}\cos^{-1}\left(\frac{\mathrm{Tr}\left([K]_1^T[K]_2\right)}{\sqrt{\mathrm{Tr}\left([K]_1^T[K]_1\right)}\sqrt{\mathrm{Tr}\left([K]_2^T[K]_2\right)}}\right). \tag{2.38}$$

where $[K]_{\mathrm{i}}$ represents the Kennaugh matrix [125]. The similarity measure based on *GD* can be derived as

$$f_{\mathrm{i}}=1-GD\left([K],[K]_{\mathrm{i}}\right). \tag{2.39}$$

Normalization of similarity measure was achieved as

$$\gamma_{\mathrm{i}}=\frac{f_{\mathrm{i}}}{\sum_{\mathrm{i}}f_{\mathrm{i}}}. \tag{2.40}$$

Afterwards, normalized similarity measure of each scattering mechanisms were multiplied by a weight equal to *span* to make the similarity measures comparable to the decomposed scattering powers of model-based methods.

Table 2.6: Similarity parameter analysis

Paper	Salient Points	Year
Yang *et al.* [118]	Proposed similarity parameter to obtain the degree of similarity between the scattering matrices of target and canonical scattering mechanisms.	2001
Chen *et al.* [119]- [121]	Similarity parameter approach was extended to coherency matrix of canonical scattering mechanisms.	2010
	Utilized eigenvector-based parameters to compute scattering similarity.	2013
Li *et al.* [122]- [123]	Proposed random similarity between two mixed scatterers by utilizing different volume scattering matrices.	2015
	Eigenvector-based parameters utilized along with different volume scattering models to find the scattering similarity between two mixed targets.	2017
Ratha *et al.* [124]	Obtained scattering similarity by using Geodesic distance between measured coherency matrix and canonical scattering mechanisms.	2017

Chapter 3

Extended Four-Component Decomposition by Using Modified Cross-Scattering Matrix

3.1 Introduction

This chapter deals with classification of oriented urban areas. Urban area classification is essential for monitoring growth of megacities. With ever-increasing urban population density, megacities have been rapidly expanding by encroaching the forest, agricultural lands and wetlands. Hence, timely monitoring of urban expansion is utmost required for proper urban planning, infrastructure development and climate control.

The radar backscattering is highly dependent on the target structure and its relative orientation with respect to radar illumination. In urban areas, oriented man-made structures generate a significant amount of cross-polarization power. This cross-polarization generation from urban areas results in the scattering mechanism ambiguity. As cross-polarization is mainly accounted by the volume scattering contribution in the conventional model-based decomposition techniques, oriented urban structures are wrongly classified into volume scattering category. An efficient way to overcome this problem is to model the urban cross-polarization power in an appropriate way. Several literature have been reported, where authors modeled the urban cross-polarization power by rotated dihedral scattering mechanism with different distribution functions [85]- [86]. However, the above referred models do not utilize any extra unused element of the coherency matrix while adding one more scattering mechanism as can be seen from (2.9) and (2.11). This results in further increase of the number of unknown model coefficients and constrained their decomposition schemes to make additional assumptions to solve the unknowns. The second issue is that instead of finding out the contribution of each scattering mechanism,

these methods completely neglect the contributions of some scattering mechanisms on the basis of branching conditions. This process partially defies the principle of model-based decomposition methods, where for every pixel, the contribution of each scattering mechanism is computed. The third issue with these models is their constant contributions for each urban pixels. It could be possible that the different urban structures may have different orientations. Therefore, to overcome these problems, a new adaptive scattering model is needed to accommodate the cross-polarization power from urban areas.

The cross-polarization generation in oriented urban areas is because of polarization orientation angle (POA) shifts. In urban areas, polarization orientation shift is induced by the oriented man-made structures. The term $\Re(T_{23})$ is associated with the polarization orientation shifts. Hence by considering this term through proper modeling, the urban cross-polarization power can be characterized. To realize this, rotated dihedral scattering matrix is used to introduce a modified cross-scattering model. Proposed cross-scattering model is averaged by the cosine distribution with its peak at orientation angle. This averaging results in the modeling of $\Re(T_{23})$ which allows us to independently calculate the power of modified cross-scattering mechanism. This empowers us to get rid of additional assumptions to solve the unknown model coefficients. Also, by utilizing orientation angle information of each pixel, adaptivity is incorporated in the proposed cross-scattering model.

3.2 Generation of the Modified Cross-Scattering Matrix

A modified cross-scattering matrix is introduced to account for the cross-polarization generation from the oriented urban structures. The modified cross-scattering matrix is generated from the scattering matrix of a rotated dihedral characterized by the orientation angle of the buildings. Scattering matrix of a dihedral is given by [1]

$$[S]_{\text{dihedral}} = \begin{bmatrix} 1 & 0 \\ 0 & -1 \end{bmatrix}. \tag{3.1}$$

The coherency matrix of a dihedral rotated by an angle θ can be computed as

$$[T(\theta)]_{\text{dihedral}} = \begin{bmatrix} 0 & 0 & 0 \\ 0 & \cos^2 2\theta & -\sin 4\theta/2 \\ 0 & -\sin 4\theta/2 & \sin^2 2\theta \end{bmatrix}. \tag{3.2}$$

Since different buildings may have different orientation angles with respect to the radar illumination, the orientation angles of these buildings should be considered in order to generate the modified cross-scattering matrix. Therefore, cosine distribution function

with its peak at dominant POA is used to obtain the averaged modified cross-scattering matrix.

$$p(\theta) = \frac{1}{2}\cos(\theta - \vartheta_1), \quad -\frac{\pi}{2} + \vartheta_1 < \theta < \frac{\pi}{2} + \vartheta_1 \tag{3.3}$$

where ϑ_1 is the polarization orientation angle given by [102]

$$\vartheta_1 = \frac{1}{4}\tan^{-1}\left(\frac{2\Re(T_{23})}{T_{22} - T_{33}}\right). \tag{3.4}$$

The averaged modified cross-scattering matrix can be derived as

$$[T]_{\times-\text{pol}} = \int_{-\frac{\pi}{2}+\vartheta_1}^{\frac{\pi}{2}+\vartheta_1} [T(\theta)]_{\text{dihedral}}\ p(\theta)\, d\theta. \tag{3.5}$$

From (3.3) and (3.5), the averaged modified cross-scattering coherency matrix $[T]_{\times-\text{pol}}$ can be determined as [126]

$$[T]_{\times-\text{pol}} = \begin{bmatrix} 0 & 0 & 0 \\ 0 & \frac{1}{2} - \frac{\cos 4\vartheta_1}{30} & \frac{\sin 4\vartheta_1}{30} \\ 0 & \frac{\sin 4\vartheta_1}{30} & \frac{1}{2} + \frac{\cos 4\vartheta_1}{30} \end{bmatrix} = \begin{bmatrix} 0 & 0 & 0 \\ 0 & t_{22} & t_{23} \\ 0 & t_{32} & t_{33} \end{bmatrix}. \tag{3.6}$$

3.3 Decomposition Methodology

An extended four-component decomposition (E4D) method is presented here by utilizing the modified cross-scattering matrix. The proposed modified cross-scattering matrix is added to the four basic scattering models of Y4O [74] as follows.

$$[T] = f_s[T]_s + f_d[T]_d + f_v[T]_v + f_c[T]_c + f_{\times-\text{pol}}[T]_{\times-\text{pol}}, \tag{3.7}$$

where $[T]$ is the measured coherency matrix, f_s, f_d, f_v, f_c, and $f_{\times-\text{pol}}$ are the unknown model coefficients to be determined, and $[T]_s$, $[T]_d$, $[T]_v$, and $[T]_c$ are the coherency matrices for single-bounce, double-bounce, volume, and helix scattering mechanisms, as described in (1.27), (1.30), (1.35), and (2.8). Comparing each model coefficients with the coherency matrix elements, the following equations are obtained.

$$T_{11} = f_s + f_d|\alpha|^2 + \frac{f_v}{2} \tag{3.8a}$$

$$T_{22} = f_s|\beta|^2 + f_d + \frac{f_v}{4} + \frac{f_c}{2} + t_{22}f_{\times-\text{pol}} \tag{3.8b}$$

$$T_{33} = \frac{f_v}{4} + \frac{f_c}{2} + t_{33}f_{\times-\text{pol}} \tag{3.8c}$$

$$T_{12} = f_s\beta^* + f_d\alpha \tag{3.8d}$$

$$T_{23} = t_{23}f_{\times-\text{pol}} \pm j\frac{f_c}{2}. \tag{3.8e}$$

As can be seen from (3.6), t_{23} is always coming out to be real for all values of ϑ_1. Therefore, the modified cross-scattering contribution $f_{\times-\text{pol}}$ can be calculated from (3.8e) as

$$f_{\times-\text{pol}} = \frac{\Re(T_{23})}{t_{23}}. \tag{3.9}$$

Afterwards, the helix scattering model coefficient (f_c) can be calculated by comparing the imaginary part of both sides of (3.8e) as

$$f_c = 2\left|\Im(T_{23})\right|. \tag{3.10}$$

The volume scattering model coefficient (f_v) is determined next from (3.8c) as

$$f_v = 4\left(T_{33} - \frac{f_c}{2} - t_{33}f_{\times-\text{pol}}\right). \tag{3.11}$$

After calculating these three model coefficients, one is left with three equations and four unknowns. To solve the unknowns, a conventional assumption based on the sign of $\Re\langle S_{HH}S_{VV}^*\rangle$ is used as follows. For $\Re\langle S_{HH}S_{VV}^*\rangle > 0$, which represents the dominant surface scattering case, the unknowns can be determined as

$$f_s = T_{11} - \frac{f_v}{2},\ \beta^* = \frac{T_{12}}{f_s},\ \text{and}\ f_d = T_{22} - f_s|\beta|^2 - \frac{f_v}{4} - \frac{f_c}{2} - t_{22}f_{\times-\text{pol}}. \tag{3.12}$$

For $\Re\langle S_{HH}S_{VV}^*\rangle \leq 0$, which represents the dominant dihedral scattering case, the unknowns can be determined as

$$f_d = T_{22} - \frac{f_v}{4} - \frac{f_c}{2} - t_{22}f_{\times-\text{pol}},\ \alpha = \frac{T_{12}}{f_d},\ \text{and}\ f_s = T_{11} - f_d|\alpha|^2 - \frac{f_v}{2}. \tag{3.13}$$

In aforementioned equations, if $f_{\times-\text{pol}} < 0$, then $f_{\times-\text{pol}}$ is set to zero in order to make the proposed decomposition scheme physically realizable. The scattering powers for single-bounce (P_s), double-bounce (P_d), volume (P_v), helix (P_c), and modified cross-scattering ($P_{\times-\text{pol}}$) mechanisms can be obtained as follows.

$$\begin{aligned} &P_s = f_s\left(1+|\beta|^2\right),\ P_d = f_d\left(1+|\alpha|^2\right),\\ &P_v = f_v,\ P_c = f_c,\ \text{and}\ P_{\times-\text{pol}} = f_{\times-\text{pol}}. \end{aligned} \tag{3.14}$$

Flowchart of E4D method is shown in Figure 3.1. The term 'TP' in the flowchart corresponds to total power or *span*.

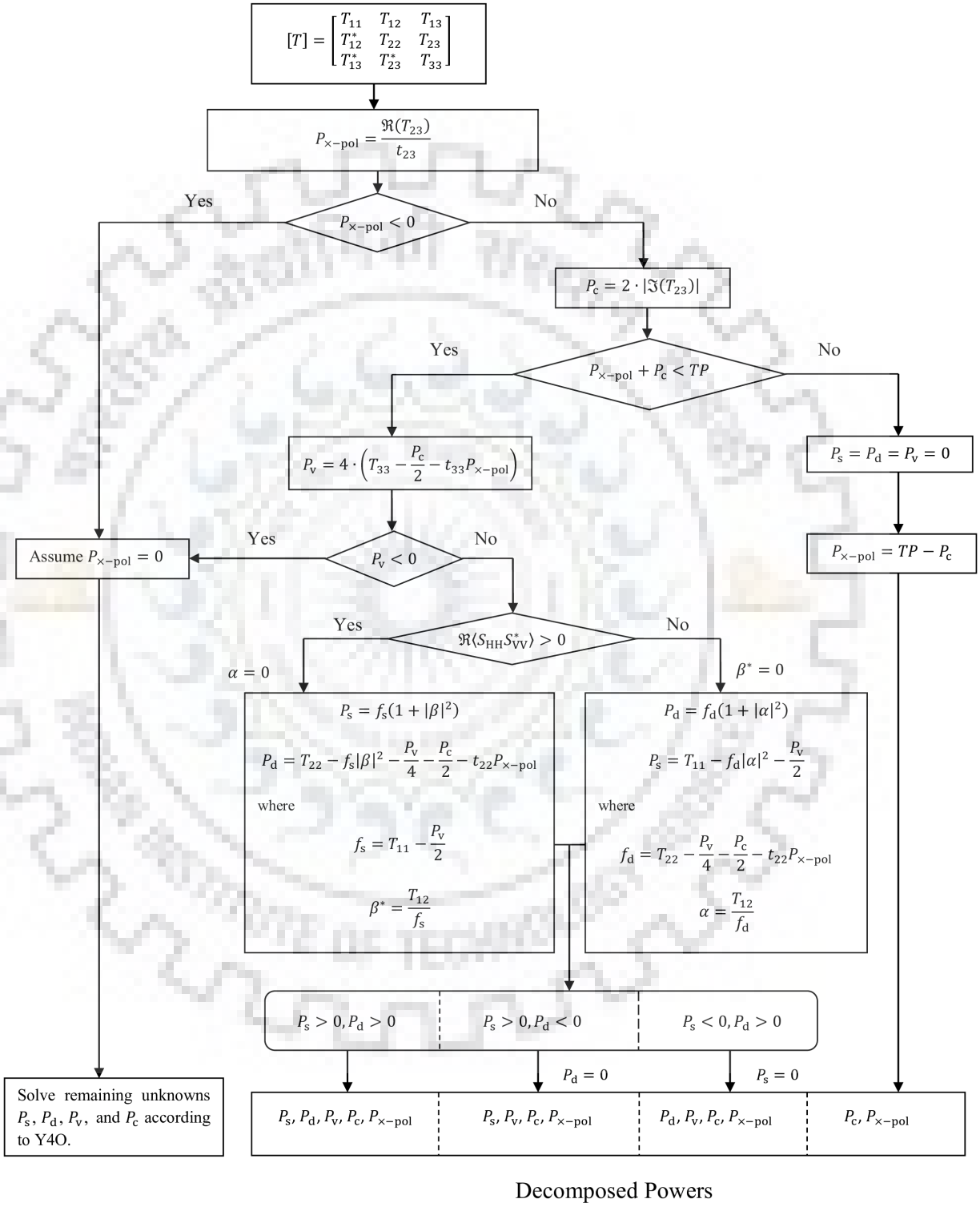

Figure 3.1: Flowchart of E4D.

3.4 Experimental Results and Discussion

E4D method is validated over two fully polarimetric datasets. The first data used for validation was acquired over the San Francisco Bay area by L-band airborne SAR, while the second data was obtained by C-band Radarsat-2 spaceborne SAR over the Mumbai region.

3.4.1 AIRSAR San Francisco Bay Data

The fully polarimetric L-band NASA/JPL AIRSAR San Francisco Bay image [127] mainly composed of ocean, urban and park areas. The Pauli RGB image of the test site is shown in Figure 3.2(a). Performance of E4D is compared with Y4O [75] and Y4R [106].

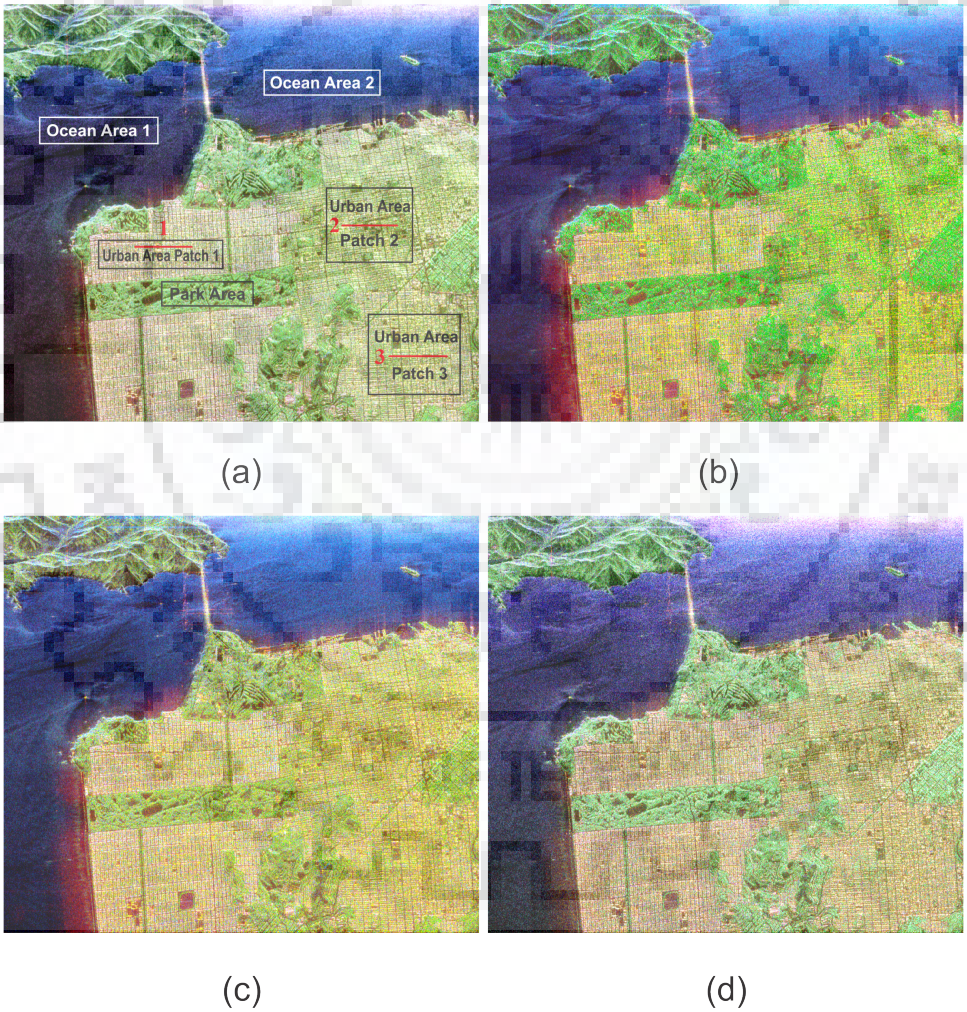

Figure 3.2: Color coded decomposed images of AIRSAR San Francisco data. (a) Pauli RGB. (b) Y4O. (c) Y4R. (d) E4D.

Figures 3.2(b) and 3.2(c) show the decomposed images of Y4O and Y4R, respectively. In both of these figures, the red color represents the urban scattering from both

double-bounce and helix scattering mechanisms. After orientation angle correction, the classification improvement can be seen in the urban Patch 2 and Patch 3 regions. Here one can notice that the OAC has significant effect on Y4O. However, even after the correction of orientation angle, the cross-polarization power generated by the oriented urban structures is not fully compensated. Figure 3.2(d) shows the classification result of the proposed decomposition method in three scattering classes, viz. single-bounce scattering (blue), urban scattering (red : from double-bounce, helix, and modified cross-scattering), and volume scattering (green). From the visual inspection of Figures 3.2(b), 3.2(c), and 3.2(d), one can see that E4D is able to classify the urban areas more efficiently as compared to Y4O and Y4R.

Table 3.1: Classification accuracies of selected land-covers in percentage (%)

Land Covers	Y4O	Y4R	E4D
Ocean Area 1	100	100	100
Ocean Area 1	100	100	100
Urban Patch 1	68.08	90.41	91.07
Urban Patch 2	3.64	52.59	90.37
Urban Patch 3	26.06	85.78	97.26
Park Area	98.64	98.24	85.33

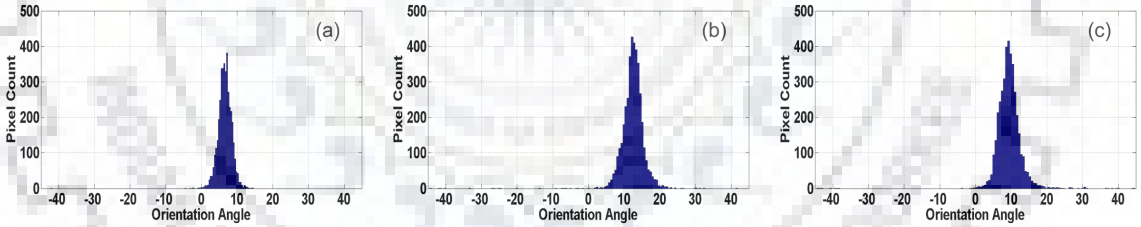

Figure 3.3: Orientation angle distribution. (a) Patch 1. (b) Patch 2. (c) Patch 3.

To demonstrate the efficacy of E4D method, the classification accuracies of selected land covers shown in Figure 3.2(a) are calculated. The classification accuracies of E4D are compared with Y4O and Y4R as shown in Table 3.1. One can see from this table that the ocean and park areas are well classified by all the aforementioned methods. However, in case of urban areas, the classification accuracy of E4D is much better in comparison to Y4O and Y4R. The three selected urban patches of San Francisco Bay image have different street orientations with respect to radar illumination as can be seen from Figure 3.3. The streets of urban Patch 1 are nearly aligned in the optimal direction to the radar illumination, while in the case of urban Patch 2 and Patch 3, the streets are somewhat oriented away from the optimal alignment. These different orientations affect the classification results of different methods.

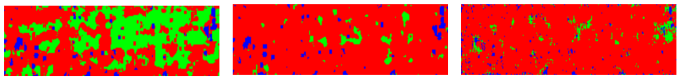

(a) (b) (c)

Figure 3.4: Classified images of urban Patch 1. (a) Y4O. (b) Y4R. (c) E4D.

In order to show the effectiveness of E4D method, further analysis has been carried out by plotting the urban scattering powers of Y4O, Y4R and E4D along three transects as shown in red color in Figure 3.2(a). The classified images of urban Patch 1 by Y4O, Y4R and E4D are shown in Figures 3.4(a), 3.4(b), and 3.4(c), respectively.

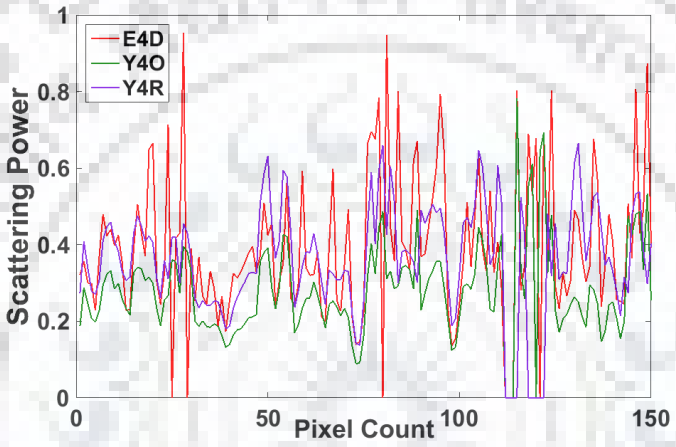

Figure 3.5: Urban scattering powers along Transect 1.

The orientation angle of urban structures in Patch 1 is in between 0 to 10° which can be seen from the Figure 3.3(a). In Figure 3.5, the urban scattering powers of Y4O, Y4R and E4D are plotted along Transect 1. From this figure, it is apparent that the Y4R and E4D have high values of urban scattering powers as compared to Y4O. The differences in urban scattering powers of aforementioned methods influence the classification results. From Table 1, one can see that E4D and Y4R classify the urban Patch 1 with 90% accuracy, whereas Y4O is able to classify this patch with 68.08% accuracy.

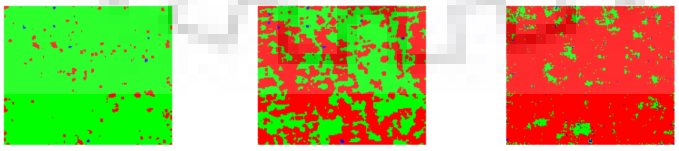

(a) (b) (c)

Figure 3.6: Classified images of urban Patch 2. (a) Y4O. (b) Y4R. (c) E4D.

The classified images for Patch 2 are shown in Figure 3.6 and the classification accuracies for different methods are given in Table 3.1. The classified images for urban Patch

2 clearly indicate that Y4O totally misclassified it. Y4R has some improvement but it is not good enough and a large urban area is misclassified under volume scattering.

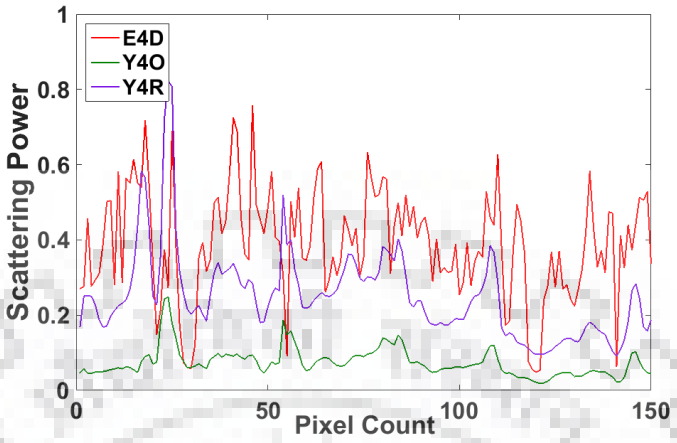

Figure 3.7: Urban scattering powers along Transect 2.

The analysis of urban Patch 2 along Transect 2 is shown in Figure 3.7. For this patch, the orientation angle range mainly lies in between 10° to 15°. From the urban scattering power plot along Transect 2 in Figure 3.7, one can notice that the urban scattering power of E4D method is quite high as compared to Y4O and Y4R. This high value of urban scattering power by E4D results into classification accuracy of 90.37% which is around 38% higher than that of Y4R.

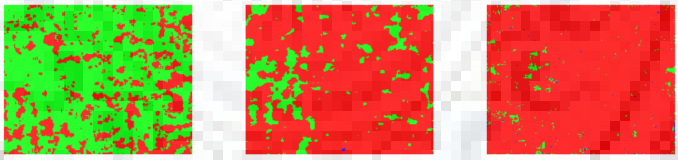

Figure 3.8: Classified images of urban Patch 3. (a) Y4O. (b) Y4R. (c) E4D.

Urban Patch 3 is classified in Figure 3.8, and the classification accuracies of Y4O, Y4R and E4D methods are given in Table 3.1. On comparing these results, one can easily see that the classification accuracy is increasing from Y4O to Y4R. However, again these results indicate that the classification accuracy of E4D is better than both the discussed methods. For Patch 3, the average value of orientation angle is centered around 10° as can be seen from Figure 3.3(c). The variation of urban scattering powers along Transect 3 are plotted in Figure 3.9. On comparing these results, one can observe that the correction of orientation angle increases the double-bounce power, so that the classification accuracy increases from Y4O to Y4R. However, a good improvement in classification accuracy is achieved by E4D. This improvement reflects the advantage of modeling of rotated dihedral structures which accounts for the cross-polarization generation in the oriented urban

areas. The capability of true characterization of this cross-polarization scattering from urban areas is the reason for the better performance of E4D.

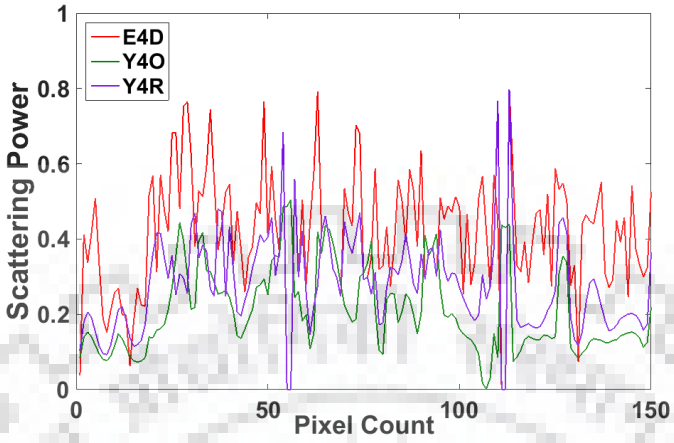

Figure 3.9: Urban scattering powers along Transect 3.

The classification accuracies of different methods for park area is given in Table 3.1. Y4O and Y4R classify the selected Golden Gate Park area more than 98% as volume scattering, whereas the proposed method classification accuracy is 85.33%. However, details of the ground truth indicates the existence of man-made structures in this region which signify double-bounce scattering mechanism. Also, this park area consists of medium density forest, so some double-bounce scattering due to the signal reflection from ground-tree trunk combinations can be expected. One can also notice lakes and clear cut areas which indicate some surface scattering mechanism as well. Therefore, the presence of the aforementioned factors justify the low value of volume scattering contribution by E4D method as compared to the rest of the two methods.

3.4.2 Radarsat-2 Mumbai Data

In order to demonstrate the robustness of the algorithm, E4D scheme is applied to second dataset obtained by fully polarimetric C-band Radarsat-2 spaceborne satellite. The dataset was acquired over Mumbai, India region by fine quad beam (FQ22).

The pauli RGB and Google Earth optical images of test site are shown in Figure 3.10. The Mumbai test site composed of sea area, oriented urban areas and some forest areas. The color coded decomposed images of test area by Y4O, Y4R, and E4D methods are shown in Figures 3.11(a), 3.11(b), and 3.11(c), respectively. The effectiveness of the proposed scheme is analyzed by taking three different patches from the test image. For quantitative comparison, the classification accuracies of E4D over three selected patches are evaluated and compared with the performances of Y4O and Y4R. The selected three patches A, B and C from the test image are shown in Figure 3.10(a). The first patch

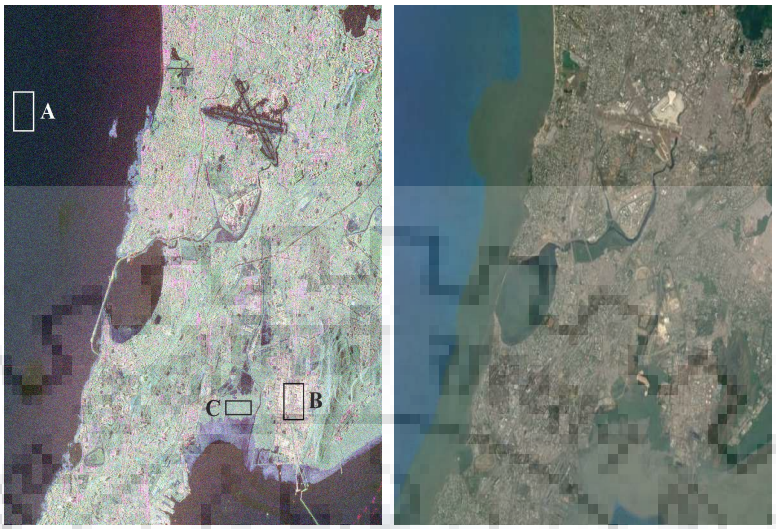

(a) (b)

Figure 3.10: Radarsat-2 Mumbai images. (a) Pauli RGB. (b) Optical Image.

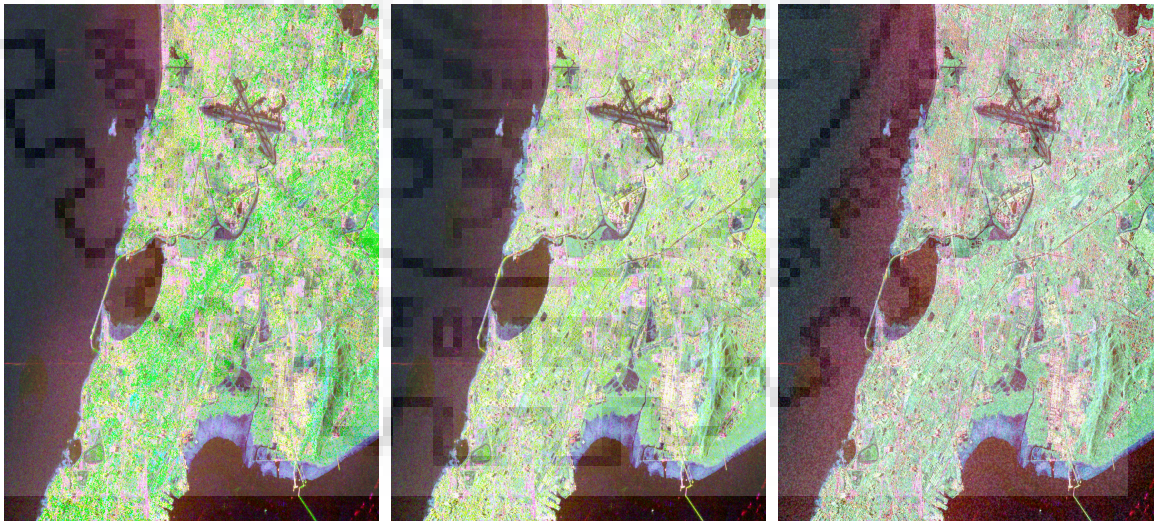

(a) (b) (c)

Figure 3.11: Color coded decomposed images of Radarsat-2 Mumbai data. (a) Y4O (b) Y4R (c) E4D.

A is selected in the Arabian sea (dominant single-bounce scattering feature), the second patch B is selected from the Bharat Petroleum Refinery area which contains buildings (dominant double-bounce scattering feature), and the third patch C is selected from the forest (dominant volume scattering feature) region.

Table 3.2: Classification accuracies of selected land-covers in percentage (%)

Land Covers	Y4O	Y4R	E4D
Patch A (Sea)	92.06	92.11	92.05
Patch B (Buildings)	57.72	62.59	66.51
Patch C (Forest)	82.89	81.38	81.14

The classification accuracies of the aforementioned decomposition schemes over three selected areas are summarized in Table 3.2. In the selected patch A, the dominant single-bounce scattering mechanism is correctly identified by all the aforementioned decomposition schemes with nearly equal accuracies. However, the mentioned decomposition schemes show some variation in statistics for patch B. The dominant scattering mechanism for this patch is double-bounce, which is identified by the Y4O with an accuracy of 57.72%. Y4R method classified this patch with an accuracy of 62.59% which is better than the performance of the Y4O. In case of E4D method, the classification accuracy of patch B is 66.51% which clearly shows that the performance of E4D is better than the other two, Y4O and Y4R. The third patch C is selected in the forest region where volume scattering mechanism is dominant. The statistics of different decomposition methods for patch C can be seen from the Table 3.2. This forest area is well classified by all the aforementioned decomposition methods. The classification accuracy for Patch C is more than 80% for all the aforementioned decomposition schemes.

The experimental results from two different fully polarimetric SAR sensors validate the robustness of the proposed decomposition method. The results clearly indicate that E4D method is efficient in classifying the complex oriented urban areas while maintaining the performances over single-bounce and volume scattering dominant areas.

3.5 Conclusion

An extended four-component decomposition (E4D) model is presented in this chapter. The scattering matrix of rotated dihedral corner reflector has been used to model the oriented dihedral structures. In addition to it, consideration of the orientation angle of urban structures empowered E4D method to use the valuable information contained in the real part of T_{23} element of coherency matrix. This enabled the characterization of cross-polarization scattering in urban environment which leads to better decomposition results.

The decomposition method is tested on the fully polarimetric AIRSAR San Francisco and Radarsat-2 Mumbai images and the classification results have been compared with Y4O and Y4R which clearly showed that E4D classify all types of land covers more efficiently.

Chapter 4

Optimization of Coherency Matrix Through Selective Unitary Rotations

4.1 Introduction

Chapter 3 is focused on the modeling of cross-polarization power from oriented dihedral structures. Oriented dihedral structures shift the polarization orientation angle (POA) which in turn generate cross-polarization power. Basically, cross-polarization refers to any process that causes coupling of energy between orthogonal states of polarization [2]. Not only oriented dihedral structures but also terrain azimuth slope and large scale roughness of the surface can result in cross-polarization backscattering. The cross-polarization generation from these targets creates scattering mechanism ambiguity. To avoid this ambiguity, the cross-polarization power caused by sloped and oriented targets should be minimized. In this context, the matrix rotation theory has gained a great popularity in recent years. The inception of the rotation theory arose from the fact that the scattering from a target highly depends on its relative orientation with respect to radar illumination. This dependency on relative orientation should be removed in order to correctly interpret the physical parameters of the target [110]. The process of reducing this orientation dependency is known as deorientation [17], [79]. Deorientation also known as orientation angle compensation (OAC) is a process that transforms the target orientation into a state of minimum cross-polarization power [79]. In OAC, the measured coherency matrix is rotated through a special unitary matrix to compensate the effects of orientation of the scatterers [102]. The concept of OAC is extended by Singh *et al.* [108] in general four-component decomposition (G4U) where authors proposed the double unitary transformations of the coherency matrix. The applicability of G4U is further increased in [109] through adaptive unitary rotations. The unitary rotations are not limited to the coherency matrix only. Generalized scattering models by utilizing unitary rotations are also pro-

posed to accommodate the cross-polarization power from depolarizing targets [110]. The potential of uniform matrix rotation theory is well discussed by Chen *et al.* [128] where authors explored the possibilities of coherency matrix transformations with different rotation angles. These literature have successfully shown that the coherency matrix can be exploited more efficaciously by unitary transformations.

Ideally, the measured coherency matrix should be completely deoriented to avoid any scattering mechanism ambiguity. However, it is almost impossible to completely extract the target orientation [79]. That is why only the partial deorientation could be applied to the fully polarimetric coherency matrix. This chapter deals with minimizing the influence of target orientation along with slope and tilt effects on coherency matrix. To accomplish this, four special unitary SU(3) matrices [1]- [2] are utilized to optimize the coherency matrix. In the proposed method, cross-polarization minimization is addressed separately for sloped surfaces and oriented urban areas. By doing so, the deorientation is maximized. Moreover, with this approach, the decrement in the cross-polarization power results in the increment of the underlying dominant co-polar scattering mechanism power. The novelty of the proposed selective unitary rotations resides in its ability to utilize all the four unitary rotations in a single decomposition scheme based on the dominance of underlying scattering mechanism.

4.2 Special unitary SU(3) group

The special unitary SU(3) matrices are derived from special unitary SU(2) group [1]- [2]. These unitary matrices obey the following properties.

$$[U]^{-1} = [U]^{*T}, \text{ and } det([U]) = 1 \tag{4.1}$$

where $[U]$ is the 3×3 special unitary matrix. To fulfil the research objective, four unitary rotation matrices from SU(3) group are utilized. These unitary rotations matrices are given as

$$[U(\vartheta_1)] = \begin{bmatrix} 1 & 0 & 0 \\ 0 & \cos 2\vartheta_1 & \sin 2\vartheta_1 \\ 0 & -\sin 2\vartheta_1 & \cos 2\vartheta_1 \end{bmatrix}, [U(\vartheta_2)] = \begin{bmatrix} 1 & 0 & 0 \\ 0 & \cos 2\vartheta_2 & j\sin 2\vartheta_2 \\ 0 & j\sin 2\vartheta_2 & \cos 2\vartheta_2 \end{bmatrix}, \tag{4.2}$$

$$[U(\varphi_1)] = \begin{bmatrix} \cos 2\varphi_1 & 0 & \sin 2\varphi_1 \\ 0 & 1 & 0 \\ -\sin 2\varphi_1 & 0 & \cos 2\varphi_1 \end{bmatrix}, [U(\varphi_2)] = \begin{bmatrix} \cos 2\varphi_2 & 0 & j\sin 2\varphi_2 \\ 0 & 1 & 0 \\ j\sin 2\varphi_2 & 0 & \cos 2\varphi_2 \end{bmatrix}. \tag{4.3}$$

One can see that (4.2) and (4.3) contain two pairs of unitary rotation matrices. Each pair consists of a real and a complex unitary rotation matrix. The unitary transformations through these rotation matrices do not alter the span of the coherency matrix. OAC utilizes the real unitary rotation matrix of (4.2) to remove the real part of T_{23} element, which in turn reduces the cross-polarization power of coherency matrix as discussed in Section 2.2. The transformed coherency matrix elements after OAC can be given as

$$T_{11}(\vartheta_1) = T_{11} \tag{4.4a}$$
$$T_{12}(\vartheta_1) = T_{12}\cos 2\vartheta_1 + T_{13}\sin 2\vartheta_1 \tag{4.4b}$$
$$T_{13}(\vartheta_1) = T_{13}\cos 2\vartheta_1 - T_{12}\sin 2\vartheta_2 \tag{4.4c}$$
$$T_{22}(\vartheta_1) = T_{22}\cos^2 2\vartheta_1 + T_{33}\sin^2 2\vartheta_1 + \Re(T_{23})\sin 4\vartheta_1 \tag{4.4d}$$
$$T_{23}(\vartheta_1) = \Im(T_{23}) \tag{4.4e}$$
$$T_{33}(\vartheta_1) = T_{33}\cos^2 2\vartheta_2 + T_{22}\sin^2 2\vartheta_2 - \Re(T_{23})\sin 4\vartheta_1. \tag{4.4f}$$

The transformation of coherency matrix can be further extended to remove the imaginary part of T_{23}, so that the cross-polarization power is further reduced [108]. This transformation can be achieved with the help of complex rotation matrix given in (4.2) as

$$[T(\vartheta_2)] = [U(\vartheta_2)][T(\vartheta_1)][U(\vartheta_2)]^{*T}. \tag{4.5}$$

The rotation angle ϑ_2 for this transformation can be found by minimizing the cross-polarization term $T_{33}(\vartheta_2)$ as

$$\vartheta_2 = \frac{1}{4}\tan^{-1}\left(\frac{2\Im(T_{23}(\vartheta_1))}{T_{22}(\vartheta_1) - T_{33}(\vartheta_1)}\right). \tag{4.6}$$

After this transformation, the coherency matrix elements are transformed as

$$T_{11}(\vartheta_2) = T_{11} \tag{4.7a}$$
$$T_{12}(\vartheta_2) = T_{12}(\vartheta_1)\cos 2\vartheta_2 - jT_{13}(\vartheta_1)\sin 2\vartheta_2 \tag{4.7b}$$
$$T_{13}(\vartheta_2) = T_{13}(\vartheta_1)\cos 2\vartheta_2 - jT_{12}(\vartheta_1)\sin 2\vartheta_2 \tag{4.7c}$$
$$T_{22}(\vartheta_2) = T_{22}(\vartheta_1)\cos^2 2\vartheta_2 + T_{33}(\vartheta_1)\sin^2 2\vartheta_2 + \Im(T_{23}(\vartheta_1))\sin 4\vartheta_2 \tag{4.7d}$$
$$T_{23}(\vartheta_2) = 0 \tag{4.7e}$$
$$T_{33}(\vartheta_2) = T_{33}(\vartheta_1)\cos^2 2\vartheta_2 + T_{22}(\vartheta_1)\sin^2 2\vartheta_2 - \Im(T_{23}(\vartheta_1))\sin 4\vartheta_2. \tag{4.7f}$$

4.2.1 T_{13} Element Removal in Dominant Surface Scattering Areas

The coherency matrix transformations described in (2.24) and (4.5) account for the minimization of cross-polarization power by decoupling the energy between double-bounce

and volume scattering mechanisms represented by T_{23} term. Both of these transformations concentrated the reduced power from cross-polarization channel (T_{33}) to double-bounce scattering channel (T_{22}). This always empowers the double-bounce scattering power irrespective of the underlying dominant scatterer. However, it has been demonstrated that terrain azimuth slope leads to cross-polarization as well [2]. Therefore, in dominant surface scattering areas, the minimization of cross-polarization power should be attained in a way so that the reduced cross-polarization power will be concentrated on the surface scattering channel (T_{11}). To realize this, unitary rotation matrices defined in (4.3) are utilized.

The proposed unitary transformations decouple the energy between surface and volume scattering mechanisms represented by T_{13} element of the coherency matrix. The first transformation of the coherency matrix to remove $\Re(T_{13})$ term can be achieved as [129]

$$[T(\varphi_1)] = [U(\varphi_1)][T][U(\varphi_1)]^{*T}. \tag{4.8}$$

The rotation angle for this transformation can be found either by minimizing cross-polarization term of $[T(\varphi_1)]$ or by finding the null angle for $\Re(T_{13}(\varphi_1))$ as

$$\vartheta_1 = \frac{1}{4}\tan^{-1}\left(\frac{2\Re(T_{13})}{T_{11}-T_{33}}\right). \tag{4.9}$$

The coherency matrix elements after this transformation are given by

$$T_{11}(\varphi_1) = T_{11}\cos^2 2\varphi_1 + T_{33}\sin^2 2\varphi_1 + \Re(T_{13})\sin 4\varphi_1 \tag{4.10a}$$
$$T_{12}(\varphi_1) = T_{12}\cos 2\varphi_1 + T_{23}^{*}\sin 2\varphi_1 \tag{4.10b}$$
$$T_{13}(\varphi_1) = j\Im(T_{13}) \tag{4.10c}$$
$$T_{22}(\varphi_1) = T_{22} \tag{4.10d}$$
$$T_{23}(\varphi_1) = T_{23}\cos 2\varphi_1 - T_{12}^{*}\sin 2\varphi_1 \tag{4.10e}$$
$$T_{33}(\varphi_1) = T_{33}\cos^2 2\varphi_1 + T_{11}\sin^2 2\varphi_1 - \Re(T_{13})\sin 4\varphi_1. \tag{4.10f}$$

The second unitary transformation of the coherency matrix to completely remove T_{13} element as well as to further reduce the cross-polarization power can be achieved as

$$[T(\varphi_2)] = [U(\varphi_2)][T(\varphi_1)][U(\varphi_2)]^{H}. \tag{4.11}$$

The rotation angle for this transformation is given by

$$\varphi_2 = \frac{1}{4}\tan^{-1}\left(\frac{2\Im(T_{13}(\varphi_1))}{T_{11}(\varphi_1)-T_{33}(\varphi_1)}\right) \tag{4.12}$$

which can be found in the same way either by minimizing the cross-polarization term $T_{33}(\varphi_2)$ or by finding the null angle for $\Im(T_{13}(\varphi_2))$. The transformed coherency matrix elements after this rotation are given as

$$T_{11}(\varphi_2) = T_{11}(\varphi_1)\cos^2 2\varphi_2 + T_{33}(\varphi_1)\sin^2 2\varphi_2 + \Im(T_{13}(\varphi_1))\sin 4\varphi_2 \tag{4.13a}$$

$$T_{12}(\varphi_2) = T_{12}(\varphi_1)\cos 2\varphi_2 + jT_{23}^*(\varphi_1)\sin 2\varphi_2 \tag{4.13b}$$

$$T_{13}(\varphi_2) = 0 \tag{4.13c}$$

$$T_{22}(\varphi_2) = T_{22}(\varphi_1) \tag{4.13d}$$

$$T_{23}(\varphi_2) = T_{23}(\varphi_1)\cos 2\varphi_2 - jT_{12}^*(\varphi_1)\sin 2\varphi_2 \tag{4.13e}$$

$$T_{33}(\varphi_2) = T_{33}(\varphi_1)\cos^2 2\varphi_2 + T_{11}(\varphi_1)\sin^2 2\varphi_2 - \Im(T_{13}(\varphi_1))\sin 4\varphi_2. \tag{4.13f}$$

After aforementioned coherency matrix transformations, the reduced cross-polarization power is always concentrated on the surface scattering channel (T_{11}) which can be seen from (4.10) and (4.13).

4.3 Freeman-Durdens' Decomposition (FDD) After Selective Unitary Rotations (SUR)

The main objective here is to minimize the cross-polarization power by decoupling the energy resides in off-diagonal terms of coherency matrix. However, it is impossible to make T_{13} and T_{23} terms zero at the same time through unitary rotations. Therefore, unitary transformations discussed in (2.24), (4.5), (4.8), and (4.11) are utilized on the basis of dominant scattering mechanism, so that the reduced cross-polarization power is concentrated on the underlying dominant co-polar scattering mechanism.

The dominant scattering mechanism can be found by the sign of $T_{11} - T_{22}$. The positive values of $T_{11} - T_{22}$ signifies dominant surface scattering areas for which transformations described in (4.8) and (4.11) are used. These transformations minimized the cross-polarization power by removing the coupling between surface and volume scattering mechanisms. Also, the reduced power is concentrated on T_{11} channel which further empowers the surface scattering power. Therefore, for $T_{11} - T_{22} > 0$ case, FDD model after selective unitary rotations (SUR) of the coherency matrix can be written as

$$[T(\vartheta_2)] = f_s[T]_s + f_d[T]_d + f_v[T]_v \tag{4.14}$$

where $[T]_s$, $[T]_d$, and $[T]_v$ are the matrices for single-bounce, double-bounce, and volume scattering mechanisms as described in (1.27), (1.30), and (1.35). The remaining param-

eters f_s, f_d, and f_v are the unknown model-coefficients to be determined. By comparing both sides of (4.14), solution for unknown model-coefficients is given by

$$f_v = 4T_{33}(\vartheta_2),\ f_s = T_{11}(\vartheta_2) - \frac{f_v}{2},$$

$$\beta^* = \frac{T_{12}(\vartheta_2)}{f_s},\ \text{and}\ f_d = T_{22}(\vartheta_2) - f_s|\beta|^2 - \frac{f_v}{4}. \tag{4.15}$$

For second case, i.e. $T_{11} - T_{22} \leq 0$, which represents the dominant double-bounce scattering, rotations described in (2.24) and ((4.5)) are utilized. These rotations minimized the cross-polarization power by removing the coupling between double-bounce and volume scattering mechanisms. The reduced power is concentrated on T_{22} channel which further empowers the double-bounce scattering power in its respective area. For this case, FDD model after SUR can be written as

$$[T(\varphi_2)] = f_s[T]_s + f_d[T]_d + f_v[T]_v. \tag{4.16}$$

The solution for unknown model-coefficients is given by

$$f_v = 4T_{33}(\varphi_2),\ f_d = T_{22}(\varphi_2) - \frac{f_v}{4}, \tag{4.17}$$

$$\alpha = \frac{T_{12}(\varphi_2)}{f_d},\ \text{and}\ f_s = T_{11}(\varphi_2) - f_d|\alpha|^2 - \frac{f_v}{2}. \tag{4.18}$$

The scattering powers for surface (P_s), double-bounce (P_d), and volume scattering mechanisms (P_v) can be given as

$$P_s = f_s\left(1+|\beta|^2\right),\ P_d = f_d\left(1+|\alpha|^2\right),\ \text{and}\ P_v = f_v. \tag{4.19}$$

Flowchart of FDD after SUR is shown in Figure 4.1.

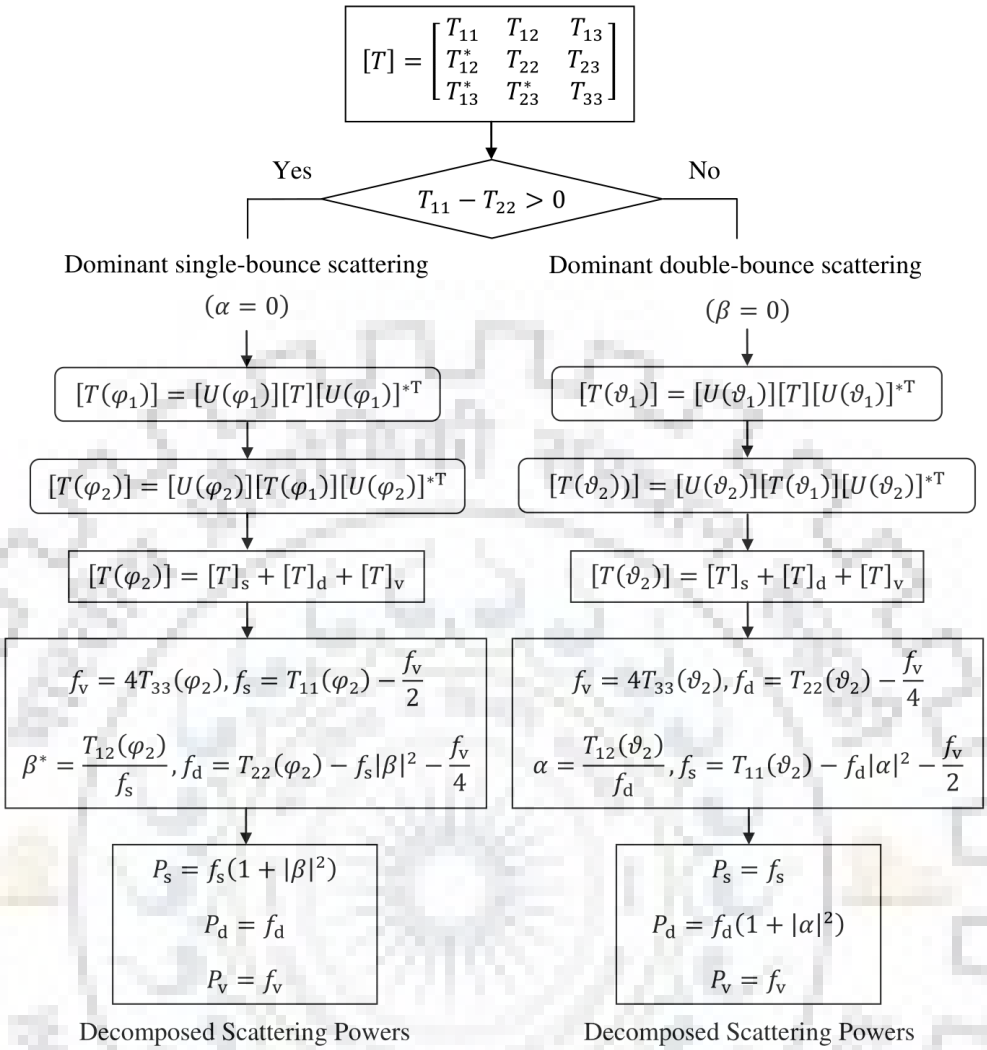

Figure 4.1: Flowchart of FDD after SUR.

4.4 Experimental Results and Discussion

In this section, the productivity of FDD after SUR is evaluated through the experiments on two different PolSAR datasets and by comparing the results with original FDD and FDD after OAC. The effectiveness can be analyzed in two manners.

1. Ability to suppress the cross-polarization power as well as the empowerments of the corresponding co-polar components.

2. Reduction in negative scattering power pixels.

4.4.1 Radarsat-2 Quebec City Data

The proposed methodology is first validated on the C-band Radarsat-2 Quebec City image [127]. The decomposed images of test site by FDD and FDD after OAC are shown in Figures 4.2(a) and 4.2(b), respectively, whereas the decomposed image by FDD after SUR method is shown in Figure 4.2(c). For analysis purpose, two urban patches are selected as shown in Figure 4.2(a). A rough estimation about the performance of FDD after SUR can be assessed from Figure 4.2. However, for proper differentiation, the quantitative comparison among the different decomposition schemes is given in Table 4.1 in terms of the normalized mean of decomposed scattering powers.

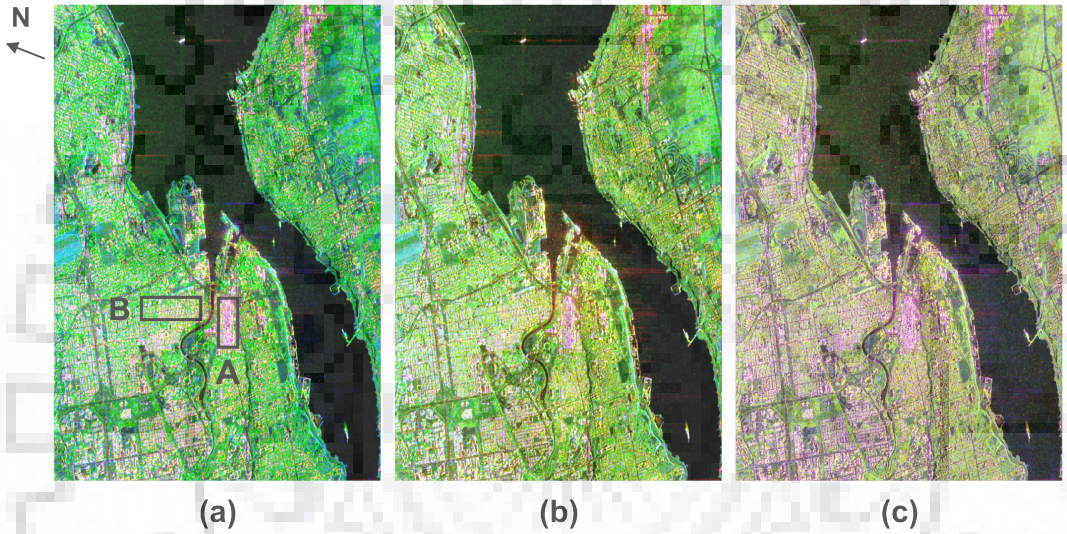

Figure 4.2: Color coded decomposed images of Radarsat-2 Quebec City (blue: surface scattering (P_s), red: double-bounce scattering (P_d), green: volume scattering (P_v)). (a) FDD. (b) FDD after OAC. (c) FDD after SUR.

Table 4.1: Normalized scattering powers mean (in %) over the selected urban patches of Radarsat-2 Quebec City image

Methods	Patch A			Patch B		
	P_s	P_d	P_v	P_s	P_d	P_v
FDD	31.08	49.19	19.73	18.58	35.64	45.78
FDD after OAC	32.09	50.42	17.49	23.45	36.14	40.41
FDD after SUR	32.61	52.45	14.94	25.01	41.01	33.98

From Table. 4.1, one can see that the normalized mean of double-bounce power (P_d) in the urban patches A and B keeps increasing as FDD $\rightarrow$ FDD after OAC $\rightarrow$ FDD after SUR. From this table, one can also notice that FDD after SUR not only increased

the P_d values in the selected urban patches but also reduced the significant amount of volume scattering contribution (P_v). This clearly reflects the advantage of using selective coherency matrix transformations rather than OAC.

Table 4.2: Percentage (%) of negative power pixels for Radarsat-2 Quebec City image

Methods	FDD	FDD after OAC	FDD after SUR
% of negative power pixels	40.63	35.32	27.51

In the next part of the analysis, the amount of negative scattering power pixels is calculated for Radarsat-2 Quebec City image by different decomposition methods as can be seen in Table 4.2. Almost all model-based decomposition schemes compute the volume scattering power first. If volume scattering contribution is overestimated which usually happens when not modeled properly, then other scattering components may have negative power contribution. Any pixel for which atleast one of the scattering power contribution is negative known as negative scattering power pixel. This is the main reason for having negative scattering power pixels in model-based decomposition methods. From Table 4.2, one can observe that FDD results in 40.63% negative power pixels. FDD after OAC reduced this amount to 35.32% by reducing volume scattering overestimation. However, the superiority of FDD after SUR can be observed which further reduces negative power pixel amount to 27.51% through selective unitary rotations of coherency matrix.

4.4.2 AIRSAR Death Valley Data

To further demonstrate the effectiveness of FDD after SUR, experiments are conducted on second PolSAR dataset acquired by L-band AIRSAR over Death Valley region [130]. The test site area comprised of the sloped desert. The decomposed images of test site by FDD, FDD after OAC, and FDD after SUR are shown in Figures. 4.3(a), 4.3(b), and 4.3(c), respectively. For analysis purpose, two patches are selected as shown in Figure 4.3(a). The percentage of normalized mean of scattering powers by different methods is tabulated in Table 4.3. From Table 4.3, one can see that the performance of FDD after SUR is better than FDD and FDD after OAC for both selected patches. One notable thing can be observed from Table 4.3 that after OAC, FDD shows only minor improvements in increment of P_s values. The P_v values of FDD after OAC are also comparable to original FDD in both selected patches. However, the single-bounce contributions (P_s) by FDD after SUR are about 5% more than that of P_s by FDD after OAC for both selected patches. Also, the volume scattering power P_v by FDD after SUR is 7% less than the P_v of FDD after OAC in both selected patches.

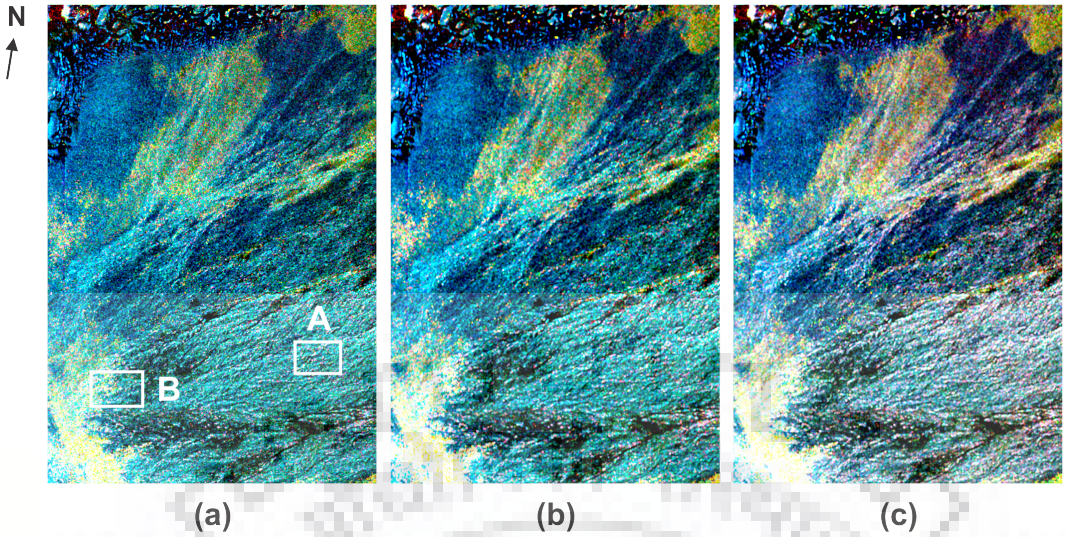

Figure 4.3: Color coded decomposed images of AIRSAR Death Valley (blue: surface scattering (P_s), red: double-bounce scattering (P_d), green: volume scattering (P_v)). (a) FDD. (b) FDD with OAC. (c) FDD after SUR.

Table 4.3: Normalized scattering powers mean (in %) over the selected desert patches of AIRSAR Death Valley image

Methods	Patch A			Patch B		
	P_s	P_d	P_v	P_s	P_d	P_v
FDD	74.30	2.38	23.32	66.74	3.12	30.14
FDD after OAC	74.80	2.71	22.49	68.18	3.61	28.21
FDD after SUR	79.37	5.18	15.45	73.93	5.02	21.05

The amount of negative power pixels by different decomposition techniques for AIRSAR Death Valley data is tabulated in Table 4.4. The percentage of negative power pixels for FDD is 16.07%. The negative power pixel count can be decreased by reducing the overestimation of volume scattering contribution. From Table 4.3, it can be observed that OAC fails to efficiently reduce the overestimation of volume scattering power which has a direct impact on the amount of negative power pixel. For this reason, FDD after OAC is less effective in reducing the negative power pixel count which can be seen from Table 4.4. The percentage of negative power pixels for FDD after OAC is 11.04%. However, an interesting result can be observed from Table 4.4, where the percentage of negative power pixels is significantly decreased to 0.77% by FDD after SUR. This significant decrement is possible because of the selective unitary rotations in dominant surface scattering areas.

Table 4.4: Percentage (%) of negative power pixels for AIRSAR Death Valley image

Methods	FDD	FDD after OAC	FDD after SUR
% of negative power pixels	16.07	11.04	0.77

4.5 Conclusions

In this chapter, a methodology is presented to optimize the fully polarimetric coherency matrix. The optimization is achieved by the selective coherency matrix transformations using special unitary SU(3) matrices based on underlying dominant scattering mechanism. This not only minimized the cross-polarization power but also channelized the amount of decreased cross-polarization power to underlying dominant co-polar scattering mechanism. The effectiveness of the approach has been shown through the implementation of FDD on optimized coherency matrices for two different PolSAR datasets. It has been demonstrated that the FDD after SUR reduces more cross-polarization power in all types of incoherently scattering areas along with corresponding increase in the underlying co-polar components in comparison to FDD after OAC. In addition, the negative power pixel count is also found to be significantly decreased by FDD after SUR approach. The aforementioned amenities make FDD after SUR distinct and more suitable for PolSAR data decomposition in comparison to other relevant literature.

Chapter 5

Non-negative Scattering Power Decomposition

5.1 Introduction

As discussed in Section 1.4, the basic reason behind the occurrence of negative scattering power is the overestimation of one of the scattering components. The sum of the contributions of all the scattering components must be equal to the span or total power of the observed coherency matrix. In case any of the scattering component's power is overestimated at any pixel, then at that pixel the remaining scattering components may have negative contributions so that the total power or *span* remains constant. A pixel that has negative scattering powers for any or more than one of the scattering components is regarded as the negative power pixel. In most of the model-based decomposition methods, volume scattering contribution is calculated first. Therefore, the negative scattering powers for co-polarized scattering mechanisms (surface and dihedral) is mainly generated by overestimation of the volume scattering contribution. In recent years, many literature reduced the overestimation of volume scattering component either by introducing new scattering models or by proposing coherency matrix transformations. New scattering models reduce the overestimation of volume scattering contribution either by better characterization of vegetation or by modeling the cross-polarization power generated from sloped and oriented scatterers [74]- [90]. Whereas in unitary transformations, overestimation of volume scattering is reduced by rotating the coherency matrix through an angle obtained by minimizing the cross-polarization power [88], [79]- [109]. By both of aforementioned methods, amount of negative power pixels can be abated. However, decreasing negative power pixels has always been the secondary concern of the aforementioned literature which came through by appropriate modeling of radar backscattering.

The most adequate literature category where the primary concern is the removal of

negative power pixels belongs to hybrid decomposition. In hybrid decomposition category, eigenvector and eigenvalue information utilized together with the physical scattering models to overcome the negative power problem. This category was commenced by Cloude [2]. Thereafter many excellent works have been reported where the negative power problem of model-based decomposition method is targeted [112]- [100]. However, in all of the aforementioned literature, Cloude's hybrid approach is the simplest one. Therefore, in this chapter, the applicability of Cloude's hybrid three-component decomposition method is extended to a hybrid four-component decomposition (HFCD) method. Along with the extension of Cloude's approach to remove negative power problem of four-component decomposition method, some additional modifications are adapted to further enhance the decomposition result.

5.1.1 Hybrid Three-Component Decomposition

In 2010, Cloude [2] proposed a hybrid three-component decomposition method. In this hybrid decomposition method, surface and dihedral scattering models are characterized by eigenvectors and eigenvalues of coherency matrix, while the volume scattering matrix is kept same as that of FDD method. Cloude's three-component decomposition method can be described as

$$[T] = [T]_{\mathrm{s}} + [T]_{\mathrm{d}} + [T]_{\mathrm{v}} \tag{5.1}$$

where $[T]$ is the measured coherency matrix, and $[T]_{\mathrm{s}}$, $[T]_{\mathrm{d}}$, $[T]_{\mathrm{v}}$ are the matrices for single-bounce, double-bounce, and volume scattering mechanisms, respectively, given by

$$[T]_{\mathrm{s}} = m_{\mathrm{s}} \begin{bmatrix} \cos^2\alpha_{\mathrm{s}} & \cos\alpha_{\mathrm{s}} \sin\alpha_{\mathrm{s}} e^{\mathrm{j}\phi_{\mathrm{s}}} & 0 \\ \cos\alpha_{\mathrm{s}} \sin\alpha_{\mathrm{s}} e^{-\mathrm{j}\phi_{\mathrm{s}}} & \sin^2\alpha_{\mathrm{s}} & 0 \\ 0 & 0 & 0 \end{bmatrix} \tag{5.2}$$

$$[T]_{\mathrm{d}} = m_{\mathrm{d}} \begin{bmatrix} \cos^2\alpha_{\mathrm{d}} & \cos\alpha_{\mathrm{d}} \sin\alpha_{\mathrm{d}} e^{\mathrm{j}\phi_{\mathrm{d}}} & 0 \\ \cos\alpha_{\mathrm{d}} \sin\alpha_{\mathrm{d}} e^{-\mathrm{j}\phi_{\mathrm{d}}} & \sin^2\alpha_{\mathrm{d}} & 0 \\ 0 & 0 & 0 \end{bmatrix} \tag{5.3}$$

$$[T]_{\mathrm{v}} = m_{\mathrm{v}} \begin{bmatrix} \frac{1}{2} & 0 & 0 \\ 0 & \frac{1}{4} & 0 \\ 0 & 0 & \frac{1}{4} \end{bmatrix}. \tag{5.4}$$

In aforementioned equations, m_{s}, m_{d}, and m_{v} are the scattering power coefficients for single-bounce, double-bounce, and volume scattering mechanisms, respectively. The values of α_{s} and α_{d} depend on dielectric constants of the surfaces and the angle of incidence,

whereas ϕ_s and ϕ_d are the scattering phase for single-bounce and double-bounce mechanisms, respectively [2]. The unknown parameters in (5.2) and (5.2) can be reduced by postulating orthogonality of the single- and double-bounce components as

$$\alpha_d + \alpha_s = \frac{\pi}{2}, \text{ and } \phi_d - \phi_s = \pm\pi. \tag{5.5}$$

This reduces the number of unknowns in (5.1), which can be rewritten as

$$[T] = [T]_{sd} + [T]_v, \tag{5.6}$$

where $[T]_{sd}$ is the combined rank-2 matrix for single- and double-bounce scattering mechanisms, given by

$$[T]_{sd} = \begin{bmatrix} m_s\cos^2\alpha + m_d\sin^2\alpha & \cos\alpha\,\sin\alpha e^{j\phi}\,(m_d - m_s) & 0 \\ \cos\alpha_s\,\sin\alpha e^{-j\phi}\,(m_d - m_s) & m_d\cos^2\alpha + m_s\sin^2\alpha & 0 \\ 0 & 0 & 0 \end{bmatrix}. \tag{5.7}$$

In hybrid Freeman decomposition method, volume scattering power coefficient m_v is calculated first from (5.6) as

$$m_v = 4T_{33}. \tag{5.8}$$

The other two scattering power coefficients m_d and m_s are given in (5.9) which can be computed as the eigenvalues of the remaining rank-2 coherency matrix left after subtracting the volume scattering contribution.

$$m_{d,s} = \frac{T_{11} + T_{22} - 3T_{33} \pm \sqrt{(T_{11} - T_{22} - T_{33})^2 + 4\,|T_{12}|^2}}{2}. \tag{5.9}$$

Singh *et al.* [112] introduced OAC in Cloude's hybrid Freeman decomposition method to compensate for the polarization orientation shifts as

$$[T(\vartheta_1)] = [T]_{sd} + [T]_v. \tag{5.10}$$

5.2 Hybrid Four-Component Decomposition (HFCD)

In this section, Cloude's hybrid three-component decomposition approach is extended to present a hybrid four-component decomposition (HFCD) method [131]. In addition to the extension of Cloude's approach, some additional modifications are incorporated in the HFCD approach which will be discussed along with the description of HFCD method. The HFCD method can be presented as

$$[T] = [T]_{\mathrm{sd}} + [T]_{\mathrm{v}}^{\mathrm{An}} + [T]_{\mathrm{c}}\,, \tag{5.11}$$

where $[\mathrm{T}]_{\mathrm{v}}^{\mathrm{An}}$ is An *et al.* volume scattering model [88] given in (2.18), while $[\mathrm{T}]_{\mathrm{c}}$ is the helix scattering matrix as described in (2.8). The first modification in the decomposition scheme is done by replacing the conventional uniformly distributed volume scattering model to An *et al.* [88] volume scattering model. An *et al.* [88] model has entropy equals to 1, therefore, is well suited for volume scattering phenomenon.

From (5.11), the helix scattering power coefficient is determined first by the imaginary part of T_{23} element of the coherency matrix as

$$m_{\mathrm{c}} = 2\left|\mathrm{Im}\left(T_{23}\right)\right|. \tag{5.12}$$

Rest of the scattering power coefficients can be calculated by the eigen-decomposition of the remaining matrix obtained after subtracting the helix scattering contribution from the observed coherency matrix as

$$[T]^{'} = [T] - [T]_{\mathrm{c}}\,. \tag{5.13}$$

In the above procedure, it can be possible for some pixels to have helix scattering power greater than the *span* or total power of the coherency matrix. In that case, the helix scattering contribution can be assumed to zero, so that the remaining coherency matrix will remain positive semidefinite. However, these type of pixels are negligible as compared to the total number of pixels in any test site image. Now the decomposition equation given in (5.11) can be written as

$$[T]^{'} = [T]_{\mathrm{sd}} + [T]_{\mathrm{v}}^{\mathrm{An}}\,. \tag{5.14}$$

After finding the helix scattering contribution, the second modification is done in the process of calculating the volume scattering contribution. In the HFCD scheme, instead of calculating volume scattering coefficient from cross-polarization term, eigenvalues of the remainder coherency matrix $[T]_{\mathrm{R}}\left(=[T]^{'} - [T]_{\mathrm{v}}^{\mathrm{An}}\right)$ is utilized according to the following procedure.

The remainder coherency matrix matrix $[T]_{\mathrm{R}}$ can be decomposed according to

$$[T]_{\mathrm{R}} = [U]_3\,[\Sigma]\,[U]_3^{*T}, \tag{5.15}$$

where $[U]_3$ is the 3×3 eigenvector matrix of $[T]_{\mathrm{R}}$ and $[\Sigma]$ is the diagonal eigenvalue matrix given by

$$[\Sigma] = \begin{bmatrix} \lambda_1^{'} - (m_v/3) & 0 & 0 \\ 0 & \lambda_2^{'} - (m_v/3) & 0 \\ 0 & 0 & \lambda_3^{'} - (m_v/3) \end{bmatrix}, \tag{5.16}$$

where $\lambda_1^{'}$, $\lambda_2^{'}$, and $\lambda_3^{'}$ are the eigenvalue of the matrix $[T]^{'}$ with $\lambda_1^{'} \geq \lambda_2^{'} \geq \lambda_3^{'}$. As we know that after subtracting the volume scattering contribution, the remainder coherency matrix $[T]_R$ must be of a rank-2 matrix (as that of $[T]_{sd}$). Also, the eigenvalues of the remainder matrix must be non-negative. These two aforementioned conditions can be satisfied only if the volume scattering power coefficient m_v is determined from the smallest eigenvalue of $[T]^{'}$ as

$$m_v = 3\lambda_3^{'}. \tag{5.17}$$

The rest of scattering powers m_s and m_d can be determined with the help of eigenvalues of the remainder matrix remainder matrix $[T]_R$ on the basis of dominant scattering mechanism.

For dominant single-bounce scattering case, i.e. $T_{11} - T_{22} > 0$, the surface and double-bounce scattering power coefficients m_s and m_d, respectively can be determined as

$$m_s = \lambda_{1R} = \lambda_1^{'} - \lambda_3^{'} \tag{5.18}$$

$$m_d = \lambda_{2R} = \lambda_2^{'} - \lambda_3^{'}. \tag{5.19}$$

Whereas for $T_{11} - T_{22} \leq 0$ which represents the dominant double-bounce scattering case, m_s and m_d can be determined as

$$m_s = \lambda_{2R} = \lambda_2^{'} - \lambda_3^{'} \tag{5.20}$$

$$m_d = \lambda_{1R} = \lambda_1^{'} - \lambda_3^{'}. \tag{5.21}$$

where λ_{1R} and λ_{2R} are the eigenvalues of the remainder matrix $[T]_R$ with $\lambda_{1R} \geq \lambda_{2R}$. Since the eigenvalues are arranged such that the condition $\lambda_1^{'} \geq \lambda_2^{'} \geq \lambda_3^{'}$ always satisfies, the scattering powers m_s and m_d will always be non-negative.

The last modification in the hybrid approach is implemented by incorporating the unitary matrix rotations described in Section 4.2. With that, the performance of the HFCD method is further increased through coherency matrix optimization. Unitary transformations presented in Section 4.2 can be applied to the matrix $[T]^{'}$ on the basis of the dominant scattering mechanism as

$$[T]^{'} = \begin{cases} [T(\varphi_2)]^{'} & \text{if } T_{11} - T_{22} > 0 \\ [T(\vartheta_1)]^{'} & \text{if } T_{11} - T_{22} \leq 0 \end{cases} \tag{5.22}$$

Here the unitary transformations have been applied after subtracting the helix scattering contribution from the measured coherency matrix. By doing this, one of the unitary transformation given in (4.5) can be skipped as the imaginary part of the T_{23} element will become zero after the subtraction of the helix scattering power. The flowchart of the HFCD method is shown in Figure 5.1.

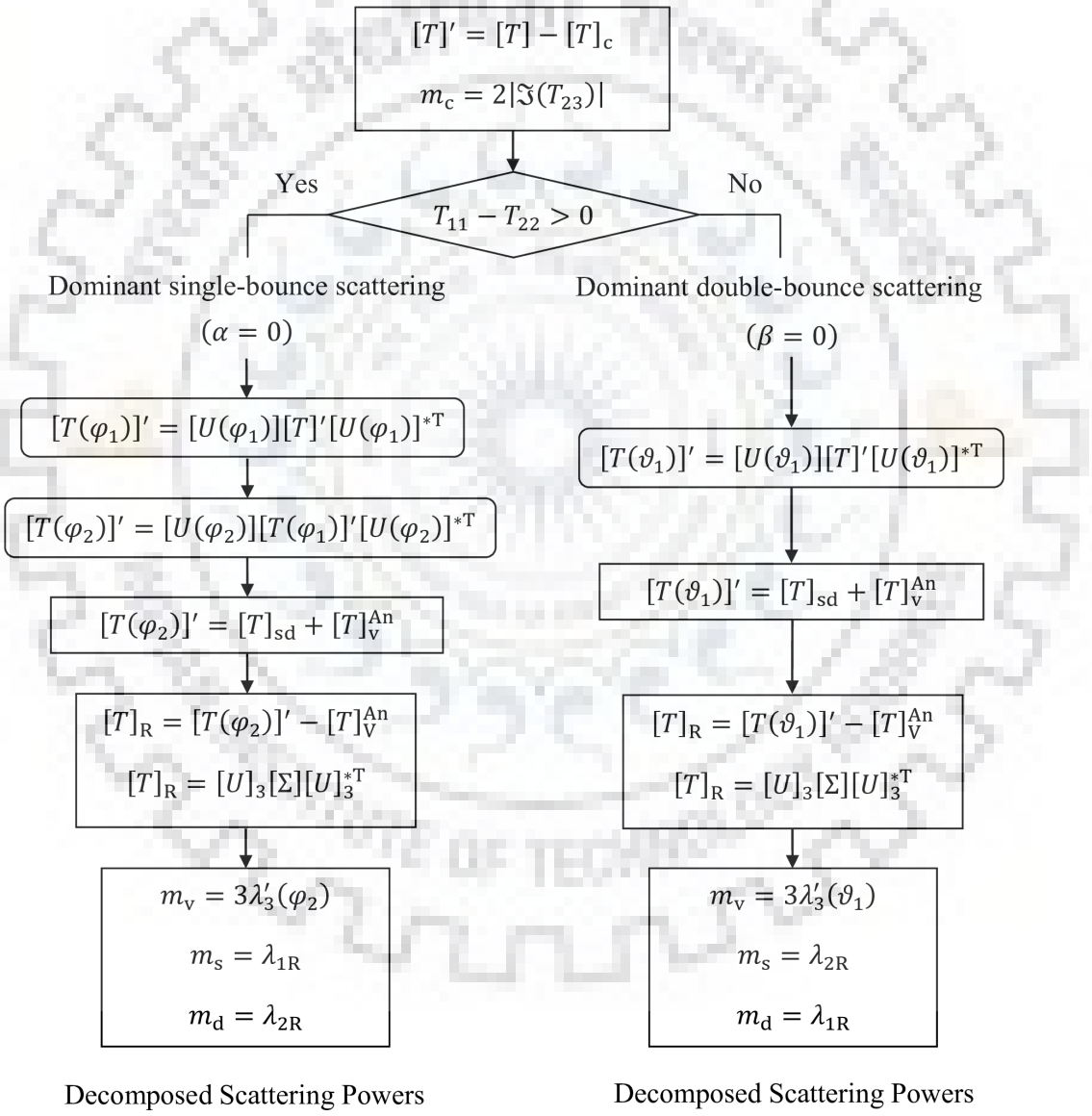

Figure 5.1: Flowchart of HFCD Method.

5.3 Results and Discussion

Experiments on two different PolSAR datasets are performed to validate the efficacy of the HFCD technique. The first dataset is acquired over San Francisco Bay area by the C-band spaceborne satellite Radarsat-2, whereas the second dataset is of Hayward area obtained by the L-band airborne UAVSAR (uninhabited aerial vehicle synthetic aperture radar). The effectiveness of the HFCD technique is evaluated on the basis of the two factors.

1. Improvements in the decomposition parameters in comparison to the state-of-the-art PolSAR decomposition techniques.
2. Percentage of negative power pixels.

5.3.1 Radarsat-2 San Francisco Bay Data

The C-band Radarsat-2 data over San Francisco bay area was acquired by the Fine quad-beam (FQ9) mode. The San Francisco data contains different types of land-covers. The Pauli RGB image of the San Francisco area is shown in Figure 5.2. For the quantitative analysis purpose, four patches are selected from different land-cover areas as shown in Figure 5.2. Patch A and patch B are selected from the two different urban areas, whereas patch C and patch D are selected from the ocean and park areas, respectively.

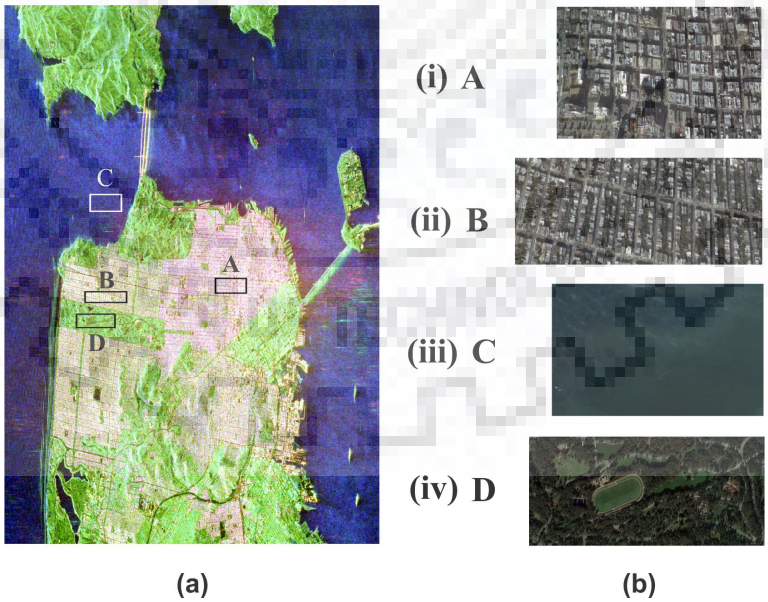

Figure 5.2: C-band Radarsat-2 San Francisco image. (a) Pauli RGB image of Radarsat-2 San Francisco area with selected land-cover patches used for analysis. (b) Optical view of selected land-cover patches.

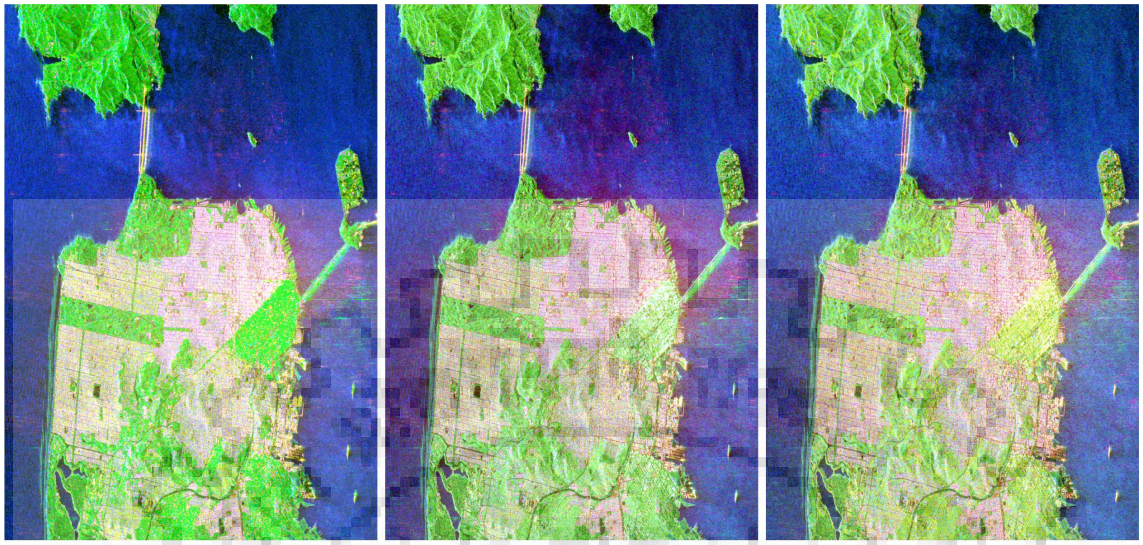

(a) (b) (c)

Figure 5.3: Color coded decomposed images of C-band Radarsat-2 San Francisco area. (a) Y4O. (b) Y4R. (c) HFCD.

Table 5.1: Normalized scattering powers mean (in %) over selected land-cover patches of Radarsat-2 San Francisco image (For all the three decomposition methods, An *et al.* [88] volume scattering matrix is used)

Methods	**Patch A**			**Patch B**		
	m_s	$m_d + m_c$	m_v	m_s	$m_d + m_c$	m_v
Y4O	39.99	54.78	5.23	37.46	46.77	15.69
Y4R	41.00	56.40	2.60	41.38	51.66	6.96
HFCD	39.77	58.18	2.05	41.46	54.34	4.20
Methods	**Patch C**			**Patch D**		
	m_s	$m_d + m_c$	m_v	m_s	$m_d + m_c$	m_v
Y4O	94.47	3.27	2.26	42.76	12.94	44.30
Y4R	94.55	3.38	2.06	43.87	13.35	42.78
HFCD	95.86	2.95	1.19	44.47	14.10	41.43

The performance of the HFCD is evaluated and compared with Y4O and Y4R. For comparison purpose, color coded decomposed images of Y4O, Y4R, and the HFCD are shown in Figures 5.2(a), 5.2(b), and 5.2(c), respectively. The normalized scattering powers mean by different decomposition methods are computed and tabulated in Table 5.1 for the selected land-cover patches as shown in Figure 5.2. This term is calculated by the normalized sum of scattering powers with respect to the *span* over the entire range of pixels. From Table 5.1, one can observe the potency of the HFCD in classifying the urban areas. The results of HFCD are much better than Y4O and Y4R in urban patches A and B. The comparison can be analyzed in two manners. First by finding the contribution of $(m_d + m_c)$ in urban patches, and secondly by finding how minimum is the volume scattering power m_v in that particular patch. In both the aforementioned criteria, the HFCD gives better decomposition results. The same is true for the ocean patch C, where not only the contribution of m_s by HFCD is higher than that of the two state-of-the-art methods, but also m_v contribution get reduced. The last patch D is selected from the Golden Gate Park area. From Table 5.1, one can see that in patch D, m_v derived by HFCD is less in comparison to the other two methods. The reason behind this is well explained in Section 3.4.1.

Table 5.2: Percentage (%) of negative power pixels by different methods with An *et al.* [88] volume scattering model for Radarsat-2 San Francisco image

Methods	Y4O	Y4R	HFCD
% of negative power pixels	17.08	11.02	0

The negative power analysis is also carried out for different decomposition methods. From Table 5.2, one can see the huge differences in the amount of total negative scattering power pixels for different methods. The amounts of negative power pixels are 17.08% and 11.02% by Y4O and Y4R, respectively. However, the negative scattering powers are completely eliminated by the HFCD method.

5.3.2 UAVSAR Hayward Data

To further authenticate the proposed hybrid decomposition methodology, experiments are conducted on another dataset acquired over the Hayward area by L-band UAVSAR airborne sensor [132]. The Pauli RGB image of the test site is shown in Figure 5.4. The test image of the Hayward area composed of Bay, forests, and urban areas.

For visual comparison purpose, the color coded decomposed images of test site by different decomposition methods are shown in Figure 5.5. The quantitative analysis has been carried out in terms of normalized scattering powers mean for the two urban patches

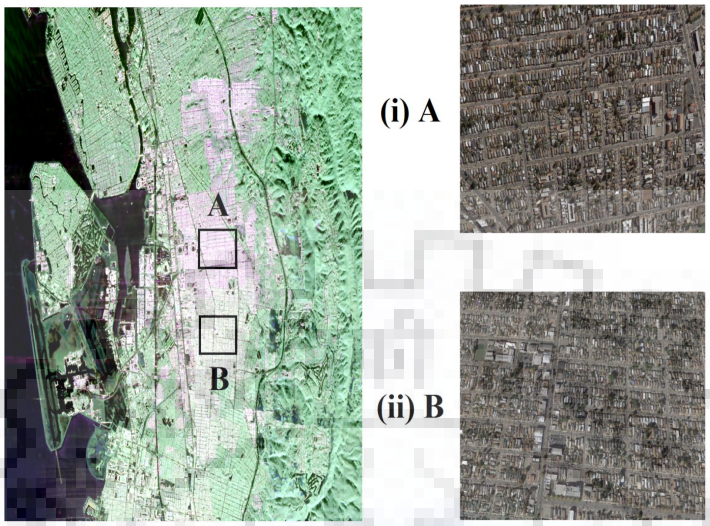

Figure 5.4: L-band UAVSAR Hayward image. (a) Pauli RGB image of UAVSAR Hayward area with selected urban patches used for analysis. (b) Optical view of selected urban patches.

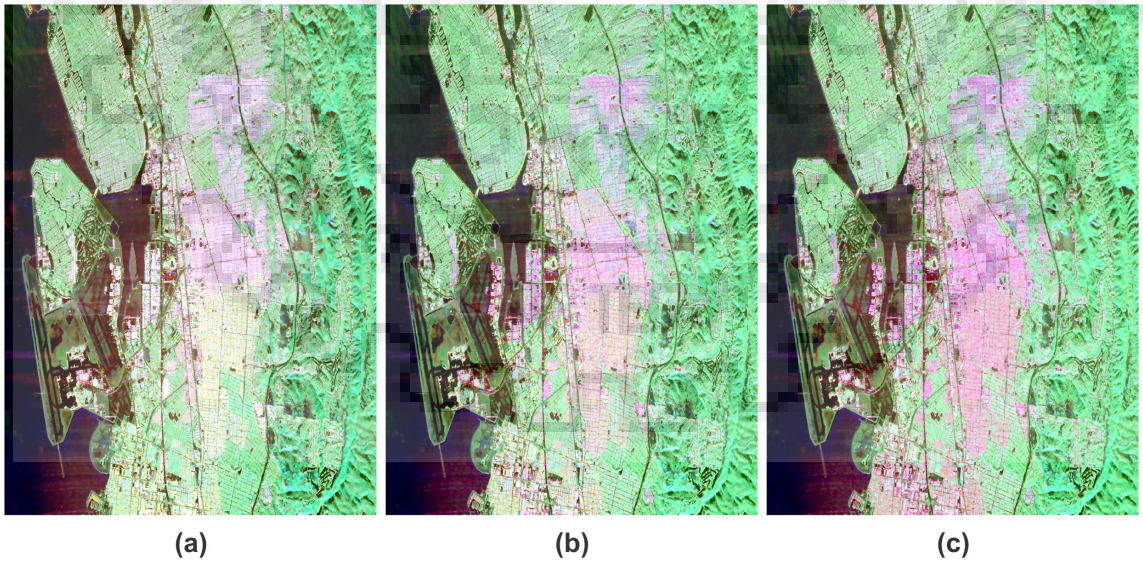

Figure 5.5: Color coded decomposed images of L-band UAVSAR Hayward area. (a) Y4O. (b) Y4R. (c) HFCD.

A and B as shown in Figure 5.4. The comparative analysis among different decomposition techniques are tabulated in Table 5.3. The increment in the $(m_d + m_c)$ values with the proposed methodology can be seen from Table 5.3. HFCD method also decreased the significant amount of the volume scattering strength in the urban environment which can be observed from Table 5.3. To further analyze, the power image of m_v for Y4O, Y4R, and HFCD methods are shown in Figure 5.6. In Figure 5.6, the red box covers the urban areas of the test site. From this figure, we can see that the strength of m_v in urban areas is very less for the HFCD as compared to Y4O and Y4R.

Table 5.3: Normalized scattering powers mean (in %) over selected urban patches of UAVSAR Hayward image

Methods	Patch A			Patch B		
	m_s	$m_d + m_c$	m_v	m_s	$m_d + m_c$	m_v
Y4O	35.06	51.75	13.19	24.39	43.84	31.77
Y4R	36.84	54.41	8.75	30.00	52.39	17.61
HFCD	36.32	57.16	6.12	29.42	56.24	14.34

Figure 5.6: Volume scattering power (m_v) for UAVSAR Hayward image. (a) Y4O. (b) Y4R. (c) HFCD.

The negative power analysis of the Hayward data for different decomposition methods is tabulated in Table 5.4. The size of the Hayward test site image is 1852×1937 pixels. With An *et al.* volume scattering model, Y4O and Y4R manage to have less amount of negative power pixels for this data, however, the HFCD still dominates over both of them with zero negative power pixels.

Table 5.4: Percentage(%) of negative power pixels by different methods with An *et al.* [88] volume scattering model for UAVSAR Hayward image

Methods	Y4O	Y4R	HFCD
% of negative power pixels	4.77	3.61	0

5.4 Conclusions

In this chapter, an extended hybrid decomposition technique is presented to overcome the negative power problem of model-based decomposition methods. In the proposed hybrid decomposition technique, conventional surface and dihedral scattering models are replaced by a rank-2 hybrid scattering model, while the conventional uniformly distributed volume scattering model is replaced by An *et al.* volume scattering model [88]. The hybrid scattering model empowers the decomposition scheme to compute the surface and dihedral scattering contributions in terms of eigenvalues of the coherency matrix. The applicability of the hybrid approach is shown through the implementation of hybrid four-component decomposition (HFCD) method. To further enhance the performance of HFCD method, selective unitary rotations are utilized on the basis of the underlying dominant scatterer. These rotations remove maximal of the cross-polarization power generated by the coupling between orthogonal states of polarization. Comparative analyses of HFCD with existing PolSAR decomposition techniques are presented in terms of normalized scattering power means and the percentage of negative power pixels. All experimental analyses clearly report the superiority of HFCD method through improvements over existing PolSAR decomposition techniques along with non-negative scattering powers.

Chapter 6

Investigation of Branching Condition in Model-Based Decomposition Methods

6.1 Introduction

Three previous chapters of the thesis were concerned about the major challenges in model-based decomposition methods. In these previous chapters, either new scattering models or new unitary rotations are explored to address the challenges. However, besides all these challenges and improvements, an interesting fact of model-based decomposition methods is that they result in an under-determined system. Almost all the model-based decomposition methods have more number of unknowns than equations. Therefore, some assumptions and constraints are applied to solve the unknowns. These constraints are known as branching conditions, which decide the dominance of a scattering mechanism and accordingly some unknowns are fixed. In conventional model-based decomposition methods, after subtracting the volume scattering contribution from the measured coherency matrix, the dominance of single- or double-bounce scattering mechanism is determined by the sign of $\Re\left(S_{\mathrm{HH}}S_{\mathrm{VV}}^{*}\right)$ or $T_{11}-T_{22}$ [34]- [35]. Based on this branching condition, the contributions of the single- and double-bounce scattering coefficients β and α are determined from the T_{12} term of the coherency matrix. The pixel-wise solution of unknowns β and α based on the sign of $\Re\left(S_{\mathrm{HH}}S_{\mathrm{VV}}^{*}\right)$ element is tedious when the image size is large.

6.2 A Fast Alternative to Model-Based Decomposition Techniques

As can be seen from (1.27) and (1.30), T_{12} element of the coherency matrix is modeled in single- and double-bounce scattering mechanisms by the model-coefficients β and α, re-

spectively. T_{12} element represents the correlation between the single- and double-bounce scattering mechanisms. Based on the sign of branching condition, T_{12} element of the coherency matrix is used to determine the value of either β or α at a time, while the other one is forced to zero. Finally, these two coefficients are used to compute the scattering powers of their corresponding models. However, if the contribution of T_{12} is directly assigned to the single- and double-bounce scattering powers P_s and P_d, then there will be no need to calculate two unknowns β and α [133]- [134]. This will also make the decomposition schemes more computationally efficient. To achieve this, the contribution of T_{12} element is distributed to T_{11} and T_{22} elements by two unitary transformations as described in the following subsections.

6.2.1 First Unitary Transformation to Remove $\Re(T_{12})$

The first unitary rotation matrix selected from special unitary SU(3) matrix group to remove $\Re(T_{12})$ term is given by

$$[U(\omega_1)] = \begin{bmatrix} \cos 2\omega_1 & \sin 2\omega_1 & 0 \\ -\sin 2\omega_1 & \cos 2\omega_1 & 0 \\ 0 & 0 & 1 \end{bmatrix}. \tag{6.1}$$

Here ω_1 is the rotation angle for the first transformation. The coherency matrix transformation through aforementioned rotation matrix can be accomplished as

$$[T(\omega_1)] = [U(\omega_1)][T][U(\omega_1)]^{*\mathrm{T}}. \tag{6.2}$$

After transformation, the coherency matrix elements are given by

$$T_{11}(\omega_1) = T_{11}\cos^2 2\omega_1 + T_{22}\sin^2 2\omega_1 + \Re(T_{12})\sin 4\omega_1 \tag{6.3a}$$

$$T_{12}(\omega_1) = \Re(T_{12})\cos 4\omega_1 + j\,\mathrm{Im}(T_{12}) + \frac{(T_{22}-T_{11})}{2}\sin 4\omega_1 \tag{6.3b}$$

$$T_{13}(\omega_1) = T_{13}\cos 2\omega_1 + T_{23}\sin 2\omega_1 \tag{6.3c}$$

$$T_{22}(\omega_1) = T_{22}\cos^2 2\omega_1 + T_{11}\sin^2 2\omega_1 - \Re(T_{12})\sin 4\omega_1 \tag{6.3d}$$

$$T_{23}(\omega_1) = T_{23}\cos 2\omega_1 - T_{13}\sin 2\omega_1 \tag{6.3e}$$

$$T_{33}(\omega_1) = T_{33}. \tag{6.3f}$$

The rotation angle ω_1 can be derived from (6.3b) as the null angle for $\Re(T_{12})$ term as

$$\Re\{T_{12}(\omega_1)\} = 0. \tag{6.4}$$

From (6.4), the rotation or null angle ω_1 can be obtained as

$$\omega_1 = \frac{1}{4}\tan^{-1}\left(\frac{2\Re\left(T_{12}\right)}{T_{11}-T_{22}}\right). \tag{6.5}$$

6.2.2 Second Unitary Transformation to Remove $\Im(T_{12})$

After first transformation, $\Re\{T_{12}(\omega_1)\}$ becomes zero, so that $T_{12}(\omega_1) = \Im\{T_{12}\}$. To remove the remaining imaginary part, the second unitary transformation is applied on the rotated coherency matrix as

$$[T(\omega_2)] = [U(\omega_2)][T(\omega_1)][U(\omega_2)]^{*\mathrm{T}}, \tag{6.6}$$

where $[U(\omega_2)]$ is a complex unitary rotation matrix given in (6.7), and ω_2 is the rotation angle for the second transformation.

$$[U(\omega_2)] = \begin{bmatrix} \cos 2\omega_2 & j\sin 2\omega_2 & 0 \\ j\sin 2\omega_2 & \cos 2\omega_2 & 0 \\ 0 & 0 & 1 \end{bmatrix}. \tag{6.7}$$

Transformed coherency matrix elements after second rotation can be given as

$$T_{11}(\omega_2) = T_{11}(\omega_1)\cos^2 2\omega_2 + T_{22}(\omega_1)\sin^2 2\omega_2 + \Im\{T_{12}(\omega_1)\}\sin 4\omega_2 \tag{6.8a}$$

$$T_{12}(\omega_2) = j\,\Im\{T_{12}\}\cos 4\omega_2 + j\,\frac{(T_{22}(\omega_1) - T_{11}(\omega_1))}{2}\sin 4\omega_2 \tag{6.8b}$$

$$T_{13}(\omega_2) = T_{13}(\omega_1)\cos 2\omega_2 + j\,T_{23}(\omega_1)\sin 2\omega_2 \tag{6.8c}$$

$$T_{22}(\omega_2) = T_{22}(\omega_1)\cos^2 2\omega_2 + T_{11}(\omega_1)\sin^2 2\omega_2 - \Im\{T_{12}(\omega_1)\}\sin 4\omega_2 \tag{6.8d}$$

$$T_{23}(\omega_2) = T_{23}(\omega_1)\cos 2\omega_2 + j\,T_{13}(\omega_1)\sin 2\omega_2 \tag{6.8e}$$

$$T_{33}(\omega_2) = T_{33}. \tag{6.8f}$$

As can be seen from (6.8b), after second transformation, $T_{12}(\omega_2)$ contains only the imaginary part. Therefore, to completely remove T_{12} element, the rotation angle ω_2 can be derived as the null angle for $T_{12}(\omega_2)$ as

$$\omega_2 = \frac{1}{4}\tan^{-1}\left(\frac{2\Im\left(T_{12}\right)}{T_{11}(\omega_1) - T_{22}(\omega_1)}\right). \tag{6.9}$$

6.3 Alternate Decomposition Methodology

After aforementioned transformations, T_{12} element of the coherency matrix becomes zero [133]- [134]. Therefore, the scattering models for single- and double-bounce mechanisms can be modified as

$$[T]_{\mathrm{s}}^{'} = \begin{bmatrix} 1 & 0 & 0 \\ 0 & 0 & 0 \\ 0 & 0 & 0 \end{bmatrix}, \text{ and } [T]_{\mathrm{d}}^{'} = \begin{bmatrix} 0 & 0 & 0 \\ 0 & 1 & 0 \\ 0 & 0 & 0 \end{bmatrix}. \tag{6.10}$$

Now the alternate FDD model can be presented as

$$[T(\omega_2)] = f_{\mathrm{s}}[T]_{\mathrm{s}}^{'} + f_{\mathrm{d}}[T]_{\mathrm{d}}^{'} + f_{\mathrm{v}}[T]_{\mathrm{v}}. \tag{6.11}$$

On comparing the unknown model-coefficients with the elements of $[T(\omega_2)]$, the following equations are obtained.

$$T_{11}(\omega_2) = f_{\mathrm{s}} + \frac{f_{\mathrm{v}}}{2},\ T_{22}(\omega_2) = f_{\mathrm{d}} + \frac{f_{\mathrm{v}}}{4},\ \text{and } T_{33}(\omega_2) = \frac{f_{\mathrm{v}}}{4}. \tag{6.12}$$

As can be from (6.12), the number of unknowns in alternate FDD model are equal to the number of equations. Therefore, the unknowns can be determined linearly without making any assumption as

$$f_{\mathrm{v}} = 4T_{33}(\omega_2),\ f_{\mathrm{s}} = T_{11}(\omega_2) - \frac{f_{\mathrm{v}}}{2},\ \text{and } f_{\mathrm{d}} = T_{22}(\omega_2) - \frac{f_{\mathrm{v}}}{4}. \tag{6.13}$$

In case of four-component, the alternate decomposition scheme can be written as

$$[\mathrm{T}(\omega_2)] = f_{\mathrm{s}}\,[\mathrm{T}]_{\mathrm{s}}^{'} + f_{\mathrm{d}}\,[\mathrm{T}]_{\mathrm{d}}^{'} + f_{\mathrm{v}}\,[\mathrm{T}]_{\mathrm{v}} + f_{\mathrm{c}}\,[\mathrm{T}]_{\mathrm{c}}\,. \tag{6.14}$$

On comparing the unknown model-coefficients with the elements of $[T(\omega_2)]$, the following equations are obtained.

$$T_{11}(\omega_2) = f_{\mathrm{s}} + \frac{f_{\mathrm{v}}}{2},\ T_{22}(\omega_2) = f_{\mathrm{d}} + \frac{f_{\mathrm{v}}}{4},\ T_{33}(\omega_2) = \frac{f_{\mathrm{v}}}{4},\ \text{and } T_{23}(\omega_2) = \pm j\frac{f_{\mathrm{c}}}{2}. \tag{6.15}$$

Again for this case, the unknown model-coefficients can be determined without taking any assumption as

$$f_{\mathrm{c}} = 2\,|\mathrm{Im}\,(T_{23}(\omega_2))|\,,\ f_{\mathrm{v}} = 4\left(T_{33}(\omega_2) - \frac{f_{\mathrm{c}}}{2}\right),$$

$$f_{\mathrm{s}} = T_{11}(\omega_2) - \frac{f_{\mathrm{v}}}{2},\ \text{and } f_{\mathrm{d}} = T_{22}(\omega_2) - \frac{f_{\mathrm{v}}}{4} - \frac{f_{\mathrm{c}}}{2}. \tag{6.16}$$

The scattering powers for both aforementioned cases can be computed as

$$P_s = f_s,\ P_d = f_d,\ P_v = f_v,\ \text{and}\ P_c = f_c. \tag{6.17}$$

6.4 Results and Discussion

To demonstrate the Alternate FDD and Y4O decomposition schemes, fully polarimetric C-band Radarsat-2 image is used. The color coded decomposed images of the alternate three- and four-component decomposition schemes are shown in Figures 6.1(a) and 6.1(b), respectively. The decomposed images of FDD and Y4O methods are almost similar to alternate FDD and alternate Y4O, respectively and hence not included here.

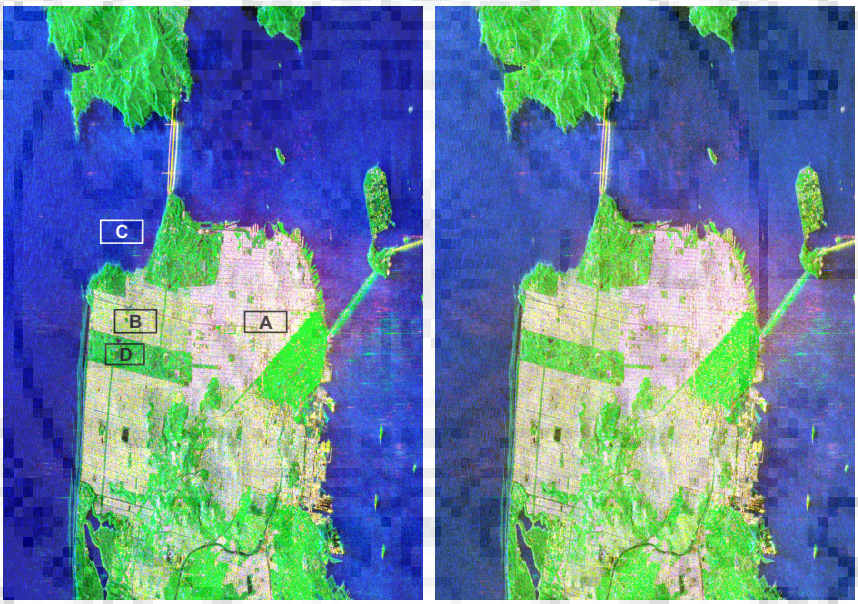

Figure 6.1: Color coded decomposed images of Radarsat-2 San Francisco area. (a) Alternate FDD. (b) Alternate Y4O.

For quantitative comparison purpose, four different land-cover patches are selected as shown in Figure 6.1(a). Patches A and B are selected from two different urban areas, whereas patch C and D are selected from ocean and park areas, respectively. Normalized scattering powers mean over aforementioned four patches are computed for alternate decomposition schemes and compared with FDD and Y4O methods in Table 6.1. From this table, one can observe that the overall decomposition results of the alternate schemes are almost similar to the original ones.

Table 6.1: Normalized scattering powers mean (in %) over selected land-cover patches of Radarsat-2 San Francisco image

Methods	Patch A			Patch B		
	P_s	$P_d + P_c^*$	P_v	P_s	$P_d + P_c^*$	P_v
FDD	32.75	48.37	18.88	27.11	38.52	34.37
Alternate FDD	32.03	49.09	18.88	26.40	39.23	34.37
Y4O	38.37	54.65	6.98	33.04	46.04	20.92
Alternate Y4O	37.82	54.89	7.29	32.84	45.67	21.49
Methods	**Patch C**			**Patch D**		
	P_s	$P_d + P_c^*$	P_v	P_s	$P_d + P_c^*$	P_v
FDD	92.97	02.46	4.57	15.95	4.10	79.95
Alternate FDD	92.98	02.45	4.57	18.04	2.01	79.95
Y4O	93.73	03.25	2.47	20.03	15.30	64.67
Alternate Y4O	93.56	03.02	3.42	23.88	7.86	68.26

(*For FDD decomposition scheme, P_c becomes zero.)

6.4.1 Computational Efficiency

The alternate and original FDD and Y4O decomposition schemes are compared in terms of computational efficiency. All the aforementioned decomposition methods are implemented on MATLAB 2012b to find out the time consumed in calculating the scattering powers for each pixel of Radarsat-2 San Francisco image. The desktop operating system is Windows 7 with 8 GB RAM and the size of the image used is 3221×1981 pixels. The time taken by the FDD and Y4O methods is 9.1872 seconds and 9.7935 seconds, respectively. Whereas for the same image, the time consumed to calculate the scattering powers by the alternate FDD and Y4O methods are 0.8952 seconds and 0.9207 seconds, respectively. Here, one can notice the vast improvement in terms of computational efficiency by the alternate decomposition methods over the original FDD and Y4O methods. The original FDD and Y4O methods have more number of equations than the number of unknowns, therefore, to calculate the values of unknowns β and α, sign of $\Re\left(S_{\mathbf{HH}}S_{\mathbf{VV}}^*\right)$ has to be checked for each pixel. However, the alternate decomposition schemes do not require to calculate the values of β and α and hence a large amount of the computational time is saved which makes a significant difference in the analysis of high resolution images.

6.5 Branching Conditions in Model-based Decomposition Methods

To further explore the impact of branching conditions in model-based decomposition methods, frequently used branching conditions are investigated. Since the solution of any model-based decomposition method is based on the branching condition, its reliability need to be checked. The frequently used branching conditions in model-based decomposition methods to discriminate between dominant surface and dihedral scattering mechanisms are listed below.

1. $\Re\left(S_{\mathrm{HH}}S_{\mathrm{VV}}^{*}\right)$ or $T_{11}-T_{22}$ [33]- [35], [74]- [75].
2. $T_{11}(\theta)-T_{22}(\theta)-T_{33}(\theta)+P_{\mathrm{c}}$ or $2T_{11}-TP+P_{\mathrm{c}}$ [85], [106], [108].

The term $T_{\mathrm{ij}}(\theta)$, $(\mathrm{i},\mathrm{j})=\{1,2,3\}$, denotes the elements of orientation angle compensated coherency matrix, TP denotes *span* or total power, and P_{c} stands for helix scattering power [106]. The following subsections investigated the factors responsible for breakdown of the aforementioned branching conditions.

6.5.1 Branching Condition 1: $T_{11}-T_{22}$

As mentioned in Section 1.12, the condition $T_{11}-T_{22}>0$ reflects dominant surface scattering mechanism. However, this condition may violate in the surface areas having some slopes. Sloped surfaces introduce cross-polarization in the scattering vector [2]. In addition, dihedral scattering can also be found in sloped areas through double reflection of the wave by the combination of plane surface and sloped surface. The same is true for the water bodies having disturbances at their surfaces due to wind as in the case of ocean and sea waves. The presence of double-bounce component (T_{22}) in the backscattering strengthens the violation of the condition $T_{11}-T_{22}>0$ in surface scattering areas.

On the other hand, condition $T_{11}-T_{22}\leq 0$ reflects dominant dihedral or double-bounce scattering. Urban area is the best example where this type of scattering takes place. However, this condition is violated in the presence of sloped and orientated man-made structures. With the presence of slope, the radar backscatter wave no longer includes two specular reflections from horizontal and vertical surfaces. Hence, the return may scattered into a small bistatic angle. As a consequence, the dihedral return is attenuated and can leave only the direct surface component in the radar backscatter direction [2]. The condition becomes more severe, when dihedral structures have large orientation with respect to radar illumination. Oriented dihedral structures generate a significant amount of cross-polarization power. The aforementioned factors attenuated the double-bounce component

in the radar backscattering, hence result in the violation of the condition $T_{11} - T_{22} \leq 0$ in sloped and oriented urban areas.

6.5.2 Branching Condition 2: $2T_{11} - TP + P_c$

The condition $2T_{11} - TP + P_c > 0$ reflects dominant surface scattering, whereas $2T_{11} - TP + P_c \leq 0$ reflects dominant dihedral scattering [106]. This branching condition is a modified version of $\Re\left(S_{HH}S_{VV}^{*}\right)$ on the coherency matrix elements after the introduction of helix scattering component and OAC technique. Here, one can see that the elements used for this branching condition are all roll-invariant. However, this branching condition is still not much efficient in complex oriented urban areas. It has been discussed in the previous subsection that in sloped urban areas, the radar backscatter may have dominant surface component. Also, complex man-made structures transform the incoming linear polarization into circular polarization which finally contributed to the helix scattering (P_c) power. These circumstances may lead to a situation where $2T_{11} + P_c > TP$ and therefore, violates the condition $2T_{11} - TP + P_c \leq 0$ in complex oriented urban areas [135].

6.6 Branching Condition Based on Alpha ($\overline{\alpha}$) Angle

In the previous section, it has been observed that the presence of slope and orientation affect the performance of conventional branching condition $T_{11} - T_{22}$. Later on, the conventional branching condition is suitably modified as $T_{11} - T_{22} - T_{33} + P_c$. Although this branching condition has roll-invariance property, its efficiency still lacks. The reason for this is the dependency of $T_{11} - T_{22} - T_{33} + P_c$ on many independent elements. The variation in a single element among T_{11}, T_{22}, T_{33}, and P_c, can affect the overall performance of the branching condition. Therefore, along with roll-invariance property, the independent elements in a branching condition should be as minimum as possible. The condition would be best if only one roll-invariant element is utilized to fulfil this purpose. Considering these aspects, alpha ($\overline{\alpha}$) angle can be explored to be used as a branching condition.

Parameter $\overline{\alpha}$ angle can be derived from the eigenvector decomposition of the coherency matrix as described in Section 1.10.3. It is robust to most of the factors affecting the performance of existing branching conditions. It is invariant to the rotations in the plane of polarization. Such rotations can appear in the backscattering from sloped surfaces and oriented urban areas [2]. In recent years, many coherency matrix transformations are proposed to compensate the effects of orientation of the scatterer as well as to efficiently exploit the information content of the coherency matrix. OAC [102], double-unitary transformation [108], and adaptive unitary transformation [109] are the

best examples of these transformations. However, any of these transformations applied to the coherency matrix are unitary in nature. Therefore, for any transformed pixel, $\overline{\alpha}$ angle remains unchanged. This roll-invariant property of $\overline{\alpha}$ angle fits the requirement of orientation independent [79], which makes it suitable to be worked even for distributed targets with random slopes and orientations. Therefore, it is more preferable to use $\overline{\alpha}$ angle to discriminate between dominant surface and dihedral scattering mechanisms in model-based methods.

6.6.1 Deciding the boundary of $\overline{\alpha}$ angle

The range of $\overline{\alpha}$ angle lies between 0° and 90°. The two extreme cases correspond to surface scattering from geometrical optics ($\overline{\alpha} = 0^\circ$) and dihedral scattering from metallic surfaces ($\overline{\alpha} = 90^\circ$). The median of these values, i.e. $\overline{\alpha} = 45^\circ$ can be found in the area of dipole scattering or single scattering by the cloud of anisotropic particles. At this stage, $\overline{\alpha}$ angle can be considered as a mixture of two orthogonal states $\overline{\alpha} = 0^\circ$ and $\overline{\alpha} = 90^\circ$. Therefore, the boundary for $\overline{\alpha}$ angle to discriminate between the dominant surface and dihedral scattering mechanisms is fixed at 45°. The pixels having $\overline{\alpha} \leq 45^\circ$ are considered to fall under dominant surface scattering mechanism, whereas the pixels having $\overline{\alpha} > 45^\circ$ are considered to fall under the dominant dihedral scattering mechanism.

6.7 Results and Discussions

This section experimentally validated the proposal of using $\overline{\alpha}$ angle as the branching condition in model-based decomposition methods. For that, experiments on three different PolSAR datasets are conducted to strongly emphasize our proposal and to show the significant improvement in the performances of model-based methods by replacing their original branching conditions with the branching condition based on $\overline{\alpha}$ angle. The first dataset used for the experiment is of San Francisco bay area obtained by C-band Radarsat-2 spaceborne satellite, whereas the second and third datasets are acquired over Hayward [132] and Niigata areas [127] by L-band UAVSAR and PiSAR airborne sensors, respectively. The Pauli RGB images of all three test sites are shown in Figure 6.2. All the aforementioned Pauli RGB images are marked with patches selected from different land-covers. The expressions of different branching conditions used for experimental analysis are listed below.

1. $\mathrm{C}_1 : T_{11} - T_{22}$
2. $\mathrm{C}_2 : 2T_{11} - TP - P_\mathrm{c}$

3. $C_3 : \overline{\alpha}$ angle

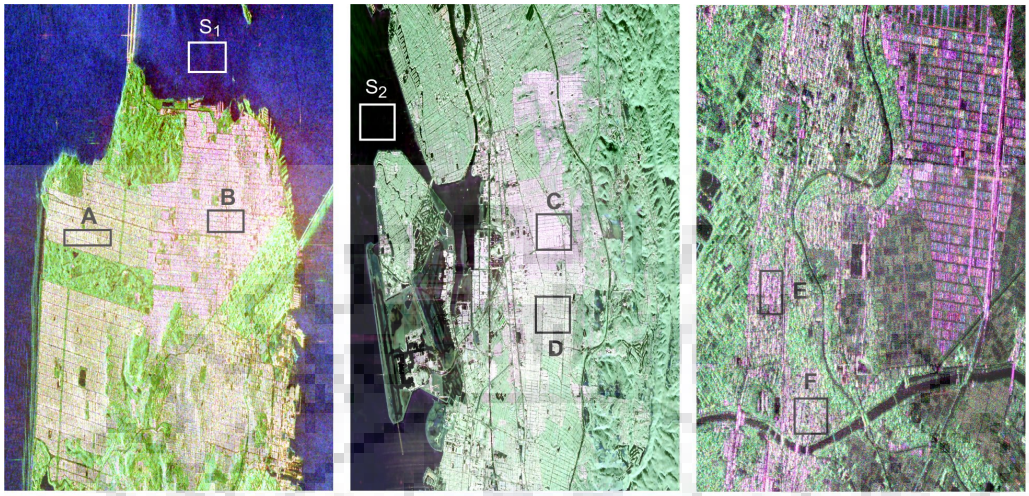

Figure 6.2: Pauli RGB images. (a) Radarsat-2 San Francisco area. (b) UAVSAR Hayward area. (c) PiSAR Niigata area.

Experiments on Different Urban Patches

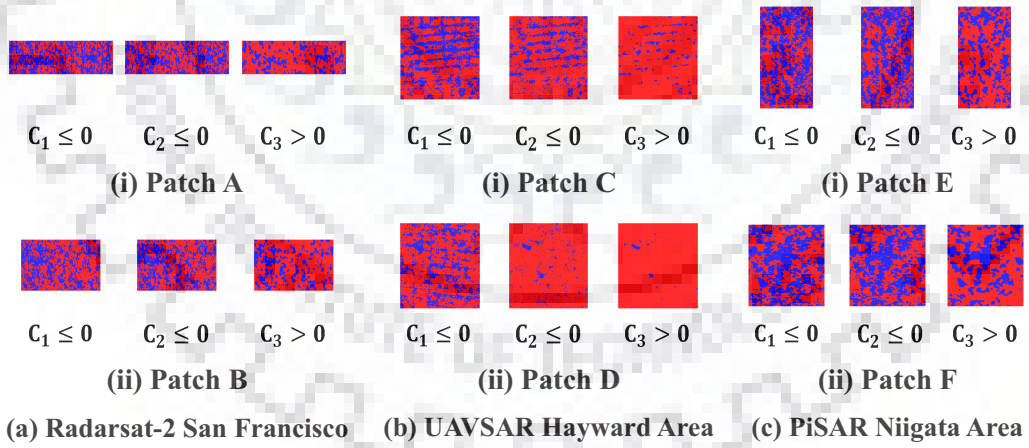

Figure 6.3: Urban pixels satisfying the different branching conditions for dominant dihedral scattering (Red color: Urban Pixels satisfying the dominant dihedral scattering condition, Blue color: Urban pixels violating the dominant dihedral scattering condition).

In this subsection, experiments are conducted over urban areas of different test sites. For that, different urban patches are selected from each of the three test sites as shown in Figure 6.2. Before conducting the experiments, J. S. Lee's sigma filter [136] is applied to the measured coherency matrix elements to suppress the inherent speckle noise. In addition,

$\overline{\alpha}$ angle is averaged over 3×3 window to mitigate any estimation bias. In the experiments, first part of the analysis starts with the calculation of percentage of pixels satisfying aforementioned expressions as branching conditions for dominant dihedral scattering mechanism: $C_1 \leq 0$, $C_2 \leq 0$, and $C_3 > 45^\circ$. Performances of the different branching conditions for selected urban patches A-F, O, and P are shown in Figure 6.3. However, for proper differentiation, a comprehensive quantitative comparison is described in Table 6.2. From the statistics given in Table 6.2, one can see that the percentage of urban pixels satisfying the branching condition $C_3 > 45^\circ$ is higher in comparison to other two branching conditions $C_1 \leq 0$ and $C_2 \leq 0$ for each of the selected urban patches.

Table 6.2: Percentage (%) of pixels satisfying different dominant dihedral branching conditions for selected urban patches

PolSAR Data	Patches	$C_1 \leq 0$	$C_2 \leq 0$	$C_3 > 45^\circ$
Radarsat-2 (San Francisco)	A	51.66	54.71	71.99
	B	59.31	58.48	72.89
	O	32.52	61.52	81.54
UAVSAR (Hayward)	C	62.03	75.29	92.89
	D	70.36	93.90	98.99
	P	9.05	79.54	95.87
PiSAR (Niigata)	E	52.04	51.01	66.20
	F	52.40	51.37	66.21

From Table 6.2, one can observe, though the branching condition C_2 has roll-invariance property, it is not always better than the branching condition C_1. To investigate the reason, the expression of C_2 can be rewritten in terms of C_1 as

$$C_2 = C_1 + (P_c - T_{33}). \tag{6.18}$$

In the above expression, one can notice that the factor responsible for difference in the performances of C_1 and C_2 is $(P_c - T_{33})$. In oriented urban areas, radar backscattering contains high cross-polarization power (T_{33}) which makes the difference term $(P_c - T_{33})$ negative for majority of the pixels. The negative difference term works in the favor of the condition $C_2 \leq 0$. That is why the performance of C_2 is better than C_1 in oriented urban areas. However, in aligned or less oriented urban areas where P_c dominates T_{33}, the difference term $(P_c - T_{33})$ moves toward positive value. This degraded the performance of branching condition $C_2 \leq 0$ in comparison to $C_1 \leq 0$ as can be seen for urban patches B, E, and F.

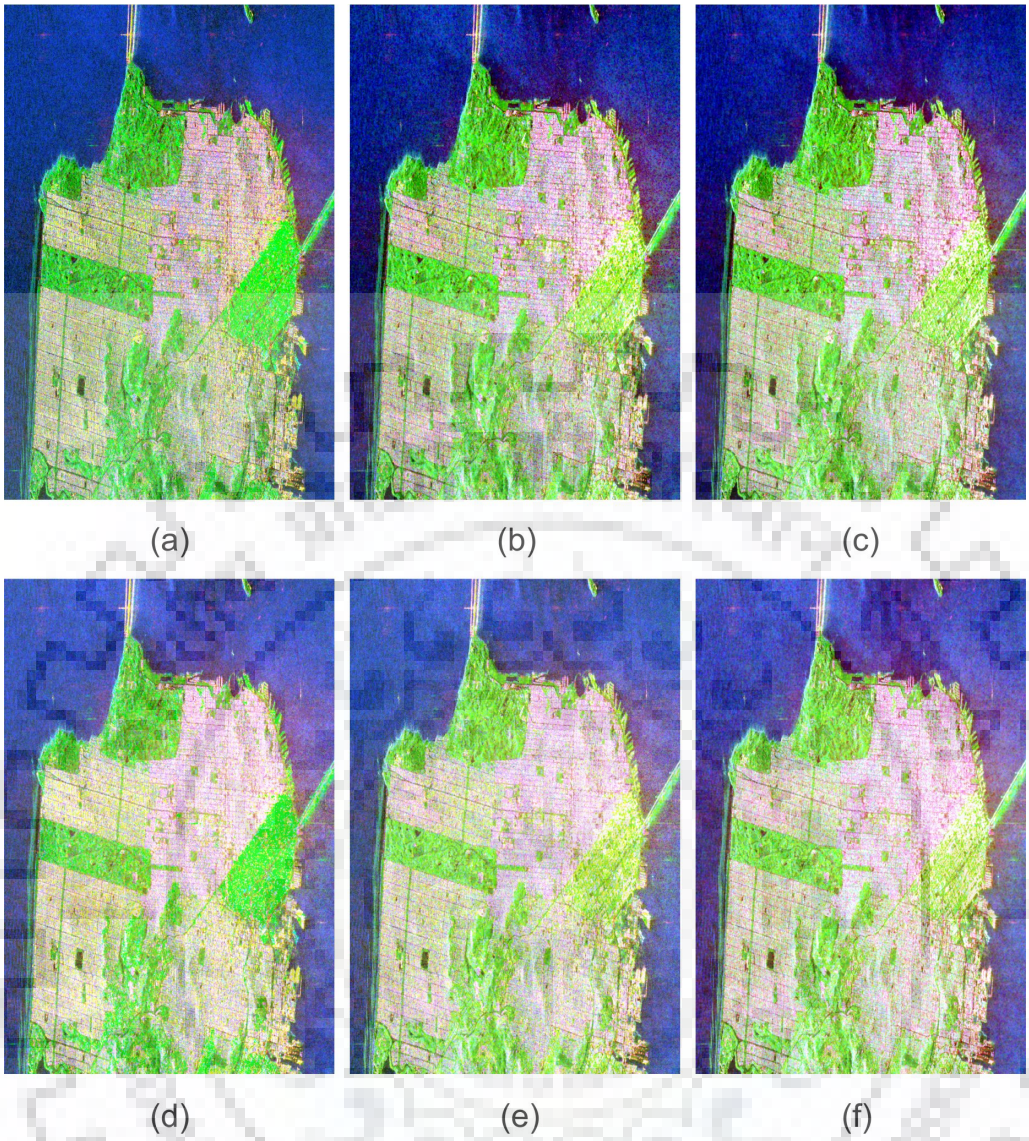

Figure 6.4: Color coded decomposed images of Radarsat-2 San Francisco area. (a)-(c) Y4O, Y4R, G4U, respectively with original branching conditions. (d)-(f) Y4O, Y4R, G4U, respectively with branching condition C_3.

6.7.1 Radarsat-2 San Francisco Bay Data

The next part of the analysis deals with the evaluation of the performances of some model-based decomposition methods with the new branching condition C_3. The model-based decomposition methods used for the demonstration are Y4O [74], Y4R [106], and G4U [108]. Y4O utilized C_1 as branching condition, whereas C_2 is used by Y4R and G4U. The color coded decomposed images of Radarsat-2 San Francisco area by Y4O, Y4R, and G4U with their original and the new branching conditions are shown in Figure 6.4. Figures. 6.4(a)-(c) show the decomposed images of Y4O, Y4R, and G4U, respectively with their original branching conditions, whereas Figures 6.4(d)-(f) show the de-

composed images of Y4O, Y4R, and G4U, respectively with the new branching condition C_3. For quantitative analysis, the normalized mean of double-bounce scattering power (P_d) is computed for each of the selected urban patches by aforementioned model-based methods with their original branching conditions and the new branching condition C_3. The two sets of the decomposition results are then compared as shown in Table 6.3.

Table 6.3: Means of normalized P_d (in %) over selected urban patches of Radarsat-2 San Francisco image

Methods	Patch A		Patch B		Patch O	
	Mean ($P_d/Span$)		Mean ($P_d/Span$)		Mean ($P_d/Span$)	
	O.B.C.*	C_3	O.B.C.*	C_3	O.B.C.*	C_3
Y4O	39.31	44.70	48.70	51.30	3.22	9.93
Y4R	46.21	50.72	50.20	53.34	28.32	35.04
G4U	47.00	52.06	50.80	54.19	31.43	37.73

(*O.B.C. stands for original branching conditions used for Y4O, Y4R, and G4U)

The statistics given in Table 6.3 describe the outcomes of the experiments conducted over the selected urban patches of San Francisco area as shown in Figure 6.2(a). From this table, one can examine the increment in the P_d values with the branching condition C_3. For all the model-based methods given in Table 6.3, P_d value is increased by about 5% in Patch A and 4% in Patch B. The Patch O is selected from the most oriented urban region (triangular area) of San Francisco. From Table 6.2, one can observe that the performance of branching condition $C_1 \leq 0$ is very poor for patch O. With branching condition $C_2 \leq 0$, improved result is achieved because of high T_{33} amplitude in the backscattering. However, the branching condition C_3 outperforms the other two with an accuracy of 81.54%. The roll-invariance property makes $\overline{\alpha}$ angle works well in this highly oriented urban patch. The performance of model-based methods for Patch O is tabulated in Table 6.3, where one can see the increment of 6% to 7% in the P_d values of different techniques with branching condition C_3.

6.7.2 UAVSAR Hayward Data

The next experiment is conducted over the selected urban patches of Hayward area as shown in Fig. 1(b). The decomposed images of UAVSAR Hayward area by Y4O, Y4R, and G4U with their original and the new branching conditions are shown in Figure 6.5. Figures 6.5(a)-(c) show the decomposed images of Y4O, Y4R, and G4U, respectively with their original branching conditions, whereas in Figures 6.5(d)-(f), decomposed images of Y4O, Y4R, and G4U, respectively are shown with branching condition C_3.

The increment in the performances of model-based decomposition methods can be seen from Table 6.4. From this table, one can observe that for all the urban patches of

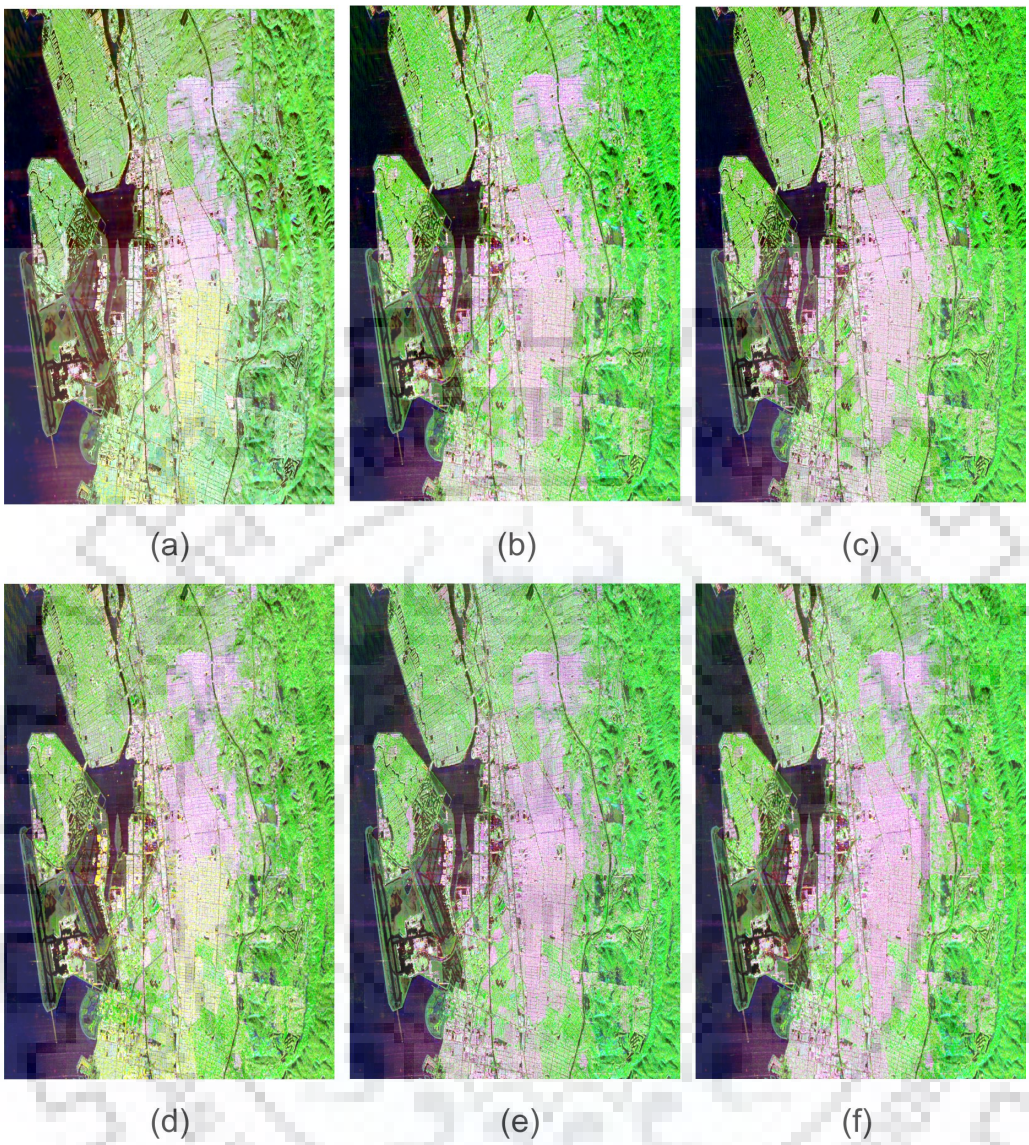

Figure 6.5: Color coded decomposed images of UAVSAR Hayward area. (a)-(c) Y4O, Y4R, G4U, respectively with original branching conditions. (d)-(f) Y4O, Y4R, G4U, respectively with branching condition C_3.

Table 6.4: Means of normalized P_d (in %) over selected urban patches of UAVSAR Hayward image

Methods	Patch C		Patch D		Patch P	
	Mean ($P_d/Span$)		Mean ($P_d/Span$)		Mean ($P_d/Span$)	
	O.B.C.	C_3	O.B.C.	C_3	O.B.C.	C_3
Y4O	47.49	54.80	42.57	45.80	17.30	25.04
Y4R	53.13	57.47	53.83	55.03	25.36	27.50
G4U	53.81	58.52	54.45	55.76	26.46	28.76

Hayward area, the increase in P_d values for Y4O is more than 3% with the branching condition C_3. However, the increase in P_d values is less for Y4R and G4U as compared to Y4O. This clearly reflects that the increase in the performances of model-based methods is proportional to the increase in percentage of pixels satisfying the branching condition C_3.

6.7.3 PiSAR Niigata Data

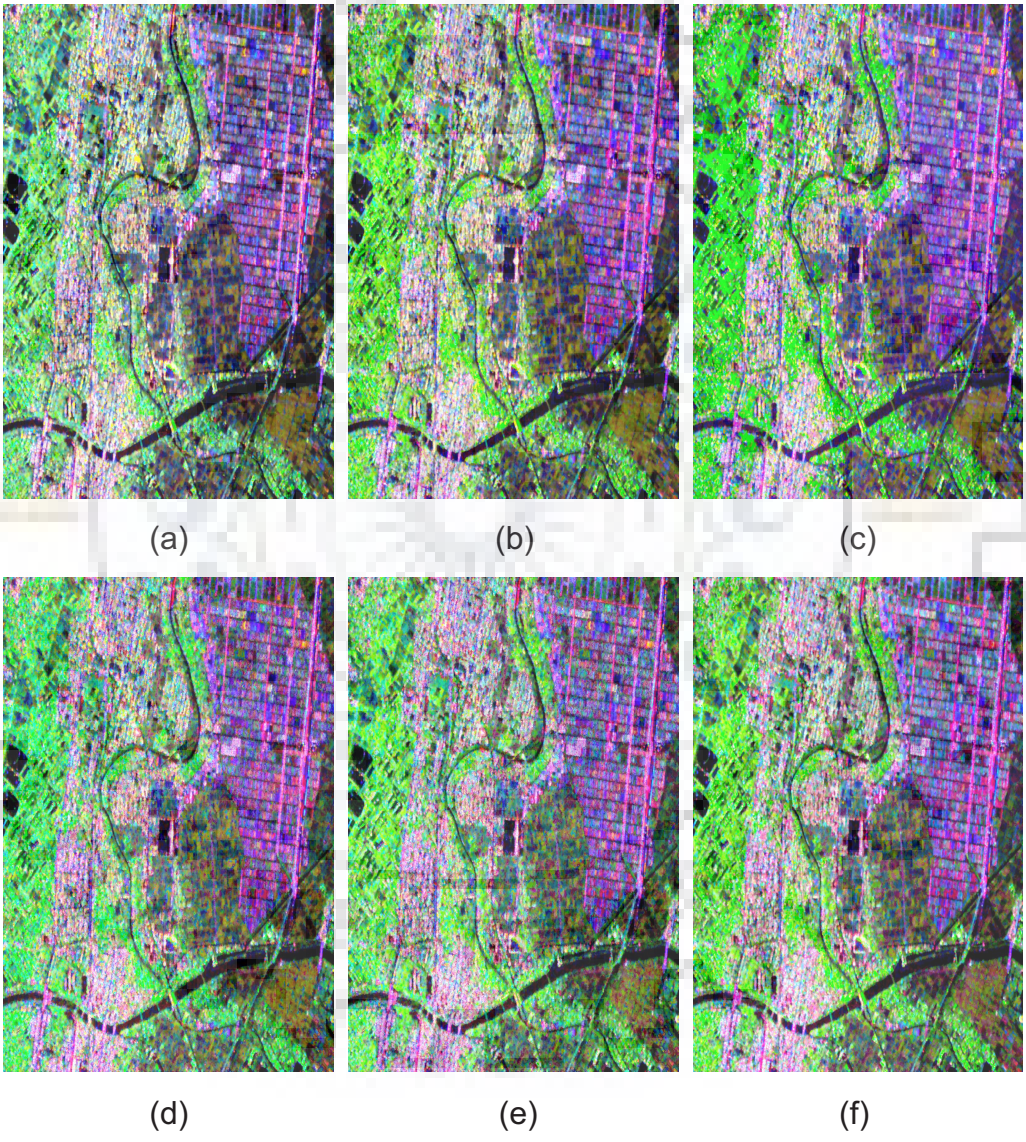

Figure 6.6: Color coded decomposed images of PiSAR Niigata area. (a)-(c) Y4O, Y4R, G4U, respectively with original branching conditions. (d)-(f) Y4O, Y4R, G4U, respectively with branching condition C_3.

The last experiment is carried over urban patches of Niigata area as shown in Figure 6.2(c). The decomposed images of PiSAR Niigata area by Y4O, Y4R, and G4U with

their original and the new branching conditions are shown in Figure 6.6. Figures 6.6(a)-(c) show the decomposed images of Y4O, Y4R, and G4U, respectively with their original branching conditions, whereas Figures 6.6(d)-(f) show the decomposed images of Y4O, Y4R, and G4U, respectively with the branching condition C_3.

Table 6.5: Means of normalized P_d (in %) over selected urban patches of PiSAR Niigata image

Methods	Patch E		Patch F	
	Mean ($P_d/Span$)		Mean ($P_d/Span$)	
	O.B.C.	C_3	O.B.C.	C_3
Y4O	41.95	48.95	42.88	49.94
Y4R	43.02	50.41	45.06	51.63
G4U	43.46	50.77	46.57	52.65

Again for these urban patches, the model-based methods perform better with the branching condition $C_3 > 45^\circ$ as compared to their original ones. From Table 6.5, it can be seen that in Patch E, normalized means of P_d increased by 7% for Y4O, while for Y4R and G4U, the increments are 7.39% and 7.31%, respectively. For Patch F, Y4O retains the same increment, whereas the increments in P_d for Y4R and G4U are about 6.5% and 6%, respectively. All these aforementioned experiments clearly demonstrate the advantage of using branching condition C_3 for model-based decomposition methods.

Experiments on Ocean Patches

The experiments over selected ocean patches of San Francisco and Hayward test site images (as shown in Figures 6.2(a) and 6.2(b)) are conducted to further validate the effectiveness of the branching condition C_3. Since ocean areas fall within the surface scattering category, the equality signs of branching conditions described in Section 6.4.1 are now just reversed as $C_1 > 0$, $C_2 > 0$, and $C_3 \leq 45^\circ$. First part of the analysis starts with the calculation of percentage of pixels satisfying different branching conditions.

Table 6.6: Percentage (%) of pixels satisfying different dominant surface scattering branching conditions for selected ocean patches

PolSAR Data	Patch	$C_1 > 0$	$C_2 > 0$	$C_3 \leq 45^\circ$
Radarsat-2 (San Francisco)	S_1	93.81	95.32	99.97
UAVSAR (Hayward)	S_2	93.20	91.41	97.55

From Table 6.6, one can observe that all branching conditions discriminated the ocean patches under dominant surface scattering mechanism with high accuracies. However,

the branching condition $C_3 \leq 45^\circ$ still dominated the rest of two branching conditions. In the next part of analysis, the normalized mean of surface scattering power (P_s) is computed for each of the selected ocean patches by different model-based methods. One can observe from Table 6.7 that the percentage of P_s is increased for different model-based schemes by utilizing branching condition C_3. From all these experiments and analyses, one can easily conclude that the model-based methods provide better results with the branching condition C_3 than the previous existing branching conditions.

Table 6.7: Means of normalized P_s (in %) over selected ocean patches of San Francisco and Hayward images

Methods	Patch S_1		Patch S_2	
	Mean ($P_s/Span$)		Mean ($P_s/Span$)	
	O.B.C.	C_3	O.B.C.	C_3
Y4O	90.30	92.23	72.23	73.32
Y4R	90.48	91.54	73.59	75.41
G4U	90.75	91.76	74.04	75.89

6.8 Conclusions

In this chapter, alternative approaches to the branching conditions of model-based decomposition methods are investigated. In the first part, a computationally efficient approach to solve the conventional model-based decomposition methods is proposed. Under this approach, the conventional branching condition is efficiently implemented by distributing the contribution of T_{12} element to single- and double-bounce scattering channels. With this, alternate FDD and Y4O decomposition schemes are presented. The alternate decomposition schemes have equal number of equations and unknowns. Hence, the values of unknowns can be found out directly without checking any branching condition which greatly improves the computational efficiency. In the second part, the impact of branching conditions in the performance of model-based decomposition methods is explored. The efficiencies of frequently used branching conditions are evaluated in terms of their ability to discriminate dominant surface and dihedral scattering areas. Along with this, a new branching condition based on $\overline{\alpha}$ angle is presented. The roll-invariance property of $\overline{\alpha}$ angle makes it robust to the factors affecting the efficacy of existing branching conditions. Experiments on different PolSAR datasets are conducted to evaluate the potency of $\overline{\alpha}$ angle as branching condition. The experimental results clearly demonstrated that the deficiency of existing branching conditions can be overcome by $\overline{\alpha}$ angle. Furthermore, analysis is extended to evaluate the performances of model-based methods with the branching condition based on $\overline{\alpha}$ angle. In these analyses, it is shown that the potency

of the model-based methods significantly increased by replacing their original branching conditions with $\overline{\alpha}$ angle.

Chapter 7

Conclusion and Future Scope

7.1 Contribution of the Thesis

In recent years, there has been fast and large scale change in different land-cover types like barren areas, vegetation, grasslands, landscapes, coastal areas, forest, urban, and wetlands etc. These changes are due to the increased human population and the ever-increasing demand of human for the natural resources. The rapid expansion of urban areas and change in population settlements contribute to the variations in weather and climatic conditions. Urbanization, which is the leading reason behind the depletion of vegetation and forests, ultimately results in the changes in hydrological conditions. The regional and global climatic conditions, both of them are affected by the displacement of natural vegetation cover and landscapes. Therefore, correct mapping of land-cover plays a significant role in understanding the global environmental variation. On this matter, over the past two decades, model-based decomposition methods have been used for land-cover mapping through the analysis of PolSAR data. However, despite of its usability, model-based decomposition methods suffer from some inherited problems. These problems confine the applicability of the model-based decomposition methods.

The work in this thesis aims at providing feasible solutions to the current problems of model-based decomposition methods. In Chapter 1, the four current challenges of model-based decomposition methods are pointed out. The probable solutions and advancements related to these challenges reported in the literature are discussed comprehensively in Chapter 2. Thereafter the main contributions of this thesis are described in the next four working chapters.

In Chapter 3, a new urban scattering model was proposed to deal with the scattering mechanism ambiguity between urban area and vegetation. Scattering from urban area is usually modeled with the co-polarization scattering phenomenon. However, man-made structures oriented away from the optimal radar illumination generate a significant amount

of cross-polarization power. Cross-polarization is generally accounted by the volume scattering mechanism. Hence oriented urban areas are wrongly classified into volume scattering category. To accommodate the cross-polarization scattering from urban area, coherency matrix of a rotated dihedral corner reflector was used. Cosine distribution with its peak at orientation angle was incorporated to average the rotated dihedral coherency matrix. Utilizing this averaged coherency matrix, an extended four-component decomposition (E4D) has been proposed. Consideration of orientation angle enables the modeling of one unused element of coherency matrix, i.e. the real part of T_{23}, which makes the decomposition scheme more feasible and effective.

Coherency matrix transformations through special unitary matrix SU(3) group was exploited in Chapter 4. Ideally, the measured coherency matrix should be completely deoriented to avoid any scattering mechanism ambiguity. However, it is almost impossible to completely extract the target orientation. That is why only the partial deorientation could be applied to fully polarimetric coherency matrix. To maximize the deorientation, influence of target orientation along with slope and tilt effects on coherency matrix should be minimized. To accomplish this, four special unitary SU(3) matrices were utilized to optimize the coherency matrix. In the optimization process, cross-polarization minimization has been addressed separately for sloped surfaces and oriented urban areas. By doing so, the reduced power from cross-polarization channel is always concentrated on the underlying dominant co-polar scattering mechanism. This makes it unique in comparison to state-of-the-art techniques. Along with minimizing cross-polarization power, new unitary rotations also transforms the coherency matrix more close to reflection symmetry condition by reducing the number of unused elements.

In Chapter 5, a hybrid decomposition technique has been presented to deal with the negative power problem of model-based decomposition methods. Overestimation of the volume scattering contribution is one of the major reason for having negative scattering power pixels in model-based decomposition methods. To deal with this problem, coherency matrix rotations proposed in Chapter 4 are used to remove maximal of the cross-polarization power generated by the coupling between orthogonal states of polarization. Whereas, with the utilization of hybrid scattering models, the complete removal of negative scattering powers has been achieved. The applicability of the proposed approach has been shown through the implementation of hybrid four-component decomposition method.

The significance of branching condition in model-based decomposition methods was discussed in Chapter 6. The first part of this chapter presented the new coherency matrix transformations to obtain the solution of an under-determined system of model-based methods without making any assumption. By this means, computationally efficient al-

ternate FDD and Y4O decomposition schemes were implemented. In the second part of this chapter, the performance of frequently used branching conditions in the model-based decomposition methods was investigated. In this part, it has been shown that the existing branching conditions are less efficient when it comes to discriminate in between dominant surface and dihedral scattering mechanisms. The discrimination ability of the branching conditions further deteriorates when the target has some random slope and orientation. This greatly affects the performance of the model-based decomposition methods. To alleviate this problem, a new branching condition based on the value of the α angle has been suggested. The roll-invariance property of α angle makes it work efficiently even in the sloped and oriented areas where existing branching conditions are less efficient. The replacement of the existing branching conditions with α angle enhanced the performances of the model-based decomposition methods.

7.2 Future Scope

The following aspects can be explored as the future scope of this thesis work.

1. This thesis mainly concerned on the scattering mechanism ambiguity problem of model-based decomposition methods. The most common scattering mechanism ambiguity in model-based decomposition methods is the result of incorrect categorization of the cross-polarization power generated by different depolarizing targets. The most likely solution to this problem is achieved by introducing new scattering models [137]- [145]. New models can lessen the scattering mechanism ambiguity either by better characterization of volume scattering from vegetation or by modeling the cross-polar response from tilted surface and oriented man-made areas. The second effective solution to resolve this issue is given by the unitary rotations of coherency matrix. Both of these methods are effective and widely used for model-based decomposition methods. However, in recent years, the unitary rotations of scattering models are explored. Scattering model rotations with known rotation angles have advantages over introducing new scattering models as they do not increase the number of unknowns in the decomposition scheme. These rotated scattering models, known as generalized or incoherent scattering models, account for the incoherently scattering from depolarizing targets. In few literature, incoherent scattering models are used along with the unitary rotation of coherency matrix. However, if the coherency matrix is compensated for slope and orientation of the scatterers, then the scattering models do not need further rotation with the same rotation angle as the effect has been already compensated. In this case, the scattering

models should be kept as conventional. On the other hand, if the scattering models are rotated, then the coherency matrix should remain as original. Nevertheless, the aforementioned two statements can be implemented simultaneously if two different rotation matrices with different rotation angles are used to rotate coherency matrix and scattering models separately. This scheme is expected to enhance the decomposition result by integrating more information in a decomposition scheme.

2. Chapter 4 of this thesis described the effectiveness of selective unitary rotations of coherency matrix based on the dominant scattering mechanism. Removal of cross-polarization power generated from different depolarization targets, and assigning the removed cross-polarization power back to the underlying dominant co-polar scattering component was the key idea of this work. The adaptability to the work is provided by utilizing different special unitary rotation matrices with different rotation angles. However, this adaptability completely depends on the effectiveness of the branching condition. The branching condition is used to determine the underlying dominant co-polar scattering mechanism, and accordingly the depolarizing targets are assumed to fall under that dominant category. As can be seen from Chapter 6, conventional branching conditions are less efficient in deciding the dominant scattering mechanism. Therefore, this can lead to the wrong selection of unitary rotation matrix. Subsequently, this will raise the scattering mechanism ambiguity by assigning the removed cross-polarization power to wrong co-polarization component. To resolve this problem, the branching condition based on α angle can be utilized for the appropriate selection of the unitary rotation matrix. This will increase the potency of the model-based methods in two ways. First, replacement of conventional branching condition with α angle will itself enhance the decomposition efficiency. Second, the more accurate selection of unitary rotation will reduce more cross-polarization power and empowers the correct dominant co-polarization scattering mechanism.

3. In this thesis, the importance of volume scattering matrix in model-based decomposition scheme is discussed thoroughly. Almost all the model-based decomposition techniques compute the surface and dihedral scattering powers after subtracting the volume scattering contribution from the measured coherency matrix. That's the reason why most of the major problems of model-based decomposition methods arise due to inappropriateness of the volume scattering matrix. The literature related to volume scattering matrix is vast [33], [74]- [75], [87]- [91]. Many appreciable improvements in model-based decomposition category are presented by proper modeling of volume scattering mechanism [146]- [150]. However, still the

overestimation of volume scattering power and its after-effects are regarded as the major challenges of model-based decomposition. Basically, the cross-polarization phenomenon is considered as the result of volume scattering. However, apart from vegetation, many real scenarios are there where the backscattering carries cross-polarization power. Therefore, instead of allocating the entire cross-polarization power, only a part of it should relate to the volume scattering. On this issue, the approach of eigen-based decomposition techniques looks more approved and convenient. In eigen-based decomposition techniques, polarization/depolarization contents (entropy, polarization fraction, depolarization index, degree of polarization etc.) are frequently considered to measure the noise, random scattering, and volume scattering contribution. These parameters are derived from the eigenvalues of coherency matrix, therefore has roll-invariance property. Thus assimilating this information in modeling of volume scattering phenomenon is expected to mitigate the overestimation of volume scattering and its consequences in model-based techniques.

Bibliography

[1] J. S. Lee and E. Pottier, *Polarimetric radar imaging: from basics to applications*. Boca Raton, FL, USA: CRC, 2009.

[2] S. R. Cloude, *Polarisation: applications in remote sensing*. London, U.K. Oxford Univ. Press, 2010.

[3] M. A. Richards, *Fundamental of radar signal processing*. McGraw-Hill. 2005.

[4] H. Mott, *Remote sensing with polarimetric radar*. Wiley, 2007.

[5] J. J. Van Zyl and Y. Kim, *Synthetic aperture radar polarimetry*. Wiley, 2011.

[6] Y. Yamaguchi, "Disaster monitoring by fully polarimetric SAR data acquired with ALOS-PoLSAR, *Proc. IEEE*, vol. 100, pp. 2851–2860, 2012.

[7] M. Sato, S.-W. Chen, and M. Satake, "Polarimetric SAR analysis of tsunami damage following the March 11, 2011 East Japan earthquake", *Proc. IEEE*, vol. 100, pp. 2861–2875, 2012.

[8] S.-W. Chen and M. Sato, "Tsunami damage investigation of built-up areas using multitemporal spaceborne full polarimetric SAR images", *IEEE Transactions on Geoscience and Remote Sensing*, vol. 51, pp. 1985–1997, 2013.

[9] G. Singh, Y. Yamaguchi, W.-M. Boerner, and S.E. Park, "Monitoring of the March 11, 2011, off-Tohoku 9.0 Earthquake with super-tsunami disaster by implementing fully polarimetric high resolution POLSAR techniques", *Proc. IEEE*, vol. 101, pp. 831–846, 2013.

[10] K. E. Joyce, S. V. Samsonov, S. R. Levick, J. Engelbrecht, and S. Belliss," "Mapping and monitoring geological hazards using optical, LiDAR, and synthetic aperture RADAR image data," *Natural hazards*, vol. 73, pp. 137–163, 2014.

[11] L. A. Gibson, Z. Münch, J. Engelbrecht, and J. E. Conrad, "Uncertainties in using remote sensing for water use determination: a case study in a heterogeneous study

area in South Africa," *Hydrology and Earth System Sciences Discussions*, vol. 7, pp. 6581–6612, 2016.

[12] V. P. A. Rebello, A. Getirana, V. Lakshmi, and O. C. R. Filho, "Monitoring drought in Brazil by remote sensing," *Remote Sensing of Hydrological Extremes*, pp. 197-218, 2017.

[13] R. Albarakat, V. Lakshmi, and C. Tucker, "Using satellite remote sensing to study the impact of climate and anthropogenic changes in the Mesopotamian Marshlands, Iraq," *Remote Sensing*, vol. 10, 2018.

[14] A. Theron, J. Engelbrecht, "The role of earth observation, with a focus on SAR interferometry, for sinkhole hazard assessment," *Remote Sensing*, vol. 10, 2018.

[15] A. Moreira, P. Prats-Iraola, M. Younis, G. Krieger, I. Hajnsek, and K. P. Papathanassiou, "A tutorial on synthetic aperture radar," *IEEE Geoscience and Remote Sensing Magazine*, vol. 1, pp. 6–43, 2013.

[16] S. Chandrasekhar, *Radiative transfer*. New York, Dover Publications Inc, 1960.

[17] J. R. Huynen, "Phenomenological theory of radar targets," Ph.D. dissertation, Dept. Electr. Eng., Math. Comput. Sci., Technical Univ., Delft, The Netherlands, 1970.

[18] E. Krogager, "A new decomposition of the radar target scattering matrix," *Electronics Letters*, vol. 26, pp. 1525–1526, 1990.

[19] E. Krogager, and W.-M. Boerner, "On the importance of utilizing polarimetric information in radar imaging classification," *AGARD Proc.*, pp. 1–13, 1996.

[20] W. L. Cameron, N. Youssef, and L. K. Leung, "Simulated polarimetric signatures of primitive geometrical shapes," *IEEE Transactions on Geoscience and Remote Sensing*, vol. 34, pp. 793–803, 1996.

[21] D. G. Corr, and A. F. Rodrigues, "Alternative basis matrices for polarimetric decomposition," *Proceedings of EUSAR*, Cologne, Germany, 2002.

[22] R. Touzi, and F. Charbonneau, "Characterization of target symmetric scattering using polarimetric SARs," *IEEE Transactions on Geoscience and Remote Sensing*, vol. 40, pp. 2507–2516, 2002.

[23] G. Singh, "Development of general radar polarimetry methods for fully polarimetric synthetic aperture radar data utilization to monitor the Earth," Doctoral Thesis, Program in Electrical and Information Engineering, Graduate School of Science and Technology, Niigata University, Niigata-shi, Japan, 2013.

[24] S. R. Cloude, "Uniqueness of target decomposition theorems in radar polarimetry in Direct and Inverse Methods in Radar Polarimetry," *Part 1, NATO-ARW*, W.M. Boemer et al., (Eds.) Norwell, MA: Kluwer, pp. 267–296, 1992.

[25] S .R. Cloude and E. Pottier, "The concept of polarization entropy in optical scattering," *Optical Engineering*, vol. 34, pp. 1599–1610, 1995.

[26] S. R. Cloude and E. Pottier, "A review of target decomposition theorems in radar polarimetry," *IEEE Transactions on Geoscience and Remote Sensing*, vol. 34, no. 2, pp. 498-518, Mar. 1996.

[27] S. R. Cloude and E. Pottier, "An Entropy based classification scheme for land applications of polarimetric SAR," *IEEE Transactions on Geoscience and Remote Sensing*, vol. 35, no. 1, pp. 68–78, 1997.

[28] S. L. Durden, J. J. van Zyl, and H. A. Zebker, "The unpolarized component in polarimetric radar observations of forested areas," *IEEE Transactions on Geoscience and Remote Sensing*, vol. 28, pp. 268–271, 1990.

[29] S. Wang, K. Liu, J. Pei, M. Gong, and Y. Liu, "Unsupervised classification of fully polarimetric SAR images based on scattering power entropy and copolarized Ratio," *IEEE Geoscience and Remote Sensing Letters*, vol. 10, pp. 622–626, 2013.

[30] S. Zhang, S. Wang, B. Chen, and S. Mao, "Classification method for fully PolSAR data based on three novel parameters," *IEEE Geoscience and Remote Sensing Letters*, vol. 11, pp. 39–43, 2014.

[31] W. An, Y. Cui, J. Yang, and H. Zhang, "Fast alternatives to H/alpha for polarimetric SAR," *IEEE Geoscience and Remote Sensing Letters*, vol. 7, pp. 343–347, 2010.

[32] A. Freeman and S. Durden, "A three component scattering model to describe polarimetric SAR data," *Radar Polarimetry*, vol. SPIE- 1748, pp. 213–225, 1992.

[33] A. Freeman and S. L. Durden, "A three-component scattering model for polarimetric SAR data," *IEEE Transactions on Geoscience and Remote Sensing*, vol. 36, no. 3, pp. 963-973, May 1998.

[34] J. J. van Zyl, "Unsupervised classification of scattering behavior using radar polarimetry data," *IEEE Transactions on Geoscience and Remote Sensing*, vol. 27, pp. 36-45, Jan. 1989.

[35] J.-S. Lee, T. L. Ainsworth, and Y. Wang, "Generalized polarimetric model-based decompositions using incoherent scattering models," *IEEE Transactions on Geoscience and Remote Sensing*, vol. 52, no. 5, pp. 2474-2491, 2014.

[36] P. Siqueira, S. Hensley, B. Chapman, and R. Ahmed, "Combining lidar and InSAR observations over the Harvard and Duke forests for making wide area maps of vegetation height," *IGARSS*, 2008.

[37] R. Ahmed, P. Siqueira, and S. Hensley," "Analyzing the uncertainty of biomass estimates from L-band radar backscatter over the Harvard and Howland forests," *IEEE Transactions on Geoscience and Remote Sensing*, vol. 52, pp. 3568–3586, 2014.

[38] Y. Lei, P. Siqueira, N. Torbick, D. Chowdhury, W. Salas, and R. N. Treuhaft, "Large-scale product of forest height using a new approach from spacborne repeat-pass SAR interferometry and lidar," *IGARSS*, 2017.

[39] O. Cartus, P. Siqueira, and J. Kellndorfer, "An error model for mapping forest cover and forest cover change using L-band SAR", *IEEE Geoscience and Remote Sensing Letters*, vol. 15, pp. 107–111, 2018.

[40] Y. Lei, R. M. Lucas, P. Siqueira, M. Schmidt, and R. N. Treuhaft," "Detection of forest disturbance with spaceborne repeat-pass SAR interferometry," *IEEE Transactions on Geoscience and Remote Sensing*, vol. 56, pp. 2424–2439, 2018

[41] G. Ijjas and Y.S. Rao, "Microwave remote sensing of soil moisture from aircraft in Hungary", *International Journal of Remote Sensing*, vol. 13, pp. 471–479, 1992.

[42] J. D. Bolten, V. Lakshmi, E. G. Njoku, "Soil moisture retrieval using the passive/active L-and S-band radar/radiometer," *IEEE Transactions on Geoscience and Remote Sensing*, vol. 41, pp. 2792-2801, 2003.

[43] J. Engelbrecht, "Synthetic aperture radar data employed for soil moisture estimation in the Piketberg region, South Africa," *IGARSS*, 2009.

[44] S. Mohan, A. Das, D. Haldar, and S. Maity, "Monitoring and retrieval of vegetation parameter using multi-frequency polarimetric SAR data," *3rd International Asia-Pacific Synthetic Aperture Radar (APSAR)*, 2011.

[45] G. G. Ponnurangam and Y.S. Rao, "Soil moisture mapping using ALOS PALSAR and ENVISAT ASAR data over India", *Proc. Asia-Pacific conference on SAR*, pp. 606–609, 2011.

[46] D. Haldar, A. Das, S. Mohan, O. Pal, R. S. Hooda, and M. Chakraborty, "Assessment of L-band SAR data at different polarization combinations for crop and other land use classification," *Progress In Electromagnetics Research*, vol. 36, pp. 303–321, 2012.

[47] U. K. Khankhoje, M. Burgin, and M. Moghaddam, "On the accuracy of averaging radar backscattering coefficients for bare soils using the finite element method," *IEEE Geoscience and Remote Sensing Letters*, vol. 11, pp. 1345–1349, 2014.

[48] J. Engelbrecht, C. Musekiwa, J. Kemp, M. R. Inggs, "Parameters affecting interferometric coherence – The case of a dynamic agricultural region," *IEEE transactions on geoscience and remote sensing*, vol. 52, pp. 1572–1582, 2014.

[49] D. Haldar, A. Das, M. Yadav, R. S. Hooda, S. Mohan, and M. Chakraborty, "Analysis of temporal polarization phase difference for major crops in India," *Progress In Electromagnetics Research*, vol. 57, pp. 299–309, 2014.

[50] P. W. Liu, J. Judge, R. D. DeRoo, A. W. England, T. Bongiovanni, and A. Luke, "Dominant backscattering mechanisms at L-band during dynamic soil moisture conditions for sandy soils," *Remote Sensing of Environment*, vol. 178, pp. 104-112, 2016.

[51] P. W. Liu, T. Bongiovanni, A. Monsivais-Huertero, J. Judge, S. Steele-Dunne, R. Bindlish, and T. J. Jackson, "Assimilation of active and passive microwave observations for improved estimates of soil moisture and crop growth," *IEEE Journal of Selected Topics in Applied Earth Observations and Remote Sensing*, vol. 9, pp. 1357–1369, 2016.

[52] U. K. Khankhoje, "Quantification of Uncertainty in Radar Backscatter Due to Variable Soil Moisture," *PIERS*, Singapore, 2017.

[53] V. Kumar, H. McNairn, A. Bhattacharya, and Y. S. Rao, "Temporal response of crop type to transmitted ellipticity in compact-pol SAR data", *IEEE Journal of Selected Topics in Applied Earth Observations and Remote Sensing*, 2017.

[54] S. C. Steele-Dunne, H. McNairn, A. Monsivais-Huertero, J. Judge, P. W. Liu, and K. Papathanassiou, "Radar remote sensing of agricultural canopies: A review," *IEEE Journal of Selected Topics in Applied Earth Observations and Remote Sensing*, vol. 10, pp. 2249–2273, 2017.

[55] H. Wang, R. Magagi, and K. Goita, "Comparison of different polarimetric decompositions for soil moisture retrieval over vegetation covered agricultural area," *Remote Sensing of Enironment*, vo. 199, pp. 120–136, 2017.

[56] Y. S. Rao, "Synthetic aperture radar (SAR) interferometry for glacier movement studies", *Encyclopedia of snow, ice and glaciers, Springer*, pp.1133–1142, 2011.

[57] G. Singh, G. Venkataraman, Y. Yamaguchi, and S.-E. Park, "Capability assessment of fully polarimetric ALOS PALSAR data to discriminate wet snow from other targets", *IEEE Transactions on Geoscience and Remote Sensing*, vol. 52, pp. 1177–1196, 2014.

[58] S.-E. Park, Y. Yamaguchi, G. Singh, S. Yamaguchi, and A. C. Whitaker, "Polarimetric SAR response of snow covered area observed by multi-temporal ALOS-PALSAR fully-polarimetric mode", *IEEE Transactions on Geoscience and Remote Sensing*, vol. 52, pp. 329–340, 2014.

[59] N. Usami, A. Muhuri, A. Bhattacharya, and A. Hirose, "PolSAR wet snow mapping with incident angle information", *IEEE Geoscience and Remote Sensing Letters*, vol. 13, pp. 2029–2033, 2016.

[60] A. Muhuri, D. Ratha, and A. Bhattacharya, "Seasonal snow cover change detection over the Indian Himalayas using polarimetric SAR images", *IEEE Geoscience and Remote Sensing Letters*, vol. 14, pp. 2340–2344, 2017.

[61] A. Muhuri, M. Surendar, and A. Bhattacharya, "Scattering mechanism based snow cover mapping using RADARSAT-2 C-band polarimetric SAR data", *IEEE Journal of Selected Topics in Applied Earth Observations and Remote Sensing*, vol. 10, pp. 3213–3224, 2017.

[62] M. Surendar, A. Bhattacharya, G. Singh, Y. Yamaguchi, "Estimation of snow surface dielectric constant from polarimetric SAR data", *IEEE Journal of Selected Topics in Applied Earth Observations and Remote Sensing*, vol. 10, pp. 211–218, 2017.

[63] S. Nayak, A. Bahuguna, P. Chauhan, H. B. Chauhan, and R. S. Rao, "Remote sensing applications for coastal environmental management in India," *Environmental Management*, vol. 4, pp. 113–125, 1997.

[64] P. Chauhan, M. Mohan, R. K. Sarngi, B. Kumari, S. Nayak, and S. G. P. Matondkar, "Surface chlorophyll a estimation in the Arabian sea using IRS-P4 ocean colour

monitor (OCM) satellite data," *International Journal of Remote Sensing*, vol. 23, pp. 1663–1676, 2002.

[65] D.L. Schuler, J.S. Lee, D. Kasilingam, and E. Pottier, "Measurement of ocean surface slopes and wave spectra using polarimetric SAR image data," *Remote Sensing of Environment*, vol. 91, pp. 198– 211, 2004.

[66] P. N. Vinayachandran, P. Chauhan, M. Mohan, and S. Nayak, "Biological response of the sea around Sri Lanka to summer monsoon," *Geophysical Research Letters*, vol. 31, 2004.

[67] R. K. Sarangi, M. K. Mishra, and P. Chauhan, "Remote sensing observations on impact of Phailin cyclone on phytoplankton distribution in northern Bay of Bengal," *IEEE Journal of selected topics in Applied Earth Observations and Remote Sensing*, vol. 8, pp. 539–549, 2015.

[68] M. Sugimoto , K. Ouchi, and Y. Nakamura "On the novel use of model-based decomposition in SAR polarimetry for target detection on the sea," *Remote Sensing Letters*, vol. 4, pp. 843–852, 2013.

[69] A. Das, C. P. Singh, S. Mohan, and Ajai, "Polarization signatures of land cover classes using L-band polarimetric SAR data," *Microwave Remote Sensing of the Atmosphere and Environment, Proc. of SPIE*, vol. 6410, 2006.

[70] V. Turkar, R. Deo, Y. S. Rao, S. Mohan, and A. Das, "Classification accuracy of multi-frequency and multi-polarization SAR images for various land covers," *IEEE Journal of Selected Topics in Applied Earth Observation and Remote Sensing*, vol. 5, pp. 936–941, 2012.

[71] S.-W. Chen, Y.-Z. Li, X.-S. Wang, S.-P. Xiao, and M. Sato, "Modeling and interpretation of scattering mechanisms in polarimetric synthetic aperture radar: Advances and perspectives," *IEEE Signal Processing Magazine*, vol. 31, pp. 79–89, 2014.

[72] S. V. Nghiem, S. H. Yueh, R. Kwok, and F. K. Li, "Symmetry properties in polarimetric remote sensing," *Radio Science*, vol. 27, pp. 693–711, 1992.

[73] S. H. Yueh, R. Kwok, and S. V. Nghiem, "Polarimetric scattering and emission properties of targets with reflection symmetry," *Radio Science*, vol. 29, pp. 1409–1420, 1994.

[74] Y. Yamaguchi and T. Moriyama, "Four-component scattering model for polarimetric SAR image decomposition," *IEEE Transactions on Geoscience and Remote Sensing*, vol. 43, no. 8, pp. 1699-1706, 2005.

[75] Y. Yamaguchi, Y. Yajima, and H. Yamada, "A four-component decomposition of PolSAR images based on the coherency matrix," *IEEE Transactions on Geoscience and Remote Sensing*, vol. 3, no. 3, pp. 292-296, 2006.

[76] J. J. Van Zyl, M. Arii, and Y. Kim, "Model-based decomposition of polarimetric SAR covariance matrices constrained for nonnegative eigenvalues," *IEEE Transactions on Geoscience and Remote Sensing*, vol. 49, no. 9, pp. 3452-3459, 2011.

[77] D. L. Schuler, J.-S. Lee, and T. L. Ainsworth, "Compensation of terrain azimuthal slope effects in geophysical parameter studies using polarimetric SAR data," *Remote Sensing of Environment*, vol. 69, pp. 139-155, 1999.

[78] J.-S. Lee, D. L. Schuler, and T. L. Ainsworth, "Polarimetric SAR data compensation for terrain azimuth slope variation," *IEEE Transactions on Geoscience and Remote Sensing*, vol. 38, no. 5, pp. 2153-2163, Sep. 2000.

[79] F. Xu and Y.-Q. Jin, "Deorientation theory of polarimetric scattering targets and application to terrain surface classification," *IEEE Transactions on Geoscience and Remote Sensing*, vol. 43, no. 10, pp. 2351-2364, 2005.

[80] S. R. Cloude, "Group theory and polarization algebra," *OPTIK*, vol. 75, pp. 26–36, 1986.

[81] I. Hajnsek, E. Pottier, and S. R. Cloude, "Inversion of surface parameters from polarimetric SAR," *IEEE Transactions on Geoscience and Remote Sensing* vol. 41, no. 4, pp. 727-744, 2003.

[82] J. Yin, J. Yang, Z.-S. Zhou, and J. Song, "The extended Bragg scattering model-based method for ship and oil-spill observation using compact polarimetric SAR," *IEEE Journal of Selected Topics in Applied Earth Observation and Remote Sensing*, vol. 8, no. 8, pp. 3760-3772, 2015.

[83] G. G. Ponnurangam and Y. S. Rao, "Evaluation of different orientation angle distributions within the X-Bragg scattering model for bare soil moisture estimation," *International Journal of Remote Sensing*, vol. 38, no. 15, pp. 4379–4395, 2017.

[84] E. Krogager, W. M. Borner, and S. N. Madsen, "Feature-motivated sinclair matrix (sphere/diplane/helix) decomposition and its application to target sorting for land feature classification," *Proc. SPIE*, vol. 3120, pp. 144–154, Jul. 28-29, 1997.

[85] A. Sato, Y. Yamaguchi, G. Singh, and S. E. Park, "Four-component scattering power decomposition with extended volume scattering model," *IEEE Geoscience and Remote Sensing Letters*, vol. 9, no. 2, pp. 166-170, 2012.

[86] S. H. Hong and S. Wdowinski, "Double-bounce component in cross-polarimetric SAR from a new scattering target decomposition," *IEEE Transactions on Geoscience and Remote Sensing*, vol. 53, no. 6, pp. 3039-3051, June 2014.

[87] A. Freeman, "Fitting a two-component scattering model to polarimetric SAR data from forests," *IEEE Transactions on Geoscience and Remote Sensing*, vol. 45, no. 8, pp. 2583-2592, 2007.

[88] W. An, Y. Cui, and J. Yang, "Three-component model-based decomposition for polarimetric SAR data," *IEEE Transactions on Geoscience and Remote Sensing*, vol. 48, pp. 2732–2739, 2010.

[89] O. Antropov, Y. Rauste, and T. Hame, "Volume scattering modeling in PolSAR decompositions: study of ALOS PALSAR data over boreal forest," *IEEE Transactions on Geoscience and Remote Sensing*, vol. 49, no. 10, pp. 3838–3848, Oct. 2011.

[90] B. Chen, L. Jiao, and S. Zhang, "An improved three-component model-based decomposition for polarimetric SAR Data," *International Conference on Audio, Language and Image Processing*, 2014.

[91] Z. Wang, Q. Zeng, and J. Jiao, "A new volume scattering model for three-component decomposition of polarimetric SAR data," *IGARSS*, 2018.

[92] M. Neumann, L. Ferro-Famil, and A. Reigber, "Estimation of forest structure, ground, and canopy layer characteristics from multibaseline polarimetric interferometric SAR data," *IEEE Transactions on Geoscience and Remote Sensing*, vol. 48, no. 3, pp. 1086–1104, 2010.

[93] M. Arii, J. J. van Zyl, and Y. Kim, "A general characterization for polarimetric scattering from vegetation canopies," *IEEE Transactions on Geoscience and Remote Sensing*, vol. 48, no. 9, pp. 3349–3357, 2010.

[94] M. Arii, J. J. van Zyl, and Y. Kim, "Adaptive model-based decomposition of polarimetric SAR covariance matrices," *IEEE Transactions on Geoscience and Remote Sensing*, vol. 49, no. 3, pp. 1104–1113, 2011.

[95] D. L. Schuler, J.-S. Lee, and G. D. Grandi, "Measurement of topography using polarimetric SAR images," *IEEE Transactions on Geoscience and Remote Sensing*, vol. 34, pp. 1266–1277, 1996.

[96] E. Pottier, D. L. Schuler, J. S. Lee, and T. L. Ainsworth, "Estimation of the terrain surface azimuthal/range slopes using polarimetric decomposition of POLSAR data," *IGARSS*, 1999.

[97] H. Kimura, "Radar polarization orientation shifts in built-up areas",*IEEE Geoscience and Remote Sensing Letter*, vol. 5, pp. 217–221, 2008.

[98] S.-W. Chen, M. Ohki, M. Shimada, and M. Sato, "Deorientation effect investigation for model-based decomposition over oriented built-up areas", *IEEE Geoscience and Remote Sensing Letter*, vol. 10, pp. 273–277, 2013.

[99] M. Kajimoto and J. Susaki, "Urban-area extraction from polarimetric SAR images using polarization orientation angle," *IEEE Geoscience and Remote Sensing Letter*, vol. 10, pp. 337–341, 2013.

[100] F.-Y. Zhu, Y. H. Zhang, and D. Li, "A novel deorientation method in PolSAR data processing," *Remote Sensing Letters*, vol. 7, no. 11, pp. 1083-1092, 2016.

[101] F. Xu, H. Wang, Y.-Q. Jin, X. Liu, R. Wang, and Y. Deng, "Impact of cross-polarization isolation on polarimetric target decomposition and target detection," *Radio Science*, vol. 50, pp. 327–338, 2015.

[102] J.-S. Lee and T. L. Ainsworth, "The effect of orientation angle compensation on coherency matrix and polarimetric target decompositions," *IEEE Transactions on Geoscience and Remote Sensing*, vol. 49, no. 1, pp. 53-64, Jan. 2011.

[103] S. E. Park, W. M. Moon, and E. Pottier, "Assessment of scattering mechanism of polarimetric SAR signal from mountainous forest areas," *IEEE Transactions on Geoscience and Remote Sensing*, vol. 50, pp. 4711-4719, 2012.

[104] Z. Shan, H. Zhang, C. Wang, W. An, T. Wu, and X. Chen, "Four-component model-based decomposition of polarimetric SAR data for special ground objects," *IEEE Geoscience and Remote Sensing Letters*, vol. 9, pp. 989–993, 2012.

[105] S. E. Park, "The effect of topography on target decomposition of polarimetric SAR data," *Remote Sensing*, vol. 7, pp. 4997–5011, 2015.

[106] Y. Yamaguchi, A. Sato, W. M. Boerner, R. Sato, and H. Yamada, "Four component scattering power decomposition with rotation of coherency matrix," *IEEE Transactions on Geoscience and Remote Sensing*, vol. 49, no. 6, pp. 2251-2258, 2011.

[107] W. An, C. Xie, X. Yuan, Y. Cui, and J. Yang, "Four-component decomposition of polarimetric SAR images with deorientation," vol. 8, no. 6, pp. 1090-1094, 2011.

[108] G. Singh, Y. Yamaguchi, and S.-E. Park, "General four-component scattering power decomposition with unitary transformation of coherency matrix," *IEEE Transactions on Geoscience and Remote Sensing*, vol. 51, no. 5, pp. 3014-3022, 2013.

[109] A. Bhattacharya, G. Singh, S. Manickam, and Y. Yamaguchi "An adaptive general four-component scattering power decomposition with unitary transformation of coherency matrix (AG4U)," *IEEE Geoscience and Remote Sensing Letter*, vol. 12, no. 10, pp. 2110-2114, 2015.

[110] S.-W. Chen, X.-S. Wang, S.-P. Xiao, and M. Sato, "General polarimetric model-based decomposition for coherency matrix," *IEEE Transactions on Geoscience and Remote Sensing*, vol. 52, pp. 1843-1855, 2014.

[111] Y. Yajima, Y. Yamaguchi, R. Sato, H. Yamada, and W.-M. Boerner, "POLSAR image analysis of wetlands using a modified four-component scattering power decomposition," *IEEE Transactions on Geoscience and Remote Sensing*, vol. 46, no. 6, pp. 1667-1673, 2008.

[112] G. Singh, Y. Yamaguchi, S.-E. Park, Y. Cui, and H. Kobayashi, "Hybrid Freeman eigenvalue decomposition method with extended volume scattering model," *IEEE Geoscience and Remote Sensing Letters*, vol. 10, pp. 81–85, 2013.

[113] S. Zhang, S. Wang, and B. Chen, "Modified hybrid Freeman/eigenvalue decomposition for polarimetric SAR data," *Journal of Sensors, Hindawi*, 2015.

[114] G. Liu, M. Li, Y. Wang, P. Zhang, Y. Wu, and H. Liu, "Four-component scattering power decomposition of remainder coherency matrices constrained for nonnegative eigenvalues," vol. 11, no. 2, pp. 494–498. 2014.

[115] Y. Cui, Y. Yamaguchi, J. Yang, H. Kobayashi, S.-E. Park, and G. Singh, "On Complete model-based decomposition of polarimetric SAR coherency matrix data," *IEEE Transactions on Geoscience and Remote Sensing*, vol. 52, no. 4, pp. 1991–2001, 2014.

[116] W. An, and C. Xie, "An improvement on the complete model-based decomposition of polarimetric SAR data," *IEEE Geoscience and Remote Sensing Letters*, vol. 11, pp. 1926-–1930, 2014.

[117] F. Zhu, Y. Zhang, and D. Li, "An extension of a complete model-based decomposition of polarimetric SAR data," *IEEE Geoscience and Remote Sensing Letters*, vol. 13, pp. 287–291, 2016.

[118] J. Yang, Y.-N. Peng, and S.-M. Lin," "Similarity between two scattering matrices," vol. 37, no. 3, pp. 193-194, 2001.

[119] Q. Chen, Y.-M. Jiang, L.-J. Zhao, J. Lu, and D. Hong, "A scattering similarity based classification scheme for land applications of polarimetric SAR image," *Proceedings of 2010 IEEE 17th International Conference on Image Processing*, 2010.

[120] Q. Chen, Y. M. Jiang, L. J. Zhao, and G. Y. Kuang, "Polarimetric scattering similarity between a random scatterer and a canonical scatterer," *IEEE Geoscience and Remote Sensing Letters*, vol. 7, no. 4, pp. 866–869, 2010.

[121] Q. Chen, G. Kuang, J. Li, L. Sui, and D. Li, "Unsupervised land cover/land use classification using PolSAR imagery based on scattering similarity," *IEEE Transactions on Geoscience and Remote Sensing*, vol. 51, no. 3, pp. 1817–1825, 2013.

[122] D. Li and Y. Zhang, "Random similarity between two mixed scatterers," *IEEE Geoscience and Remote Sensing Letters*, vol. 12, no. 12, pp. 2468-2472, 2015.

[123] D. Li and Y. Zhang "Random similarity-based entropy/alpha classification of PolSAR data," *IEEE Journal of Selected Topics in Applied Earth Observation and Remote Sensing*, vo. 10, no. 12, pp. 5712–5723, 2017.

[124] D. Ratha , A. Bhattacharya, and A. C. Frery, "Unsupervised classification of PolSAR data using a scattering similarity measure derived from a Geodesic distance," *IEEE Geoscience and Remote Sensing Letters*, vol. 15, pp. 151–155, 2018.

[125] D. Ratha, S. De, T. Celik, and A. Bhattacharya, "Change detection in polarimetric SAR images using a geodesic distance between scattering mechanisms," *IEEE Geoscience and Remote Sensing Letters*, vol. 14, no.7, pp. 1066–1070, 2017.

[126] H. Maurya, R. K. Panigrahi, and A. K. Mishra, "Extended four-component decomposition by using modified cross-scattering matrix," *IET Radar, Sonar and Navigation*, vol. 11, no. 8, pp. 1196–1202, 2017.

[127] ESA, PiSAR Niigata data. [Online]. https://earth.esa.int/web/polsarpro/airborne-data-sources.

[128] S.-W. Chen, X.-S. Wang, and M. Sato, "Uniform polarimetric matrix rotation theory and its applications," *IEEE Transactions on Geoscience and Remote Sensing*, vol. 52, no. 8, pp. 4756–4770, 2014.

[129] H. Maurya and R. K. Panigrahi, "PolSAR Coherency Matrix Optimization Through Selective Unitary Rotations for Model-Based Decomposition Scheme," *IEEE Geoscience and Remote Sensing Letters*, 2018. (Accepted).

[130] Dataset: UAVSAR, NASA 2012. Retrieved from ASF DAAC 07 October 2012.

[131] H. Maurya and R. K. Panigrahi, "Non-negative scattering power decomposition for PolSAR data interpretation," *IET Radar, Sonar and Navigation*, vol. 12, no. 6, pp. 593–602, 2018.

[132] Dataset: UAVSAR, NASA 2010. Retrieved from ASF DAAC 28 March 2017.

[133] H. Maurya, A. Chauhan, and R. K. Panigrahi, "A fast alternative to three- and four-component scattering models for polarimetric SAR image decomposition," *Remote Sensing Letters*, vol. 8, no. 8, 781–790, 2017.

[134] H. Maurya and R. K. Panigrahi, "Computationally fast and efficient model-based decomposition method for PolSAR data interpretation," *PIERS*, Singapore, 2017.

[135] H. Maurya and R. K. Panigrahi, "Investigation of branching conditions in model-based decomposition methods," *IEEE Geoscience and Remote Sensing Letters*, vol. 15, no. 8, pp. 1224–1228, 2018.

[136] J.-S. Lee, J.-H. Wen, T. L. Ainsworth, K.-S. Chen, and A. J. Chen, "Improved sigma filter for speckle filtering of SAR imagery," *IEEE Transactions on Geoscience and Remote Sensing*, vol. 47, no. 1, pp. 202–213, 2009.

[137] G. Singh, Y. Yamaguchi, "Model-based and six-component scattering power decomposition," *IGARSS*, 2017.

[138] G. Singh, Y. Yamaguchi, "Model-based six-component scattering matrix power decomposition," *IEEE Transactions on Geoscience and Remote Sensing*, vol. 56, no. 10, pp. 5687–5704, 2018.

[139] K. Kitayama, Y. Yamaguchi, J. Yang, and H. Yamada, "Compound scattering matrix of targets aligned in the range direction," *IEICE Transaction on Communication*, vol. E84-B, pp. 81–88, 2001.

[140] M. S. Burgin, U. K. Khankhoje, X. Duan, and M. Moghaddam, "Generalized terrain topography in radar scattering models," *IEEE Transactions on Geoscience and Remote Sensing*, vol. 54, pp. 3944–3952,2016.

[141] M. S. Burgin, X. Duan, R. Chen, U. K. Khankhoje, and M. Moghaddam, "Validation of generalized radar scattering model for sloped terrain with airborne L- and P-band data," *PIERS*, Singapore, 2017.

[142] R. Guinvarc'h and L. Thirion-Lefevre, "Cross-polarization amplitudes of obliquely orientated buildings with application to urban areas," *IEEE Geoscience and Remote Sensing Letters*, vol. 14, no. 11, pp. 1913–1917, 2017.

[143] D. K. Atwood, and L. Thirion-Lefevre, "Polarimetric phase and implications for urban classification," *IEEE Transactions on Geoscience and Remote Sensing*, vol. 56, no. 3, pp. 1278–1289, 2018.

[144] S. Quan , B. Xiong, D. Xiang, and G. Kuang, "Derivation of the orientation parameters in built-up areas: with application to model-based decomposition," *IEEE Transactions on Geoscience and Remote Sensing*, vol. 56, no. 8, pp. 4714–4730, 2018.

[145] H. Maurya and R. K. Panigrahi, "PolSAR image classification using generalized scattering models," *PIERS*, Singapore, 2017.

[146] A. Lonnqvist, Y. Rauste, M. Molinier, and T. Hame, "Polarimetric SAR data in land cover mapping in Boreal zone," *IEEE Transactions on Geoscience and Remote Sensing*, vol. 48, no. 10, pp. 3652–3662, 2010.

[147] Z. Shan, C. Wang, H. Zhang, and W. An, "Improved four-component model-based target decomposition for polarimetric SAR data," *IEEE Geoscience and Remote Sensing Letters*, vol. 9, no. 1, pp. 75–79, 2012.

[148] S. Kusano, K. Takahashi, and M. Sato, "Volume scattering power constraint based on the principal minors of the coherency matrix," *IEEE Geoscience and Remote Sensing Letters*, vol. 11, no. 1, pp. 361–365, 2014.

[149] Q. Xie, J. D. Ballester-Berman, J. M. Lopez-Sanchez, J. Zhu, and C. Wang, "On the use of generalized volume scattering models for the improvement of general polarimetric model-based decomposition," *Remote Sensing*, vol. 9, pp. 1–20, 2017.

[150] D. Duan, Y. Wang, H. Lv, H. Li., and Y. Yang "A new PolSAR decomposition algorithm to delineate urban targets," *IGARSS*, 2017.

List of Publications (Chapter-Wise)

Chapter 3

Himanshu Maurya, R. K. Panigrahi, and A. K. Mishra, "Extended Four-Component Decomposition by Using Modified Cross-Scattering Matrix," *IET Radar, Sonar & Navigation*, vol. 11, no. 8, pp. 1196-1202, 2017.

Chapter 4

Himanshu Maurya and R. K. Panigrahi, "PolSAR Coherency Matrix Optimization Through Selective Unitary Rotations for Model-Based Decomposition Scheme," *IEEE Geoscience and Remote Sensing Letters*, 2018. (Early Access)

Chapter 5

Himanshu Maurya and R. K. Panigrahi, "Non-Negative Scattering Power Decomposition for PolSAR Data Interpretation," *IET Radar, Sonar & Navigation*, vol. 12, no. 6, pp. 593-602, 2018.

Chapter 6

Himanshu Maurya, A. Chauhan, and R. K. Panigrahi, "A Fast Alternative to Three- and Four-Component Scattering Models for Polarimetric SAR Image Decomposition," *Remote Sensing Letters, Taylor and Francis*, vol. 8, no. 8, pp. 781-790, 2017.

Himanshu Maurya and R. K. Panigrahi, "Computationally Fast and Efficient Model-based Decomposition Method for PolSAR Data Interpretation," *PIERS*, 2017.

Himanshu Maurya and R. K. Panigrahi, "Investigation of Branching Conditions in Model-Based Decomposition Methods," *IEEE Geoscience and Remote Sensing Letters*, vol. 15, no. 8, pp. 1224-1228, 2018.